

EXPLORATIONS OF NANOTUBES AND NANOPORE ARRAYS AND THEIR
INTERACTIONS WITH BIOMOLECULES

BY

LAURA S. MEHRMANESH

B.A., BRYN MAWR COLLEGE, 2001

A DISSERTATION SUBMITTED IN PARTIAL FULFILLMENT OF THE
REQUIREMENTS FOR THE DEGREE OF DOCTOR OF PHILOSOPHY IN THE
DIVISION OF ENGINEERING'S ELECTRICAL SCIENCES AND COMPUTER
ENGINEERING GRADUATE PROGRAM AT BROWN UNIVERSITY

PROVIDENCE, RHODE ISLAND

MAY 2009

© Copyright 2009 by Laura S. Mehrmanesh

This dissertation by Laura S. Mehrmanesh is accepted in its present form by the Division
of Engineering as satisfying the dissertation requirement for the degree of Doctor of
Philosophy.

Date _____

Jimmy Xu, Advisor

Recommended to the Graduate Council

Date _____

Jimmy Xu, Reader

Date _____

Anubhav Tripathi, Reader

Date _____

Kenneth Miller, Reader

Approved by the Graduate Council

Date _____

Sheila Bonde, Dean of the Graduate School

Curriculum Vitae

Laura S. Mehrmanesh was born in Hartford, CT on December 20th, 1978 and grew up in Farmington, CT. She attended Farmington High School in Farmington, CT and then went on to complete her Bachelor of Arts Degree in Physics at Bryn Mawr College in Bryn Mawr, PA. She has always enjoyed interdisciplinary studies and did her undergraduate thesis in Computer Science.

Laura has taught preschool (2003) and grade school (2000-2002). She has also tutored college students (Bryn Mawr College Physics and Computer Science Department Tutor, 1998-2001).

In August of 2003, Laura joined Professor Jimmy Xu's Lab of Emerging Technologies as a Research Assistant and began her graduate program at Brown University. Her initial research included studies of handmade single-nanotube-tipped probing needles. Partway through her degree, she began focusing more on using anodized aluminum oxide (AAO) templates and template-derived structures to analyze DNA and deliver biomolecules to cells and tissues. During her Ph.D., Laura has gained experience with the SEM, confocal fluorescence microscopy, and photolithography fabrication techniques.

Preface and Acknowledgements

This thesis explores the interactions between nanotubes and nanopore arrays and their interactions with biomolecules. Interactions with individual biomolecules are explored, as are groups of biomolecules, systems of groups of biomolecules (cells), groups of cells (tissues), and groups of tissues (organ systems). The interaction explorations are grouped into three projects: interactions between nanotubes/nanopores and groups of DNA/protein molecules (the DNA and protein separation project), interactions between mounted/in-solution nanotubes and cells/tissues/organ systems (the drug delivery project) and interactions between nanotubes/nanorods and groups of cells (the Massively Multiplexed Fluorescence In Situ Hybridization, or MM-FISH, project).

The work is organized as follows: Chapter 1 gives an overview of the three projects and describes the base technology that all of the projects employ: highly ordered highly uniform anodized aluminum oxide (AAO) nanopore array templates and template-derived arrays of nanotubes and nanorods. In Chapter 2, the DNA/protein separation project is discussed, focusing first on how groups of DNA molecules interact with and are separated by arrays of nanopores and then on how groups of DNA molecules interact with and are separated by nanotubes and other nanoposts. Chapter 3 discusses the drug delivery project, investigating the ways in which nanotubes interact with each other to form a mounted nanoneedle or a well-dispersed nanotube solution, how the nanotubes interact with a biomolecule payload, and how the nanotubes can then release their biomolecule payloads in a target area (of an individual cell or tissue). In Chapter 4, the

MM-FISH project is discussed and the interactions between massively-multiplexed nanotubes/nanorods, DNA molecules and groups of cells are investigated and future work for all projects is described.

This work was supported in part by the Department of Justice (DoJ) (Grant 2004-LT-BX-K001), the Department of Defense (DoD) MURI Program and the Lifespan/Tufts/Center for AIDS Research Grant entitled “Nano-needle Array for Massively Parallel Fluorescence in Situ Hybridization.”

I want to thank my family, my colleagues and friends, my professors, my fiancé and my fiancé’s family for their support, advice, warmth, and wisdom. I want to express my tremendous gratitude to Professor Anubhav Tripathi for his collaboration, encouragement, and positivity; he has been incredibly generous with his equipment, time and counsel. I am grateful to Professor Kenneth Miller for an extraordinary learning experience in his Biology of the Eukaryotic Cell course and for his kindness, honesty, insights and feedback. I want to thank Professor Rod Beresford for his candor and guidance and Professor Peter Richardson for his ideas, counsel, and help.

I am forever indebted to my collaborators outside of Brown University: Dr. Bharat Rhamratnam and his colleagues at the Miriam Hospital in Providence, Rhode Island, Lt. Dennis Pincince at the Rhode Island State Police in the Criminal Identification Unit, Dr. Beth Zielinski-Habershaw at the University of Rhode Island, and Robin Smith, M.S. and Karen Lynch and their colleagues at the Rhode Island Health Department.

I want to express profound gratitude to my advisor and mentor, Jimmy Xu, for his unwavering kindness, expert guidance, near-infinite scientific knowledge, decades-long experience, inviting and inspiring creativity, endless patience, and relentless faith in me.

Dedication

To my fiancé, Michael Cohen.

Table of Contents

Curriculum Vitae	iv
Preface and Acknowledgements	v
Dedication	viii
Table of Contents	ix
List of Figures	xi
List of Tables	xix
Chapter 1: AAO Arrays and AAO-Grown Nanotubes and Nanorods	1
1.1 Introduction	1
1.2 AAO Arrays	3
1.2.1 Fabrication	4
1.3 AAO-Grown Nanotubes	10
1.3.1 Carbon Nanotubes	10
1.3.1.1 Fabrication	12
1.4 AAO-derived Non-carbon Nanoposts (Nanotubes, Nanopillars)	14
Chapter 2: DNA and Protein Separation	16
2.1 Prior Art and Our Two Platforms	17
2.2 Theory	23
2.2.1 DNA Separation Theory	23
2.2.2 Protein Separation Theory	29
2.3 Our DNA/Protein Separation Devices	32
2.3.1 Nanopore Array Platform	32
2.3.1.1 Fabrication	33
2.3.1.2 Experimental Procedure and Detection Method	34
2.3.1.3 Results	39
2.3.2 Nanopost Array Platform	48
2.3.2.1 Simple Chips	49
2.3.2.2 “Starting Line” Chips	51
2.3.2.3 PDMS Air Chamber Chips	53
2.3.2.4 CNTs on Si, Si nanopikes, Au-NP coated CNTs, and CNTs anchored in PDMS	58
2.3.2.5 Directly Patterned Chips	59
2.3.2.6 Complex Photolithography Chips	60
2.3.2.7 Polymeric Nanopost Chips	64
2.3.2.8 Summary of Nanopost Array Platform Prototype Progression	66
2.4 Future DNA/Protein Separation Work	69
Chapter 3: Intracellular Probing and Drug Delivery	70
3.1 Toxicity Concerns	72
3.2 Prior Art	72
3.3 Intracellular Probing and Delivery with Carbon Nanotubes	73
3.3.1 Mounted Nanoneedle Probe Delivery	73
3.3.1.1 Fabrication	74
3.3.1.2 Experimental Setup	75
3.3.1.3 Results	77

3.3.2 Free Nanotube Delivery	78
3.3.2.1 Conjugation	80
3.3.2.2 Experimental Setup	81
3.3.2.3 Results	82
3.4 Future Intracellular Work	84
Chapter 4: Massively-Multiplexed Fluorescence In Situ Hybridization (MM-FISH).....	85
4.1 Introduction	85
4.2 Relevant Carbon Nanotube Array Properties	90
4.3 Construction of MM-FISH CNT Probe Delivery System	91
4.4 MM-FISH Operation	92
4.4.1 FISH Probe Delivery	93
4.4.2 FISH Probe Spreading	97
4.4.3 Post-hybridization Solid-state “Wash”	99
4.5 Preliminary Studies: Adapted FISH Protocol	99
4.5.1 Pre-hybridization	100
4.5.2 Denaturation and Hybridization	101
4.5.3 Post-hybridization Washes and Probe Detection	101
4.6 Future MM-FISH Work	102
4.7 Conclusions	102
References	105

List of Figures

Figure 1: Thesis overview. First column: the nanostructures that we want to study. First column, top image: nanopore arrays[1]. First column, second image: nanotube (as an example of nanopost) arrays[2]. First column, third image: free nanotubes[3]. Second column: the projects through which we studied the interactions between the aforementioned nanostructures and biomolecules and groups of biomolecules. Second column, first image: courtesy of Dr. Jin Ho Kim at Brown University. Second column, third image: from [4]. Second column, fourth image: courtesy of Dr. Gary Withey. Third column: the molecules and groups of molecules that we studied: individual biomolecules[5], groups of biomolecules[5], cells (systems of biomolecules)[6], tissues (groups of cells)[7], and organ systems (groups of tissues)[8]...... 1

Figure 2: Schematic of the AAO anodization process. (a) The anodization cell (not to scale). (b) A closer look at an individual pore and ion migration during anodization. Adapted from[15]. (c) Pore formation schematic. (d) Distinguishing between the semi-spherical barrier oxide layer and the porous oxide layer. Adapted from[10]. 5

Figure 3: Schematic of the two-step anodization process. The first anodization pretreats the Al surface in a highly ordered manner. This texture is retained during the second anodization. Adapted from [10]...... 6

Figure 4: Images of AAO membranes after the second anodization. (a) Scanning electron microscope (SEM) (Hitachi S-4500) image of an AAO membrane (oblique cross-section view). The pores are 6 μm long and 32 nm in diameter. The pore density is roughly 10^{10} cm^{-2} . The anodization conditions were: 0.3 M oxalic acid solution, 15 °C, and 40 V [1]. (b) Large-area fabrication of AAO on a 4" wafer. Top image: Atomic Force Microscopy (AFM) image of the AAO surface. Bottom image: photograph of an AAO membrane (the porous alumina layer). A ruler is included in the photograph to show scale. Courtesy of Dr. Aijun Yin. (c) Some examples of the range of AAO pore diameters and periods imaged with an SEM. Image #(1)-(3): AAO anodized in 0.3M oxalic acid at 40 V and wet-etched for 0, 1, and 2 hours, respectively. Periodicity: 100 nm periods. Diameters: 40, 60 and 80 nm, respectively. Image #(4)-(5): AAO anodized in sulfuric acid at 25 and 10 V, respectively. Periodicity: 60 and 25 nm, respectively. Diameters: 30 and 12 nm, respectively. Courtesy of Dr. Aijun Yin...... 8

Figure 5: Generalized schematic illustrating the process flow for various AAO-derived arrays of nanostructures. 9

Figure 6: Template-assisted CNT array fabrication. (a) The process begins with an AAO template. (b) Electrodeposition of catalyst particles at the base of the AAO template pores. (c) Catalyst-assisted CVD growth of carbon nanotubes in AAO...... 13

Figure 7:(a) SEM image of exposed CNTs-in-AAO (the cleaved edge of a typical sample) [2]. (b) SEM image of exposed tips of CNTs-in-AAO (taken at a 30° tilt angle) [21]. (c)

SEM image of the top view of CNTs-in-AAO. The inset shows a single CNT[10]. (d) Photograph of large-area CNTs-in-AAO fabrication, courtesy of Dr. Aijun Yin. The sample is 4" in diameter. 13

Figure 8: The DNA and protein separation project focused on the interactions between nanopore and nanotube (and other nanopost) arrays (first column[1-3]) and groups of protein and DNA molecules (third column[5-8]). Second column, first image: courtesy of Dr. Jin Ho Kim at Brown University. Second column, third image: from [4]. Second column, fourth image: courtesy of Dr. Gary Withey. 16

Figure 9: Schematics of the two biomolecule separation platforms..... 22

Figure 10: Multi-gate nanopore array biomolecule sorter schematics (not to scale). (a) Sorting charged particles (intrinsically negative native-conformation proteins, SDS-treated proteins and DNA molecules). The electric field drives the negative analytes to the right. The native-conformation proteins are sorted by size (overall diameter). The linear analytes with uniform mass-to-charge ratios (SDS-treated proteins and DNA molecules) are sorted by length (discussed in Sections 2.2.1 and 2.2.2). (b) Pressure-driven multi-gate sorting of native-conformation proteins (neutral or intrinsically charged) by diameter via size-exclusion filtering. (c) Examples of native-conformation blood components being separated with pressure-driven size-exclusion filtering. 200 nm: largest AAO pore diameter to date. 10 nm: typical protein diameter. 2 nm: smallest AAO pore diameter to date. 22

Figure 11: The three mobility regimes (Ogston sieving: shown in blue; biased reptation: shown in green; the plateau regime: shown in brown) for electrophoretic separation of molecules in a collision matrix. In this case, the collision matrix is an array of nanopores. (a) Depending on the radius of gyration [47] of the DNA fragments and the diameter of the collision matrix pores, a DNA fragment can be modeled as a sphere (Ogston sieving), a chain (biased reptation) or a rod (plateau regime). (b) As each regime features a different model for the molecule, it also features a different relationship between the fragment's electrophoretic mobility and the fragment's length (usually measured in terms of base pairs, or "bp"). A difference of one base pair will result in two fragments lengths (or "bands") with different mobilities in the case of Ogston sieving; the same 1 bp difference will result in a greater difference in mobilities in the case of reptation. That 1 bp difference will not result in a difference in mobility in the plateau region (and hence not result in a separation) [45, 46]. Differences in mobility can be measured in terms of the separation distance between the bands or the difference in time that it takes the bands to get to a fixed point (like a PMT detection slit). 25

Figure 12: A diagram of a random self-avoiding walk model for polymers like DNA in the reptation mobility regime. The Kuhn length (a set of two persistence lengths) is shown [47]. 27

Figure 13: Single-gate Nanopore Array Platform separation chip. The right-hand image is a photograph of an actual chip. The left-hand inset is an SEM image of the actual

AAO collision matrix prior to its insertion into the microfluidic channel. Overall chip dimensions: 20 mm (width) x 40 mm (length) x 2 mm (depth). Courtesy of Dr. Jin Ho Kim at Brown University. 32

Figure 14: Comparison of vertical and horizontal AAO orientations (the microchannels and nanopores are exaggerated in the diagram)..... 33

Figure 15: Fabrication steps for vertically-oriented AAO Nanopore Array Platform microfluidic chips (the microchannels and nanopores are exaggerated in this diagram). (a) Create a cross-shaped SU-8 mold on a silicon wafer using standard photolithography methods. (b) Pour PDMS solution over the SU-8 mold and cure the PDMS. (c) Peel off the cured PDMS and flip it over (revealing the microchannels). (d) Close the microchannels by covering them with a pre-made PDMS coverslab. (e) Make a cut in the longest PDMS microchannel with a razor blade, insert the AAO membrane, and seal carefully with PDMS..... 34

Figure 16: A schematic of the experimental setup for the Nanopore Array Platform (the microchannels and nanopores are exaggerated in the diagram). The fluorescently labeled DNA is detected by the PMT (photomultiplier tube) as it passes a fixed point. The smaller DNA fragments move faster in the pores (have fewer collisions with the walls) and thus are detected first. Intensity vs. time electropherogram plot courtesy of Dr. Jin Ho Kim at Brown University..... 35

Figure 17: Pinched injection in a double-T microfluidic chip. (a) Cartoon of the loading phase. (b) Cartoon of the separation phase with a bright-field microscope image of an actual AAO membrane inserted into the microfluidic separation channel. (c) Fluorescent microscope images of the YOYO-1-labeled HindIII-digested lambda DNA sample during the loading phase. (d) Flow direction arrows overlaid over the image in (c). Images in (c) and (d) courtesy of Dr. Jin Ho Kim at Brown University. 38

Figure 18: Detection system. (a) Photograph of inverted microscope system, (b) Photograph of 8-channel voltage controller..... 38

Figure 19: Control experiment electropherograms of both DNA ladders taken just in front of the nanopore array membrane (where the DNA has gone through the PVP medium only). (a) Hind III-digested λ -DNA (b) 1 kbp ladder. Courtesy of Dr. Jin Ho Kim at Brown University. 40

Figure 20: Selected electropherograms from HindIII-Digested Lambda DNA experiments. The experiments are conducted with vertically-oriented AAO Nanopore Array Platform microfluidic chips (diameter of each nanopore: 20 nm, length of each nanopore: 60 μ m). Electropherogram data gathered by Dr. Jin Ho Kim at Brown University..... 46

Figure 21: Mobility data from all selected HindIII-Digested Lambda DNA runs. 46

Figure 22: Mobility data from all selected HindIII-Digested Lambda DNA runs except for Runs 45 and 194 (the runs with the fewest data points)..... 47

Figure 23: Photograph of the first Nanopost Array Platform prototype (“The Simple Chip”) for DNA separation via electrophoresis. The collision matrix is a carbon nanotube array. Buffer solution and DNA sample can be introduced via the silicone tube input port, as can the electrodes. 49

Figure 24: Photograph of the migration of fluorescently-labeled DNA (in green) within a UV-illuminated Simple Chip carbon nanotube array. A negative bias is applied to the input port and a positive bias is applied to the output port. The negatively-charged DNA fragments travel through the CNT array towards the positively charged electrode wire. The band pictured above is diffuse because of a post-electrophoresis pre-photo one-hour waiting time..... 50

Figure 25: Photograph of a platinum wire “starting line” chip. The penny is included for scale..... 51

Figure 26: Fluorescent microscope images of DNA in the “starting line” chip. Left: DNA concentrated on the positively-biased platinum wire. Right: DNA being released or “launched” when a negative potential is applied to the platinum wire. 52

Figure 27: Illustration of the gap problem (exaggerated here for discussion purposes). (a) is an ideal nanopost array chip. (b) is a common mismatch that occurs in the fabrication process..... 52

Figure 28: General fabrication procedure for PDMS air chamber chips (microfluidic channels and CNTs not to scale). In Step 1, a Si wafer substrate is coated with SU-8 photoresist. In Step 2, a photomask is placed over the SU-8 coated Si wafer. The photoresist is then exposed to UV light and the SU-8 is cured. Step 3 shows the shape of the cured SU-8 (after uncured SU-8 is removed). This cured SU-8 will serve as the master mold for poly(dimethylsiloxane) (PDMS) microchannel fabrication. In Step 4, uncured PDMS is poured over the mold and allowed to cure. The cured PDMS is then peeled off the mold and flipped over, revealing a cross-like depression (Step 5). The microchannels within this depression serve as pathways for DNA migration during electrophoresis. The carbon nanotube array collision matrix is then manually inserted (Step 5). In Step 6, the microchannels are covered with a pre-made PDMS coverslab. The PDMS coverslab has holes punched in it for input/output ports. The two PDMS layers will adhere to each other without any pretreatment (native PDMS is hydrophobic). The PDMS-PDMS seal is improved, however, by pretreating the layers with a Corona-Treater hand-held plasma generator. The oxygen plasma treatment creates Si-OH groups on the surfaces of both PDMS layers; this means that when the two layers come into contact with each other, the surface Si-OH groups react, forming covalent Si-O-Si bonds between the two layers. The oxygen plasma treatment also results in hydrophilic microchannel walls which are more compatible with aqueous DNA solutions. In Step 7, a plasma-treated pre-punched PDMS air chamber is placed atop the PDMS coverslab

and allowed to bond. In Step 8, the silicone input/output port tubes are affixed with uncured PDMS. The PDMS is then allowed to cure..... 56

Figure 29: Left: photograph of air chamber chip with a gap-closing PDMS air chamber. Right: schematic of the PDMS ceiling being pushed downward when pressure is applied via the air chamber. The bowing out of the PDMS ceiling closes the gap between the tips of the exposed CNTs and the ceiling (CNT array not to scale). 57

Figure 30: SEM image of aligned CNTs grown with PECVD. Courtesy of Chih-Hsun Hsu at Brown University..... 58

Figure 31: Diagram of direct microchannel fabrication on CNT arrays (the microchannels and CNTs are not to scale). (a) Original CNT array. (b) Tips of the nanotubes in the CNT array are exposed. (c) SU-8 is spin-coated onto the array. (d) The sample is illuminated through the cross-shaped photomask with UV light. (e) Here, the regions of SU-8 that were protected from the UV-light are outlined. (f) Unilluminated regions of SU-8 are removed. (g) Square Reactive Ion Etching (RIE) etching mask is placed atop sample. (h) The unprotected CNTs are removed with RIE etching. (i) Pre-made PDMS coverslab is placed on top of the sample to close the SU-8 microchannels. 59

Figure 32: SEM image of direct microchannel fabrication on a CNT array. Courtesy of Dr. Jin Ho Kim at Brown University. 60

Figure 33: Diagram of tunnel-type complex photolithography chip fabrication. (a) The process starts with a CNT array etched (exposed) on both sides. (b) The CNT array is pressed into SU-8-coated glass. The entire sample is then exposed to UV light and developed. (c) SU-8 photoresist is poured over the sample. (d) UV exposure and development harden the second SU-8 layer through the modified cross-shaped mask. (e) The SU-8 is developed. The illuminated regions (shown in dark green) remain and the unilluminated regions (shown in light green) are dissolved. (f) The alumina (shown in brown) is removed using an etchant (typically a mixture of phosphoric and chromic acid). (g) The microchannels are covered with a pre-made PDMS coverslab. (h) Bright-field light microscope image of an actual tunnel-type complex photolithography chip, courtesy of Dr. Jin Ho Kim at Brown University. 61

Figure 34: Diagram of upward-type complex photolithography chip fabrication. (a) The process starts with a CNT array (etched on one side only). (b) The CNT array is placed on SU-8-coated glass and hardened with UV light and photoresist developer. (c) A second SU-8 coating is added. (d) The photomask is placed atop the sample and the sample is exposed to UV light. (e) The SU-8 photoresist is developed. (f) A pre-made PDMS coverslab and air chamber are placed on top of the PDMS microchannels. (g) Bright-field light microscope image of an actual upward-type complex photolithography chip, courtesy of Dr. Jin Ho Kim at Brown University..... 61

Figure 35: Diagram of downward-type complex photolithography chip fabrication. (a) The process starts with a CNT array etched on just one side. (b) The CNT array is

pressed into SU-8-coated glass and hardened with UV exposure and developer. (c) A second SU-8 coating is added. (d) The photomask is placed on the sample and the sample is exposed to UV light. (e) The SU-8 is developed and the pre-made PDMS coverslab is placed on top of the SU-8 microchannels. (f) Bright-field light microscope image of an actual downward-type complex photolithography chip, courtesy of Dr. Jin Ho Kim at Brown University. 62

Figure 36: Bright-field microscope image of bubble generation at the edge of the CNT array in a complex photolithography DNA electrophoresis chip (the bubble generation is caused by the applied electric field). Courtesy of Dr. Jin Ho Kim at Brown University. 63

Figure 37: Top: Nanofabrication steps for making polymeric nanopost arrays. (a) Create the AAO membrane. (b) Place a sheet of polymer on top of the AAO. Apply mechanical pressure to the sample under a vacuum until the sample gets above the glass transition temperature of the polymer. (c) The AAO channels will fill with polymer. (d) Remove aluminum. (e) Remove the AAO via wet-etching. Bottom: Fabrication results from polymeric nanopost prototypes. (a) Polymeric polystyrene nanopost array. (b) A tunnel through an SU-8-supported polymeric nanopost array. (c) A higher magnification view of the SU-8-supported polymeric nanopost array. 65

Figure 38: The drug delivery project focused on the interactions between free nanotubes (first column[1-3]) and the following three targets: individual cells, tissues and organ systems (third column[5-8]). Second column, first image: courtesy of Dr. Jin Ho Kim at Brown University. Second column, third image: from [4]. Second column, fourth image: courtesy of Dr. Gary Withey. 70

Figure 39: Left: Fabrication steps for mounted nanoneedle probes. Right: SEM image of a finished mounted nanoneedle probe[85]. 74

Figure 40: Experimental setup schematic for the mounted nanoneedle payload delivery confocal microscope experiment. 76

Figure 41: Confocal microscope image of electrostatic delivery of DAPI to an individual HeLa cell using a mounted carbon nanotube nanoneedle. (a) an image of the DAPI dye. (b) an image of the plasma membrane dye. (c) Image (a) overlaid with image (b). (d) Three-dimensional scanning of the targeted cell and its neighbor. Here, you can see the cross-sections (side view) of the cells. The blue DAPI payload is clearly confined within the plasma membrane of the targeted cell and is not present in the neighboring cell. (e) A Bright-Field image of the nanoneedle penetrating the target cell [4]. 78

Figure 42: Mucosal membrane target areas for in vivo drug delivery in (a) human and (b) mouse model[8, 87]. 79

Figure 43: Conjugation scheme for our most successful “dispersed” nanotube interactions in vivo experiment. Single-walled carbon nanotubes (SWNTs) coated with a phospholipid-PEG surfactant and reacted with an amine-reactive fluorescent label. 81

Figure 44: Orally administered SWNT-PEG-AlexaFluor 594 conjugates. Tissue sections were taken from the lower bowel after a 1-day incubation period. Nuclei in blue. SWNT conjugates in red. The green arrow points to the epithelial cell layer of the mucosal membrane where we believe we are seeing nanotube uptake..... 82

Figure 45: PBS control mouse tissue section. Lower Bowel. Cell nuclei in blue. Nanotube conjugates in red. The green arrow points to the epithelial cell layer of the mucosal membrane where we believe we are seeing nanotube uptake. 83

Figure 46: Free dye (just AlexaFluor 594 dye molecules, no nanotubes) in PBS (control) mouse tissue section. Cell nuclei in blue. Free dye in red. The green arrow points to the epithelial cell layer of the mucosal membrane where we believe we are seeing nanotube uptake..... 84

Figure 47: The Massively Multiplexed Fluorescence In Situ Hybridization (MM-FISH) project focused on the interactions between nanotube arrays (first column[1-3]) and groups of cells (third column[5-8]). Second column, first image: courtesy of Dr. Jin Ho Kim at Brown University. Second column, third image: from [4]. Second column, fourth image: courtesy of Dr. Gary Withey. 85

Figure 48: (a) How conventional Fluorescence In Situ Hybridization (FISH) works[89]. (b-d) A schematic of how MM-FISH would work. (b) “Stationary” ssDNA, which are compliments to the “probe DNA” are covalently bound to the carbon nanotube tips (conjugation protocol described in detail in [90]). The hybridization reaction between the stationary ssDNA and the “probe DNA” is used to “load” the CNT array with FISH probe. (c) The loaded CNT array is then mechanically pressed into the cultured cell (or cells), piercing the cell membrane. (d) The probe DNA is then released from its stationary ssDNA anchor. Probe DNA inside the nuclear membrane is then allowed to hybridize with chromosomal DNA and sequence matches will fluoresce..... 87

Figure 49: A schematic of a small area of our CNT array system. The area depicted would represent approximately a 200 μm x 200 μm area of the array (CNTs not drawn to scale). Our subsection areas are 100 μm by 100 μm . The CNT pillars will be modified with a DNA probe, then pressed down onto a cell culture to achieve probe injection. Diagram courtesy of Dr. Gary Withey..... 92

Figure 50: MM-FISH concept. Modes of nanotube array operation during the probe delivery and hybridization procedures. (a) Probe DNA is hybridized to stationary strand DNA that is covalently linked to the CNTs. (b) The CNTs are then inserted through the cell membrane. (c) A DC-biased AC signal is then applied along with heat to melt the probe and native DNA, and drive probe DNA toward its nuclear target. (d) After probe DNA has arrived at its target, the temperature and induced CNT electromechanical vibration are reduced, and the DC bias is removed to allow the probe DNA to hybridize. Diagrams courtesy of Dr. Gary Withey. 95

Figure 51: Modes of operation of the nanotube array during the solid state washing procedure. (a) A positive DC bias and high AC amplitude and frequency draw unbound probe back to the CNTs while agitating the cellular environment to assist rapid diffusion. (b) When unbound probes have been drawn back to the array, the AC signal is turned off to allow probes to rehybridize to their complements linked to the CNTs. (c) The nanotube array is then withdrawn from the cell, removing excess probe. A positive bias is maintained to ensure that free probe will remain bound to the CNTs even in the event that they do not successfully rehybridize. Diagrams courtesy of Dr. Gary Withey. 98

Figure 52: Fluorescence microscopy image of our adapted FISH protocol results. The centromeric region of each chromosome is clearly marked with a region of increased fluorescence from the selective hybridization of the fluorescently-labeled alpha satellite DNA sequence. This experiment confirms the viability of the underlying technology of the system we seek to develop. 100

List of Tables

<i>Table 1: Recap of Nanopost Prototype Progression. Images in Rows 5-7 courtesy of Dr. Jin Ho Kim at Brown University. Image in Row 4 courtesy of Chih-Hsun Hsu at Brown University.</i>	68
<i>Table 2: Key Times in MM-FISH. Courtesy of Dr. Gary Withey.</i>	93
<i>Table 3: Modes of Operation for MM-FISH CNT Array. Courtesy of Dr. Gary Withey.</i>	96

Chapter 1: AAO Arrays and AAO-Grown Nanotubes and Nanorods

1.1 Introduction

This dissertation explores interactions between engineered nanoscale (1-999 nm) structures and biomolecules through three projects: DNA and Protein Separation, Drug Delivery, and Massively Multiplexed Fluorescence In Situ Hybridization (MM-FISH) (see Figure 1). The nanostructures focused on in this work are nanopore arrays, nanotube (and other nanopost) arrays and nanotubes dispersed in solution (“free” nanotubes). We investigate the way that our engineered nanostructures interact with biomolecule targets locally and remotely; we look at interactions with individual biomolecules, with groups of biomolecules, and with biomolecule systems (cells, tissues and organ systems).

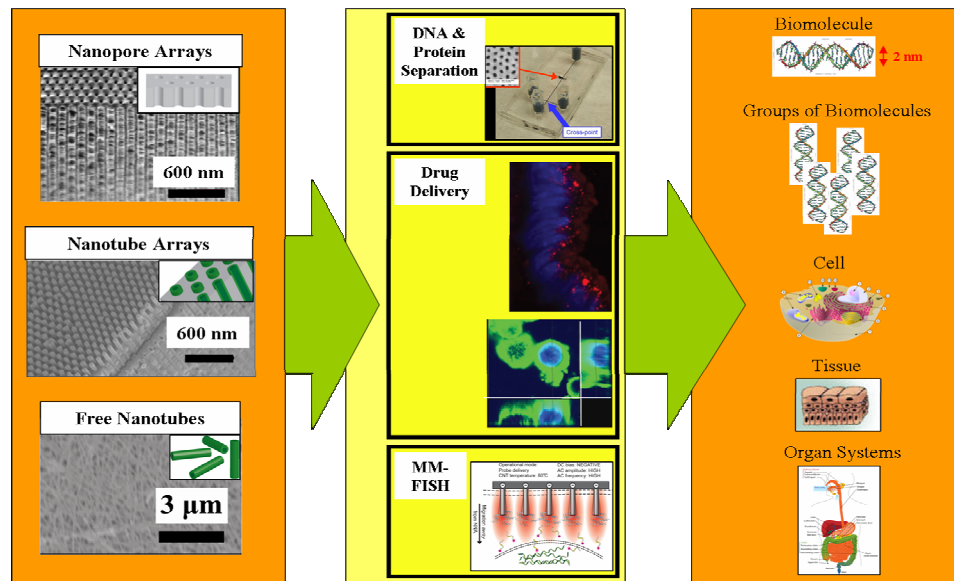


Figure 1: Thesis overview. First column: the nanostructures that we want to study. First column, top image: nanopore arrays[1]. First column, second image: nanotube (as an example of nanopost) arrays[2]. First column, third image: free nanotubes[3]. Second column: the projects through which we studied the interactions between the aforementioned nanostructures and biomolecules and groups of biomolecules. Second column, first image: courtesy of Dr. Jin

Ho Kim at Brown University. Second column, third image: from [4]. Second column, fourth image: courtesy of Dr. Gary Withey. Third column: the molecules and groups of molecules that we studied: individual biomolecules[5], groups of biomolecules[5], cells (systems of biomolecules)[6], tissues (groups of cells)[7], and organ systems (groups of tissues)[8].

The goal of the DNA project is to pioneer explorations of nanopore-DNA and nanotube-DNA interactions and create devices which exploit these interactions for the purposes of biomolecule separation and lead to powerful revolutions in DNA and protein analysis.

The aim of the drug delivery project is both to delve into the interactions between dispersed nanotubes and cells/tissues/organ systems and to use those interactions to noninvasively deliver drugs to targets which conventional methods cannot reach. The purpose of the MM-FISH project is both to explore interactions between nanotube arrays and groups of cells and to utilize those interactions to massively multiplex a genetic analysis technique called Fluorescence In Situ Hybridization (FISH), resulting in fast clinical screening of genetic mutations in the chromosomes of individuals.

The scale of the engineered nanostructures we are studying, the nanoscale (1-999 nm), is one of the most exciting scales in modern science and key for accessing local interactions with biomolecules. This scale is where all major traditional scientific disciplines meet[9]. It is the scale of objects as fundamental as molecules, electron wavelengths [10, 11], and photons. It is the scale at which fundamental biological processes, such as gene regulation, cell communication, information storage, transcription and mitosis, take place[12]. It is the scale of chemical reactions, evanescent waves, quantum mechanical effects such as tunneling and electron wave interference and the limit of conventional semiconductor fabrication technology[13]. Biologists are experts at understanding the function of molecules in the context of complex spatial and temporal systems. Chemists

specialize in the way molecules form and come apart. Physicists study electrons, photons, atoms, and the behavior of ensembles of molecules. The nanoscale is where approaches and knowledge from physics, chemistry, and biology can all be applied [9] and new solutions can be found via interdisciplinary combinations of theory, technique, and experience. Investigation devices with features on the nanoscale have already begun to give us exciting new information about fundamental processes important to all fields and will likely continue to uncover currently inaccessible phenomena[9, 10].

1.2 AAO Arrays

Central to all of the engineered nanostructures discussed in this dissertation is the anodized aluminum oxide (AAO) nanopore array template. Modified AAO templates (through-pore membranes, Figure 5e) can serve as nanopore arrays for biomolecule separation. Modified and unmodified AAO templates can serve as masks for template-assisted fabrication of nanotube and nanopillar arrays (Figure 5 d,h) for biomolecule separation, drug delivery, and MM-FISH.

AAO has many properties that make it the ideal biomolecule interaction investigation device element, including:

- a high aspect ratio[14, 15] for
 - a high number of DNA-matrix collisions during electrophoretic DNA separation in nanopores.
- transparency [16] for
 - real-time imaging of DNA separation in nanopores.

- a high degree of tunability and uniformity in pore dimensions[10, 16] and periodicity[14] ((25 to 400 nm[10]) for
 - precise size-exclusion capabilities for native-state protein separation.
 - a wide range of pore diameters (2 to 200 nm, uniform diameters for 20-200 nm[10]) for multi-stage DNA and protein separation devices.
- a thermal robustness[14, 16] for
 - tolerance of high temperatures during high-voltage (for high-speed separation) electrophoresis.
- low manufacturing cost[10, 14, 15, 17] and semiconductor-compatible[10] for
 - mass-produced disposable DNA separation chips for contamination-free results.

1.2.1 Fabrication

AAO nanopore array templates are formed by anodizing high-purity aluminum under certain conditions. If the conditions are right, nanopores will form and self-organize into a highly ordered hexagonal array of straight parallel uniform pores with pore diameters, periods, array sizes that vary over ranges beyond the reach of any lithography methods[10]. The physical mechanisms underlying the impressive uniformity and aspect ratio are not yet completely understood, but some hypotheses have been offered and can be further studied in [10, 15].

The anodization process can be summarized as follows. The process begins with electropolishing a strip or disc of high-purity aluminum film (99.999%) for 3 minutes in a

solution of HClO_4 and $\text{C}_2\text{H}_5\text{OH}$. Next, the electropolished aluminum is placed in an electrolyte bath (i.e. oxalic acid) and an electrical circuit is established between the cathode plate electrode and the anode (the aluminum film) (see Figure 2a). Initially, a barrier oxide layer forms; this barrier layer is maintained during the development of the porous oxide layer. The porous alumina layer thickens over time while the barrier layer remains as a semi-spherical oxide layer at the base of each pore (see Figures 2c & 2d)[10].

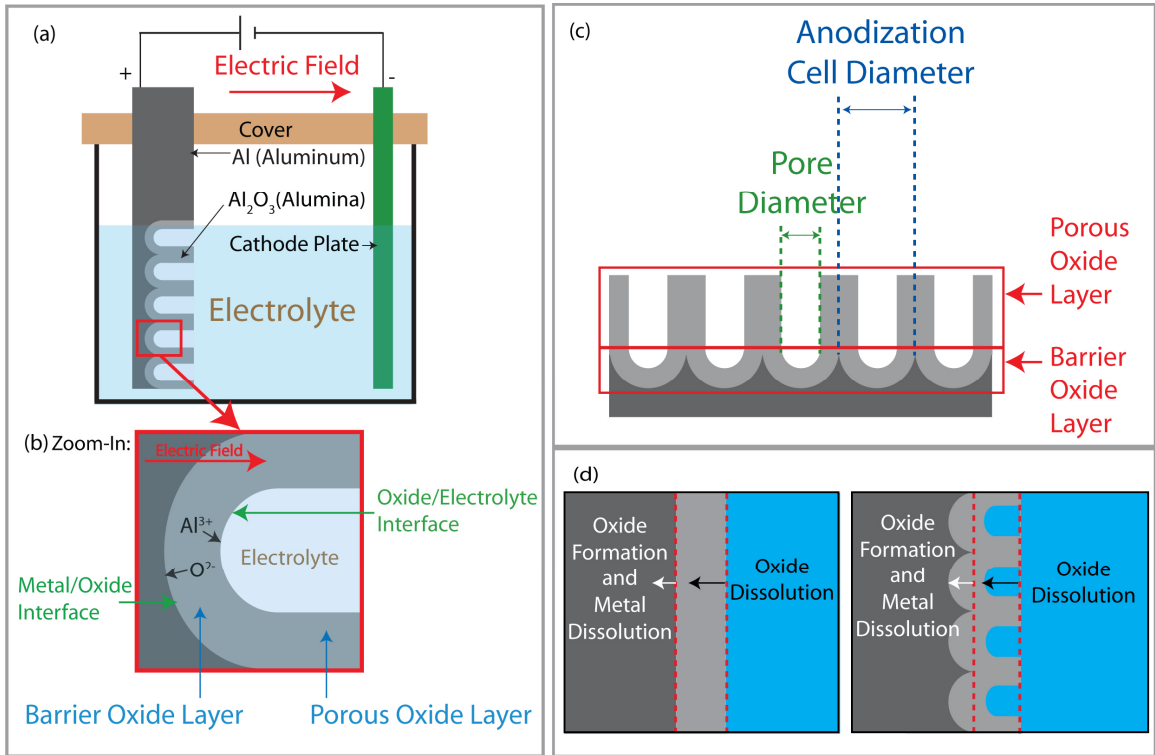


Figure 2: Schematic of the AAO anodization process. (a) The anodization cell (not to scale). (b) A closer look at an individual pore and ion migration during anodization. Adapted from[15]. (c) Pore formation schematic. (d) Distinguishing between the semi-spherical barrier oxide layer and the porous oxide layer. Adapted from[10].

The anodization process is governed by the following three reactions[15, 16]:



In the anodization cell, the base metal is dissolved according to Equation 1.3. Initially, the Al^{3+} ions contribute to oxide formation only (Equation 1.2 in reverse). When the Al^{3+} ions drift through the oxide and are released into the electrolyte (Equation 1.3), pore growth begins. Steady-state pore growth occurs when the oxide formation at the metal/oxide interface (Equation 1.1) is in equilibrium with the field-enhanced oxide dissolution at the oxide/electrolyte interface (Equation 1.2). The oxide dissolution preferentially occurs at the pore bottoms because the electric field is highest there.

The anodization cell diameter (which determines the periodicity), initial pore diameter and the barrier film thickness are directly proportional to the anodization voltage. Long anodization times rearrange the anodization cells, reducing the number of defects and improving the overall uniformity of the AAO[10].

An even more effective way of improving the pore ordering is performing a two-step anodization (see Figure 3). After the first anodization, the porous AAO layer is removed with a 6% phosphoric acid/1.8% chromic oxide (wt%) solution at 60°C and the pre-patterned remaining material is re-anodized[10].

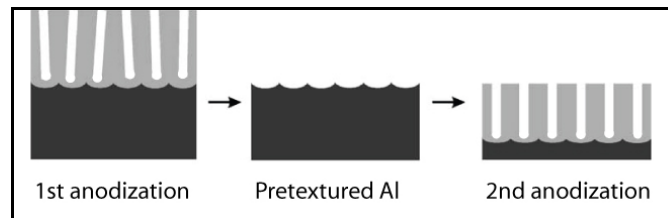
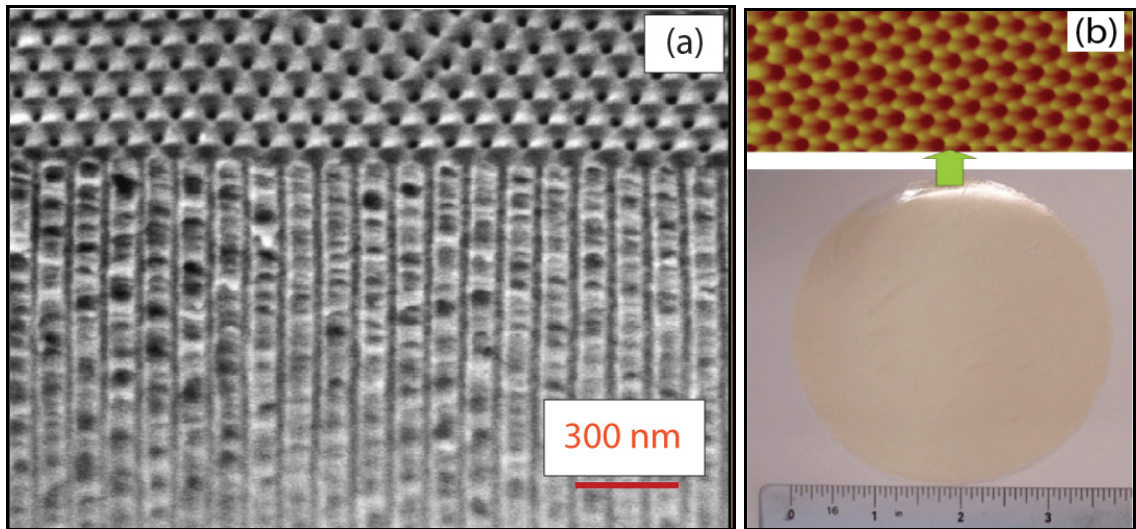


Figure 3: Schematic of the two-step anodization process. The first anodization pretextures the Al surface in a highly ordered manner. This texture is retained during the second anodization. Adapted from [10].

The two-step anodization is performed in one of the following acids: oxalic acid, sulfuric acid, or phosphoric acid. The anodization time in the re-anodization step determines the thickness of the porous AAO layer (or, equivalently, the length or depth of the pores). The pores can then be widened by wet-etching in phosphoric acid, allowing the pore diameter to be tuned independently of the pore periodicity and length [1, 10].

Figure 4c shows the wide range of pore diameters and spacings that can be achieved by varying the anodization conditions and wet-etch times[10]. Generally speaking, a 1 V anodization voltage is associated with a pore diameter growth of approximately 1.2 nm[16].



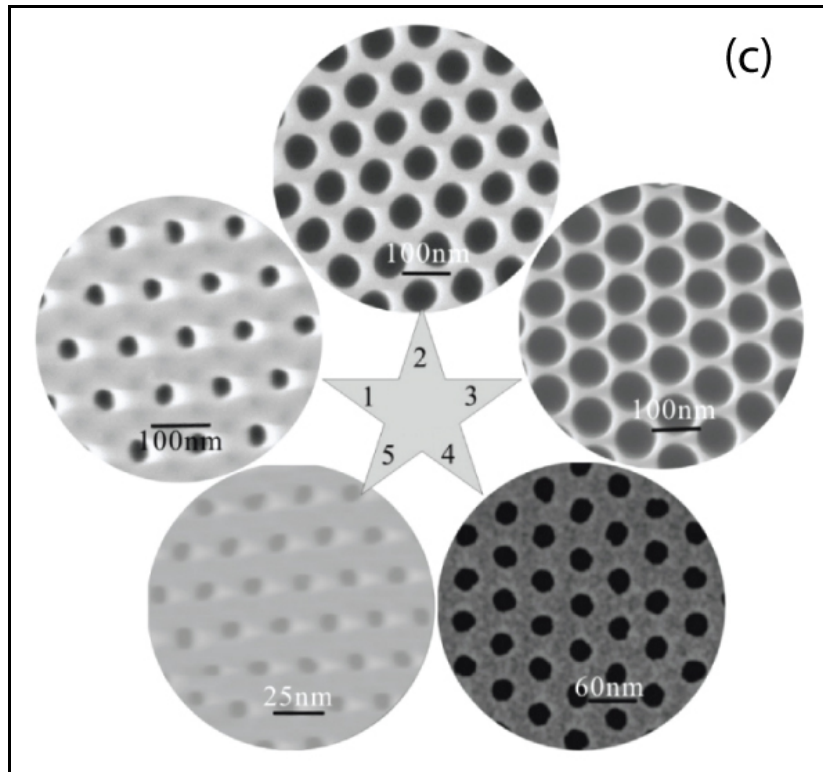


Figure 4: Images of AAO membranes after the second anodization. (a) Scanning electron microscope (SEM) (Hitachi S-4500) image of an AAO membrane (oblique cross-section view). The pores are 6 μm long and 32 nm in diameter. The pore density is roughly 10^{10} cm^{-2} . The anodization conditions were: 0.3 M oxalic acid solution, 15 $^{\circ}\text{C}$, and 40 V [1]. (b) Large-area fabrication of AAO on a 4" wafer. Top image: Atomic Force Microscopy (AFM) image of the AAO surface. Bottom image: photograph of an AAO membrane (the porous alumina layer). A ruler is included in the photograph to show scale. Courtesy of Dr. Aijun Yin. (c) Some examples of the range of AAO pore diameters and periods imaged with an SEM. Image #(1)-(3): AAO anodized in 0.3M oxalic acid at 40 V and wet-etched for 0, 1, and 2 hours, respectively. Periodicity: 100 nm periods. Diameters: 40, 60 and 80 nm, respectively. Image #(4)-(5): AAO anodized in sulfuric acid at 25 and 10 V, respectively. Periodicity: 60 and 25 nm, respectively. Diameters: 30 and 12 nm, respectively. Courtesy of Dr. Aijun Yin.

Following the second anodization, the barrier-layer-containing nanoporous alumina layer can be liberated from the aluminum base with a 6% phosphoric acid/1.8% chromic oxide (wt%) solution. The freed alumina template (Figure 5a) features open pores on the top face and closed pores on the bottom face (where the oxide barrier layer persists). To obtain a through-pore membrane (a membrane with pores that are open on both faces), the freed alumina template can be wet-etched with 0.1 M phosphoric acid solution or plasma-etched with a mixture of CF_4 and O_2 gas. The resulting through-pore AAO

membrane (Figure 5e) can then be used as a stencil or mask for producing a wide variety of highly ordered nanostructures (Figure 5 f-i)[10]. The nanostructures that this dissertation focuses on are through-pore nanopore array membranes (Figure 5e), “exposed” nanotube and nanopillar arrays (Figure 5d,h) and nanotubes that are liberated from the AAO template (or grown with other methods) (Figure 5c).

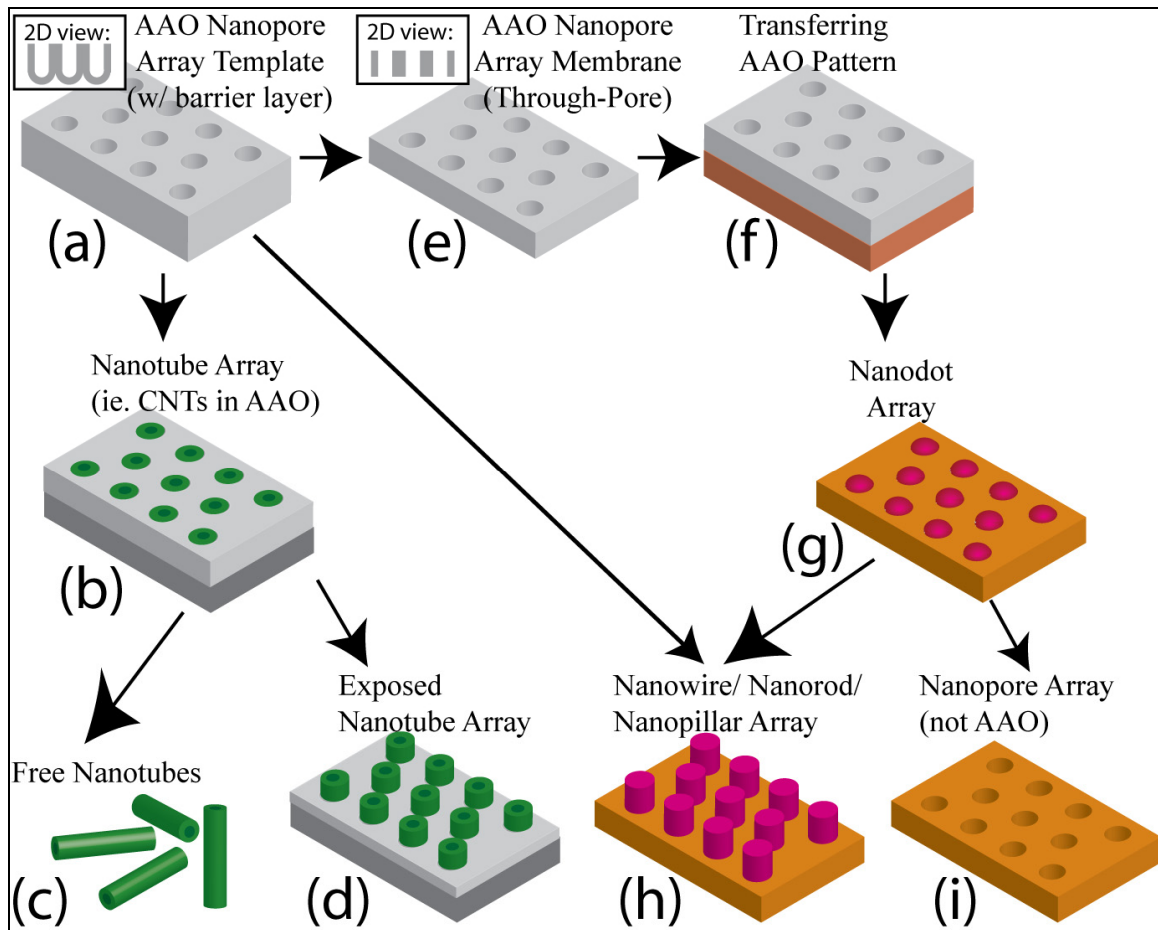


Figure 5: Generalized schematic illustrating the process flow for various AAO-derived arrays of nanostructures.

1.3 AAO-Grown Nanotubes

1.3.1 Carbon Nanotubes

Carbon nanotubes and carbon nanotube arrays, key players in the nanotube-biomolecule interactions explored in the all three projects, have extraordinary properties. Template-grown carbon nanotube arrays inherit many of the impressive uniformity and tunability aspects of the AAO template and bring some new properties to the picture. Some of the properties of carbon nanotube arrays most relevant to the nanotube-biomolecule interactions studied here include:

- a high aspect ratio [14, 15] for
 - a small diameter for noninvasive cell membrane penetration coupled with a long length for high payload capacity in the context of free nanotube drug delivery and MM-FISH.
 - a high degree of hydrophobic-hydrophobic interactions in mounted drug delivery nanoneedles which provides additional strength for the nanoneedles.
- a high degree of tunability and uniformity in pore dimensions[10, 16] and periodicity [14] for
 - optimization of inter-post gap (acts like a “pore”) in electrophoretic DNA separation with nanoposts.
 - precise size-exclusion capabilities for native-state protein separation.
 - optimization of drug-delivering nanotube dimensions for maximum cellular uptake and minimum toxicity.

- optimization of nanotube array periodicity and dimensions for cell membrane piercing and FISH probe delivery in the context of MM-FISH.
- a thermal robustness [14, 16] for
 - tolerance of high temperatures during high-voltage (for high-speed separation) electrophoresis.
- large-area fabrication [10, 17] (see Figure 7d), low manufacturing cost [10, 14, 15, 17] and semiconductor-compatible [10] for
 - disposable forensic DNA separation chips for contamination-free results.
 - disposable clinical MM-FISH chips for contamination-free results.
- high pore density [14] [10, 14, 15, 17] (approximately 10^9 - 10^{11} cm⁻²) due to the hexagonal symmetry of the AAO template [10] for
 - a high number of collisions during electrophoretic DNA separation via nanoposts.
 - high FISH probe nanotube loading for high-throughput MM-FISH.
- high strength [18] (MWNT tensile strength \sim 63 GPa [19], \sim 50X that of carbon steel) for
 - repeated injections in the context of mounted nanoneedle drug delivery and MM-FISH.
- high thermal conductivity (\sim 6000 W/M/K), high current density (10^9 A/cm², roughly 1000 times greater than that of copper), and low resistivity (\sim 10⁻⁴ ohm-cm for SWNTs at 300K [19]) for
 - DC and AC field assistance during FISH probe loading and releasing.
- biocompatibility (CNTs are chemically inert when capped) for

- low toxicity in the context of drug delivery and MM-FISH.

1.3.1.1 Fabrication

Since the discovery (or rediscovery) of carbon nanotubes in 1991[2], these tiny tubes have received a tremendous amount of attention from the scientific community as they have the potential to greatly impact future technology[10]. The widespread interest in these structures has given rise to a variety of fabrication methods[19]. The most popular fabrication methods are arc discharge, laser ablation, and chemical vapor deposition (CVD)[19]. In order to produce CNT arrays with all of the benefits of our template as well as all of the properties of carbon nanotubes, we grow our CNTs in our AAO templates and employ the CVD method.

Our fabrication procedure begins with the barrier-layer-containing AAO template (Figure 6a). The first step is to electrochemically deposit catalyst particles (typically iron, cobalt or nickel) at the base of the template pores (Figure 6b). The carbon nanotube array is then grown (Figure 6c) in two steps. The first step is the reduction of the catalyst; this step involves heating the sample at 600°C in a tube furnace for four to five hours while flowing CO gas (at 100 cm³ min⁻¹). Following that, the CO gas is replaced with a mixture of 10% acetylene in nitrogen (at the same flow rate). Conventional protocols maintain acetylene flow for two hours at 650°C[10]. Other recipes call for methane gas and higher temperatures[20].

At this point, the top surface of the sample is often ion-milled to remove any residual amorphous carbon. The nanotubes can then be exposed (see Figure 7a,b & Figure 5d) by wet-etching the sample in phosphoric acid (this removes the topmost alumina)[1, 10]. The nanotube length is determined by the thickness of the AAO membrane (Figure 6c).

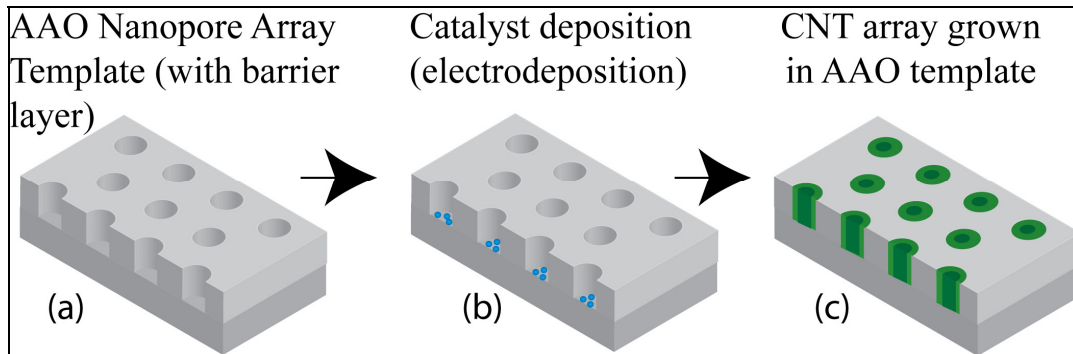


Figure 6: Template-assisted CNT array fabrication. (a) The process begins with an AAO template. (b) Electrodeposition of catalyst particles at the base of the AAO template pores. (c) Catalyst-assisted CVD growth of carbon nanotubes in AAO.

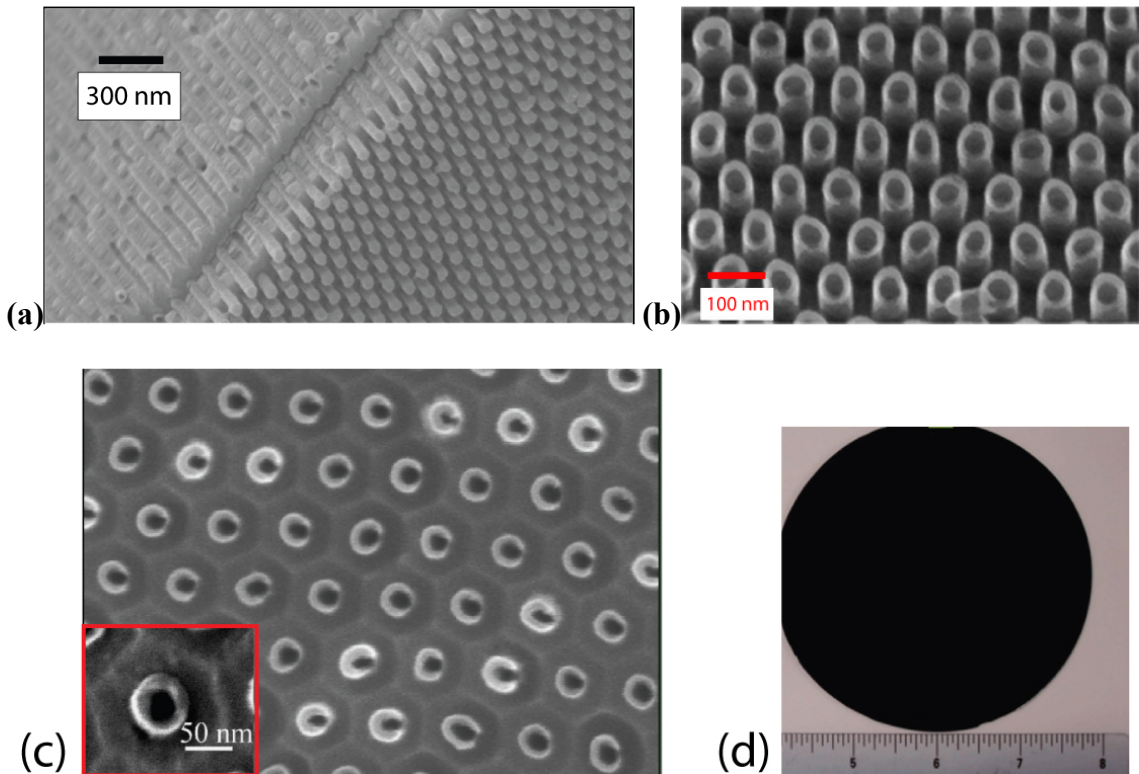


Figure 7:(a) SEM image of exposed CNTs-in-AAO (the cleaved edge of a typical sample) [2]. (b) SEM image of exposed tips of CNTs-in-AAO (taken at a 30° tilt angle) [21]. (c) SEM image

of the top view of CNTs-in-AAO. The inset shows a single CNT[10]. (d) Photograph of large-area CNTs-in-AAO fabrication, courtesy of Dr. Aijun Yin. The sample is 4" in diameter.

1.4 AAO-derived Non-carbon Nanoposts (Nanotubes, Nanopillars)

The AAO template can also be used to generate non-carbon nanotubes (See Figure 5b,d), nanodots (Figure 5g) and nanorods/wires/pillars (Figure 5h). In principle, almost any solid material can be created within the AAO membrane provided a suitable chemical pathway can be established. There are essentially five representative strategies for template synthesis of nanostructures: electrochemical deposition, electroless deposition, chemical polymerization, sol-gel deposition and chemical CVD[9].

Electrochemical deposition involves coating one side of the template with a metal film (or leaving the base aluminum layer attached to the porous alumina membrane) which will serve as a cathode (positive electrode) and attract negative metal ions during the electroplating process. The pore is filled from the bottom up; the height of the resultant nanostructure can therefore be set by the deposition time and rate[9].

“Electroless” (or “chemical”) deposition uses a chemical reagent to deposit a material from the surrounding phase onto the template surface. This process, unlike electrochemical deposition, does not require an electrochemically conductive base layer. Electroless deposition begins depositing material at the pore walls. This means that a hollow tubule can be fabricated with short deposition times and solid rods can be produced with long deposition times[9].

Chemical polymerization is a process by which conductive polymers are formed in the template by polymerizing the appropriate monomer. This can be accomplished with a simple immersion in a solution containing the monomer and polymerization agent. Here, the polymer nucleates primarily on the pore walls (similar to electroless deposition) and can produce hollow tubules or solid rods depending on the deposition time[9]

Sol-gel deposition usually requires first preparing a solution of a precursor molecule. A suspension of colloid particles (the sol) is obtained and a gel of aggregated sol particles is thermally treated. This generates nanostructures within the template pores and can yield both tubules and fibrils[9].

Chemical vapor deposition, or CVD, was discussed in Section 1.3.1.1 in the context of growing carbon nanotubes. This method can also be used to grow non-carbon nanotubes. CVD entails the solidification of gas phase reactants (for example, ethylene and pyrene) on the template surface. The reactants are decomposed resulting in the deposition of their components on the template surface. The thickness of the resultant nanostructures depends on the total reaction time and pressure[9].

Chapter 2: DNA and Protein Separation

In this chapter, the interactions between AAO nanopore arrays and AAO-derived nanotube (and other nanopost) arrays are explored and exploited for the purposes of DNA and protein separation (see Figure 8). As discussed in Sections 1.2 and 1.3.1, the properties of these arrays lead us to believe that their interactions with DNA and protein can lead to fast, sensitive, portable, contamination-free and low-cost biomolecule separation of a wide range of biomolecules and powerful revolutions in DNA and protein analysis.

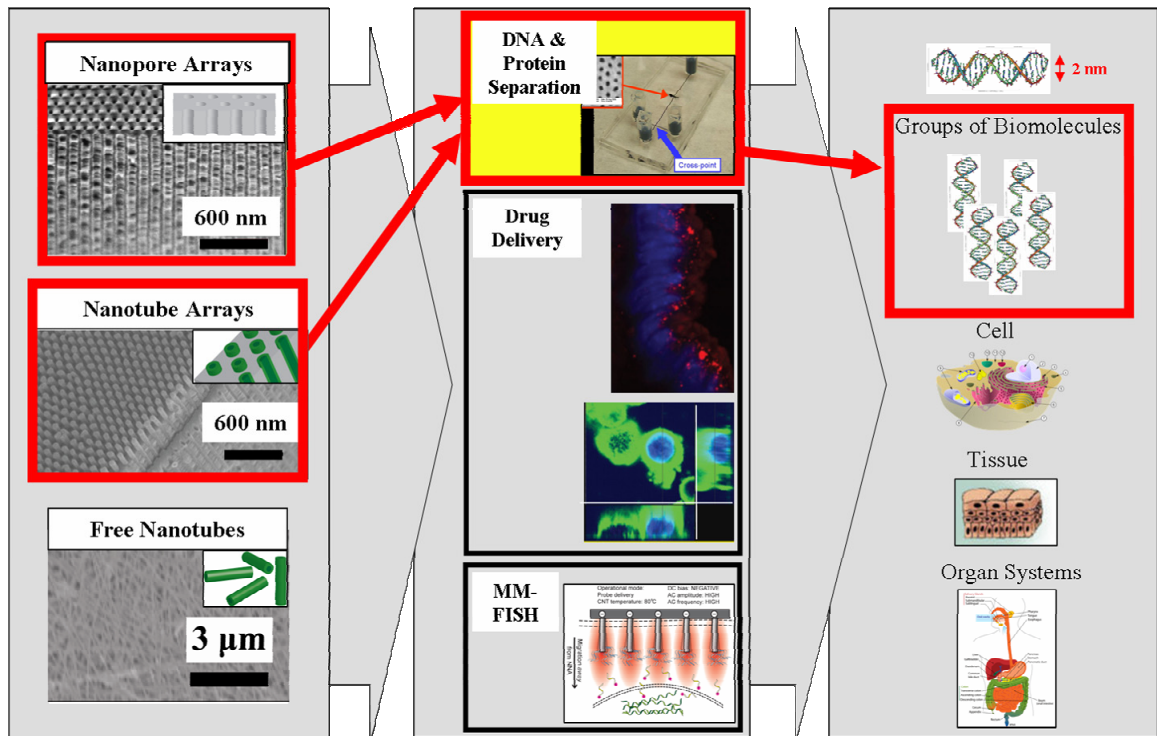


Figure 8: The DNA and protein separation project focused on the interactions between nanopore and nanotube (and other nanopost) arrays (first column[1-3]) and groups of protein and DNA molecules (third column[5-8]). Second column, first image: courtesy of Dr. Jin Ho

Kim at Brown University. Second column, third image: from [4]. Second column, fourth image: courtesy of Dr. Gary Withey.

The separation of DNA is a key component in genomic analysis in general and has applications in DNA sequencing, forensics[22], disease diagnosis and treatments, cancer research, environmental pathogen monitoring[23], and evolution and speciation studies[24].

The sorting of proteins is key in the hunt for better biomarkers. An ideal biomarker is one that would be detectable in a noninvasively collected sample; accordingly, much of the emphasis in proteomics has been on the analysis of biofluids like blood serum and plasma, urine, cerebrospinal fluid, and lymphatic fluid[25]. Our circulatory system is composed of the heart, blood, and over 100,000 km of veins, arteries, and capillaries. Generally speaking, no cell in the human body is outside the diffusion distance of the circulatory system. No other biofluid has an intimacy with a body like blood has and thus it is not surprising that blood holds a richness of information concerning the overall pathophysiology of the patient[25]. Given the incredible complexity of blood proteomes and the dynamic range of protein abundance, new high-precision multi-stage devices are needed for discovering new biomarkers and detecting established biomarkers[26].

2.1 Prior Art and Our Two Platforms

While many groups have made impressive biomolecule separation devices[27-32], we are the first group to take advantage of AAO's properties and orient our nanopore membrane vertically, allowing for compact multi-gate sorting in one separation channel.

State-of-the-art commercial ultrafiltration and dialysis membranes have elaborate convoluted pore structures (much like sponges) and are ~ 1,000 times thicker than the molecules they are designed to separate, leading to poor size cutoff properties, filtrate loss within the membranes, and low transport rates. While the pore diameter can be tuned by the processing method and starting material, other geometric aspects, such as porosity, thickness and pore diameter distribution, are strikingly insensitive to such parameters. Simple short cylindrical pores, on the other hand, can be expected to filter molecules faster and with less analyte loss[33].

Much progress is being made in alternate micro- and nano- pore separation devices. Researchers at the University of Florida have developed an anionic surfactant biasing method of making functionalizable Au nanotube membranes with diameters less than 1 nm[34]. Yamaguchi et al. have fabricated a hybrid silica-surfactant/alumina membrane with 3.4 nm diameter channels using surfactant templating [35]. Striemer and his team at the University of Rochester have used rapid thermal annealing to nucleate nanocrystals in amorphous silicon and form voids which span the membrane. These voids are then used to etch 5-25 nm pores. Striemer and his colleagues can separate the blood proteins BSA (diameter = 6.8 nm) and IgG (diameter = 14 nm) with a 15 nm thick nc-Si membrane in approximately three minutes[27]. Frank Martin's team has used top-down microfabrication methods to create silicon-based nanochannels as small as 7 nm[36]. Bob Austin's group has made single nanofluidic channels 11 to 50 nm wide and 1.5 cm long using a combination of crystallographic anisotropic etching, conformal coating, edge patterning and imprinting[37]. Juan Santiago et al. have used conventional

photolithography and dry chemical etching to fabricate devices with single silica separation channels as small as 40 nm in width for bodipy and fluorescein separation[28]. They have also used conventional photolithography dry chemical etching to fabricate channels 40-1,560 nm deep and separated 10-100 bp dsDNA in 120 seconds[29].

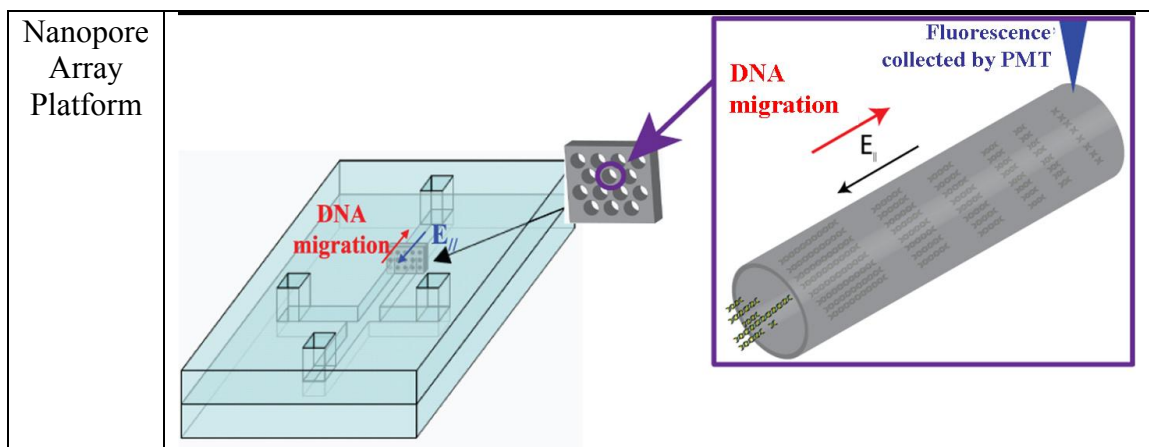
Progress is also being made in micro- and nano-post filtration devices. Young-Soo Seo et al. can construct arrays of silicon nanodots which are 11 to 13 nm in height and 250-300 nm center-to-center using sputtering, self-assembling diblock copolymers, a Langmuir-Blodgett trough, and ion milling[38]. The Austin group has separated DNA with an array of silicon posts which are 2 μm in diameter, 2 μm apart, and 2 μm tall using conventional photolithography[30]. Austin has also separated whole blood components using two types of Bosch-etched continuous flow deterministic arrays. One type, a fractionating device (or FD), separates white blood cells and red blood cells from whole blood. The critical diameter of each FD section varies from 3-9 μm at 0.5 μm intervals. The other type, a plasma separation device (or PD), consists of three separate regions, each with a different gap (20, 9, and 5 μm)[31]. Richard Mathies' group has manufactured "tapered turn" capillaries approximately 65 μm in diameter using conventional photolithography[32]. Other nanofabrication methods include: interference lithography, X-ray lithography, sacrificial electrical-spinning fibers, shadow evaporation, and scanning probe techniques[17, 37].

The next generation of biomolecule separation devices needs to be able to separate a wide range of analyte molecules and still be compact. DNA samples (forensic crime scene

samples in particular) often contain a wide range of DNA fragment lengths, not to mention a variety of other biomolecules. Complex biofluids like blood contain a wide range of analyte sizes (a few hundred pm to $\sim 10 \mu\text{m}$ [39, 40]) and abundances (10 to 12 orders of magnitude in plasma[26]). Analyzing these enormous ranges is quite difficult, even with current state-of-the-art devices. While photolithography, X-ray lithography and reactive ion etching (dry chemical etching) are well-suited to large area 2D patterning and facile integration with silicon technology, they are fundamentally limited by the feature sizes of the masks, the exposure wavelengths (in the case of X-ray lithography and photolithography) and the photoresist material[17]. Electrospun fibers might not suffer from edge roughness, but it is difficult to position the fibers precisely[37]. All nanostructure-writing (nanolithography) tools based on a fixed writing beam and a moving stage (electron beam, ion beam) have difficulty maintaining sub-20 nm writing over centimeter distances. The noise in these writing tools gives rise to line-edge-roughness (LER) which has an average size of 5-50 nm and will clog the channel before the average channel width is reduced to 20 nm or less[37]. Electron-beam lithography is additionally limited by long exposure times[17]. Scanning probe (AFM and SPM) and e-beam lithography suffer from high capital equipment costs[17]. Interference lithography can produce thin continuous channels over centimeters in length, but suffers from LER and typically makes dense, multiple channels rather than a single channel [37]. Streimer's crystallization void technique, while impressive in terms of producing small pore sizes and thin membranes, produces a relatively broad pore size distribution[27, 33]. Self-assembly (non-lithographic) processes rely upon the properties

of the starting material and formation conditions but have no inherent feature or domain size limitations and do not require expensive equipment[10].

We have developed two new biomolecule separation platforms based on the self-assembled (and therefore limit-free) AAO template: a Multi-gate Nanopore Array Platform and a Nanopost Array Platform (see Figure 9). Our most successful platform, the Multi-gate Nanopore Array Platform, takes advantage of the cylindrical pore geometry, uniform pore diameters, high porosity, and theoretically unlimited analyte size range[10] of AAO. Central to this approach is a sequential gating system that employs a series of AAO membranes, each having a different pore size (2-200 nm) (see Figure 10). This compact multi-diameter array set would be able to separate complex biofluids into their fundamental components (blood cells and platelets, blood plasma proteins, DNA molecules, hormones, dissolved nutrients like sugars and fatty acids, waste, and mineral ions[39]) in a single run, saving time, money, sample, and workspace.



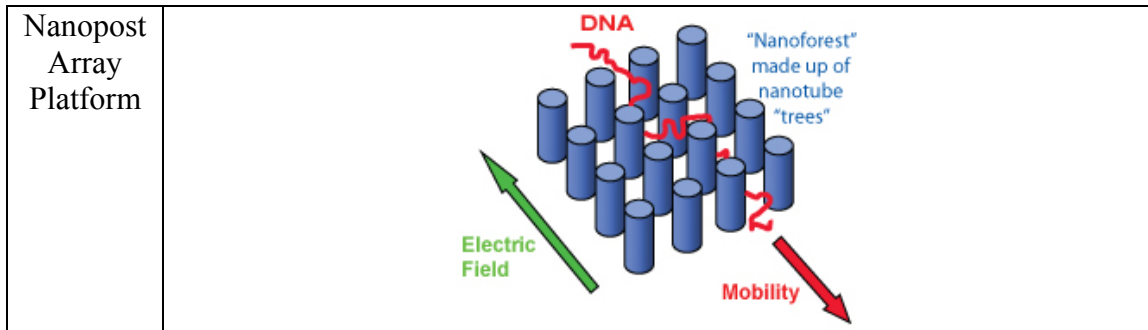


Figure 9: Schematics of the two biomolecule separation platforms.

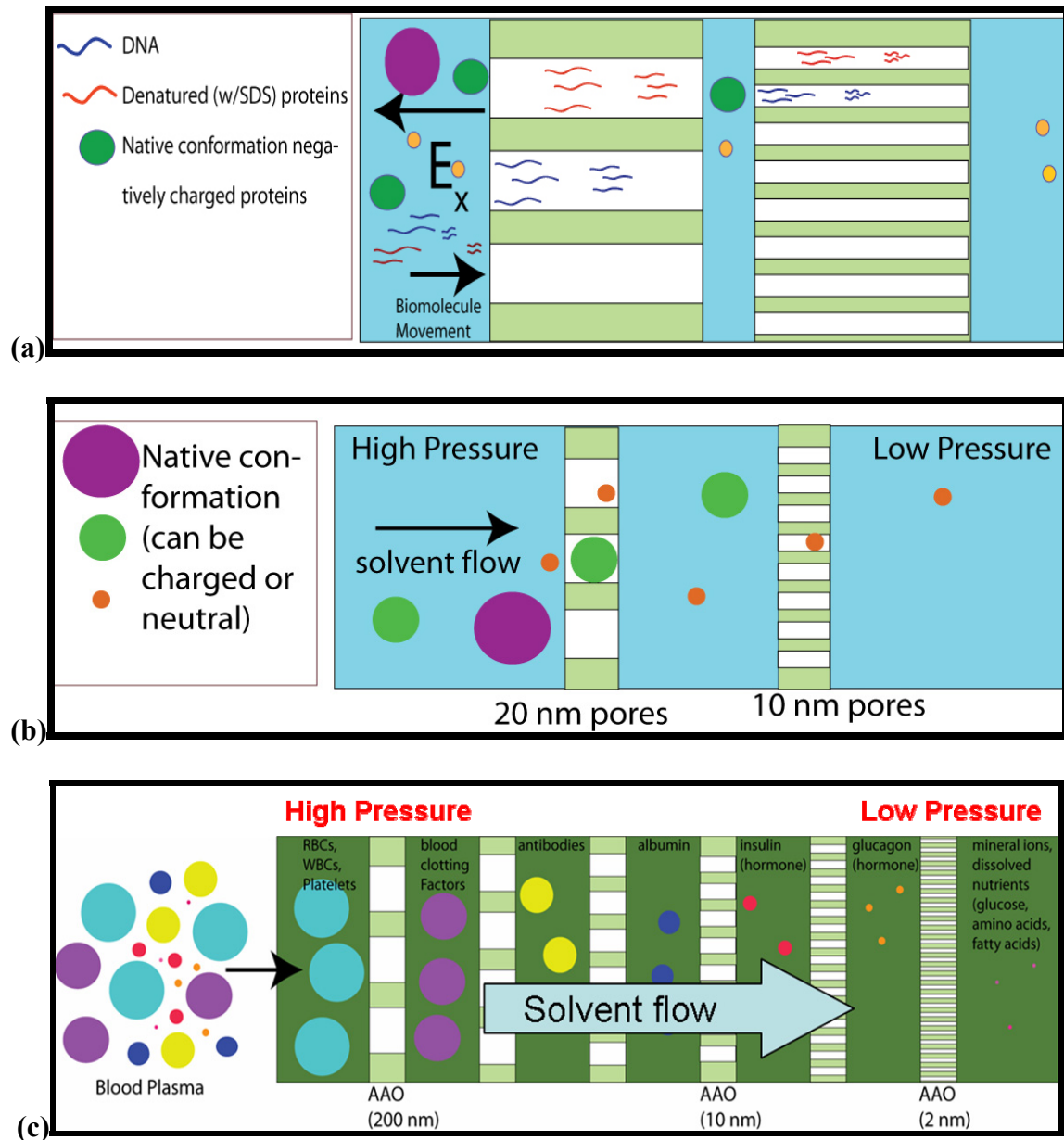


Figure 10: Multi-gate nanopore array biomolecule sorter schematics (not to scale). (a) Sorting charged particles (intrinsically negative native-conformation proteins, SDS-treated proteins and

DNA molecules). The electric field drives the negative analytes to the right. The native-conformation proteins are sorted by size (overall diameter). The linear analytes with uniform mass-to-charge ratios (SDS-treated proteins and DNA molecules) are sorted by length (discussed in Sections 2.2.1 and 2.2.2). (b) Pressure-driven multi-gate sorting of native-conformation proteins (neutral or intrinsically charged) by diameter via size-exclusion filtering. (c) Examples of native-conformation blood components being separated with pressure-driven size-exclusion filtering. 200 nm: largest AAO pore diameter to date. 10 nm: typical protein diameter. 2 nm: smallest AAO pore diameter to date.

2.2 Theory

2.2.1 DNA Separation Theory

In order to understand the interactions between DNA molecules and our engineered nanostructures and explore the ways in which those interactions can lead to the separation of those DNA molecules, we need to examine the fundamental properties of DNA. DNA comes in two forms, single-stranded (ssDNA) and double-stranded (dsDNA). It is a linear molecule made up of nucleotides; each nucleotide has a charge of -1 and consists of a base (guanine, adenine, cytosine, or thymine), a sugar, and a phosphate group[41]. Double-stranded DNA forms a double helix and is roughly 2 nm wide[42]. Each base pair unit is roughly 3.4 Å (or 0.34 nm) long[41].

Most genomic analyses require DNA molecules (or “fragments”) to be sorted by size. Since each nucleotide has a single negative charge[41], all DNA fragments have the same charge-to-mass ratio and cannot be separated in free solution under an electric field[41]. In free solution, longer fragments have a greater charge q and experience more electrical force (Equation 2.1[43]), but they also have more mass and experience more drag (or fluid resistance[44]); hence the two effects cancel each other out and the fragments all move at the same speed[41].

$$\mathbf{F}_E = q\mathbf{E}; \mathbf{v} = \mu\mathbf{E} \quad (2.1)$$

Different length fragments can, however, be separated by an electric field in a physical collision matrix, for example, in agarose or polyacrylamide gel. Longer DNA molecules collide with the matrix more often than short DNA molecules and thus migrate at a slower speed (see Figure 11b) [41].

Our two biomolecule separation platforms use AAO nanopore array membranes and AAO-derived nanopost arrays as their collision matrix (rather than conventional gels), as depicted in Figures 9 & 10.

DNA migration through a collision matrix is normally organized into three regimes: Ogston sieving, reptation, and the plateau region. The migration mobility is predominantly influenced by the ratio of the DNA molecule's radius of gyration, R_g , and the matrix's void space (or pore size) (see Figure 11) [45, 46]. The radius of gyration of a molecule provides information about the overall diameter of the molecule in solution [47] (see Figure 11a).

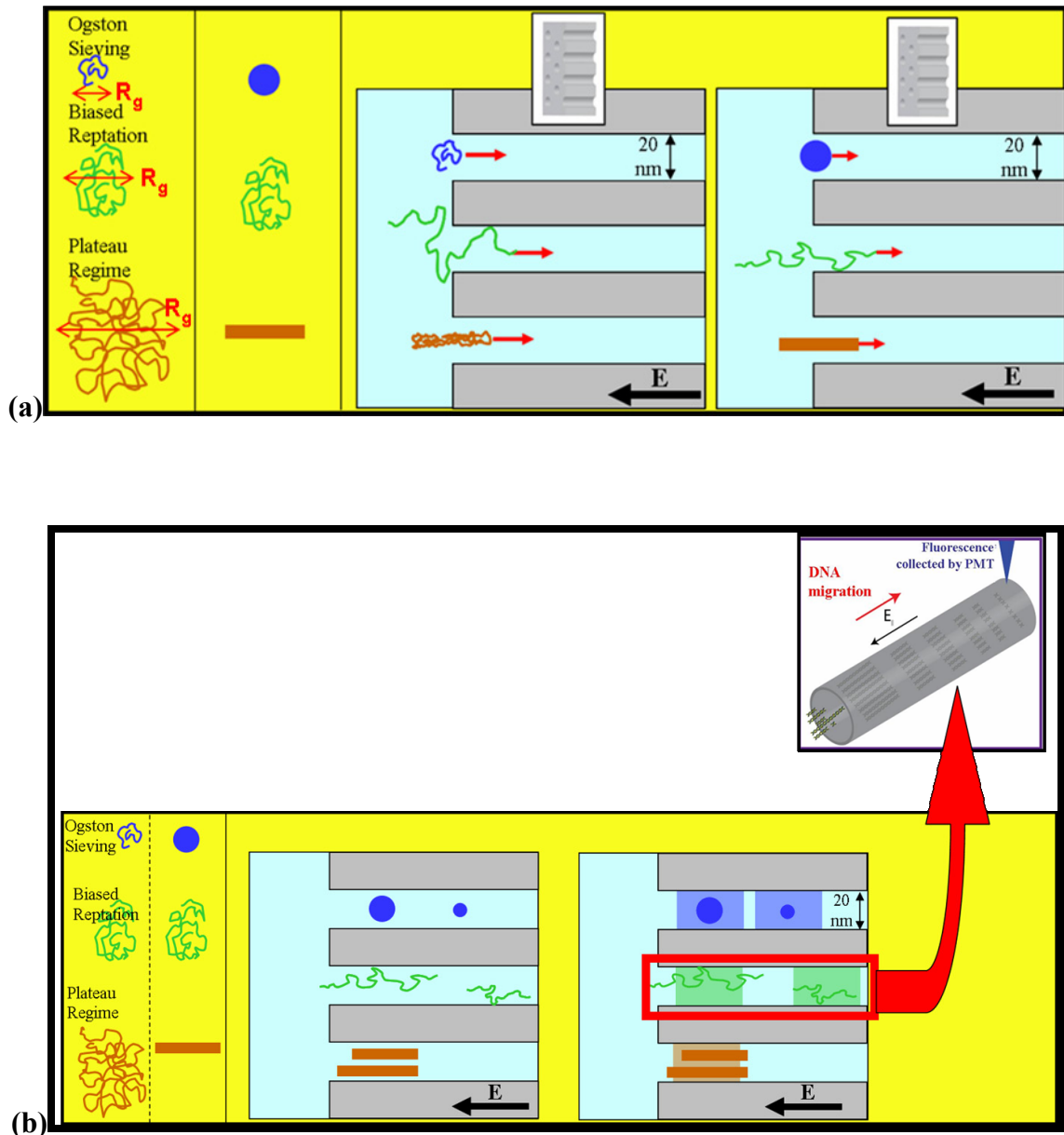


Figure 11: The three mobility regimes (Ogston sieving: shown in blue; biased reptation: shown in green; the plateau regime: shown in brown) for electrophoretic separation of molecules in a collision matrix. In this case, the collision matrix is an array of nanopores. (a) Depending on the radius of gyration [47] of the DNA fragments and the diameter of the collision matrix pores, a DNA fragment can be modeled as a sphere (Ogston sieving), a chain (biased reptation) or a rod (plateau regime). (b) As each regime features a different model for the molecule, it also features a different relationship between the fragment's electrophoretic mobility and the fragment's length (usually measured in terms of base pairs, or "bp"). A difference of one base pair will result in two fragments lengths (or "bands") with different mobilities in the case of Ogston sieving; the same 1 bp difference will result in a greater difference in mobilities in the case of reptation. That 1 bp difference will not result in a difference in mobility in the plateau region (and hence not result in a separation) [45, 46]. Differences in mobility can be measured in terms of the separation distance between the bands or the difference in time that it takes the bands to get to a fixed point (like a PMT detection slit).

In the Ogston regime, R_g is smaller than the matrix pore size and the migrating DNA molecule is treated like a sphere with radius R_g (shown in blue in Figure 11). The mobility (when the sieving matrix is a polymer gel) is described by[45]:

$$\mu = \mu_0 \exp(-K_R c) \quad (2.2)$$

where μ_0 is the free solution mobility of DNA, K_R is the retardation coefficient, and c is the concentration of the gel [45].

When the radius of gyration of the DNA molecule is larger than the pore size, sieving no longer works. Yet, experiments show that separation still occurs. Clearly, there must be another type of motion at work. This motion is known as reptation; here, the linear DNA molecules snake their way through the matrix (instead of traveling as a sphere) (shown in green in Figure 11). This motion is modeled as a random self-avoiding walk (see Figure 12) which is constrained by the collision matrix pore walls. The motion can be described by the Biased Reptation with Fluctuations (BRF) model. This model focuses on the Kuhn length of the DNA molecule and distinguishes between two different cases[45]. The Kuhn length of a polymer like DNA is the length at which the molecule can bend back upon itself (see Figure 12). The Kuhn length of DNA is approximately two times its persistence length (see Figure 12) [47]; the persistence length of DNA in electrophoretic buffer, defined as the length at which Brownian motion alone can bend the DNA molecule[47], is approximately 50 nm[48].

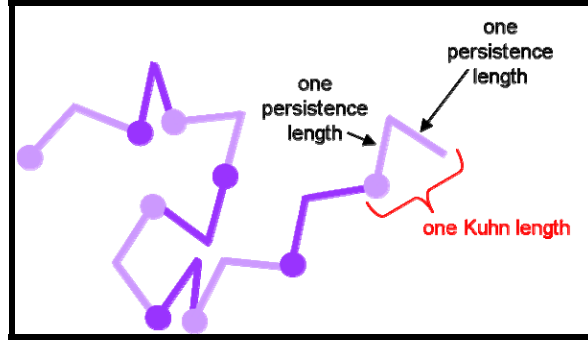


Figure 12: A diagram of a random self-avoiding walk model for polymers like DNA in the reptation mobility regime. The Kuhn length (a set of two persistence lengths) is shown [47].

In the first case of the BRF model, the Kuhn length is smaller than the pore size and the DNA molecule moves like a “flexible chain” and can reptate relatively easily. In the second case, the Kuhn length is greater than the gel pore size and the situation is described as a “tight gel” where reptation is more difficult. Both the “flexible chain” and “tight gel” cases predict an inverse relationship between DNA mobility and length:

$$\mu \sim \frac{1}{3N} \tag{2.3}$$

where N is the number of base pairs in a DNA fragment[45].

In the third mobility regime, a regime known as the plateau region, where the DNA molecule is long and/or the electric field is large, the mobility is independent of the number of DNA base pairs. The DNA is stretched in the direction of the electric field and the molecule is modeled as a rod (shown in brown in Figure 11); the mobility depends only upon electric force per unit length of molecule (which is independent of the

overall size, or basepair length, of the molecule). Separation is not possible in this regime[45].

Our Nanopore Array Platform features nanopore arrays with two different pore diameters: 20 and 50 nm. Our mobility regime expectations for these nanopore diameters depend on the radii of gyration of the DNA fragments we want to separate. We explored two different DNA ladders with our devices, HindIII-digested λ -DNA (consisting of 125, 564, 2027, 2322, 4361, 6557, 9416, and 23130 bp fragments) and 1 kbp ladder DNA (consisting of 0.5, 1.0, 1.5, 2.0, 3.0, 4.0, 5.0, 6.0, 8.0, and 10.0 kbp fragments (New England Biolabs, Ipswich, MA).

As the number of Kuhn segments in a DNA fragment is proportional to the number of base pairs, we can relate the radius of gyration to the number of base pairs [49, 50]. Our expectations for the HindIII-digested lambda DNA ladder, for example, are radii of gyration between 100 and 200 nm by the following logic: the smallest fragment size in the ladder (once discounting the two smallest sizes, 564 and 125 bp, which are not typically visible as the total amount of DNA for those fragment lengths in a typical sample is extremely small [51]) is 2,027 bp. The largest fragment size in the ladder is 23,130 bp. The radius of gyration curve values for the largest and smallest visible fragments fall between 100 and 200 nm [50].

This tells us that we can expect to be operating in the reptation or plateau mobility regimes for 20 and 50 nm nanopore devices interacting with the visible HindIII-digested

lambda DNA fragments. As the biased reptation regime gives us fragment separation and the plateau regime does not, we hope to find that the interactions between the DNA fragments and AAO nanopore walls obey the reptation model.

2.2.2 Protein Separation Theory

In order to understand the interactions between proteins (and the related molecules referred to as polypeptides and peptides[41]) and our engineered nanostructures and explore the ways in which those interactions can lead to the separation of those biomolecules, we need to examine the fundamental properties of peptides, polypeptides, and proteins.

Peptides, polypeptides and proteins are all polymers made up of amino acid monomers. Peptides are short chains of amino acids; polypeptides are long chains of amino acids which do not have a function on their own. Proteins are long chains of amino acids which are a functional unit [41].

Amino acids vary in charge, size, and shape, making the primary structure of proteins highly variable. The secondary structures of proteins (how the chain of amino acids folds locally) are determined by hydrogen bonds, ionic bonds, van der Waals attractions and hydrophobic interactions. Two particularly interesting secondary structures are alpha helices and beta sheets, two regular, repeating folding motifs which are primarily determined by hydrogen bonds. The spatial arrangement of the secondary substructures

determines a protein's overall three-dimensional shape, or tertiary structure. At this level, covalent disulfide bonds between different regions of the amino acid chain can come into play. If a protein is a subunit of a larger structure (a hemoglobin, for example), then the shape of the entire multi-protein complex is referred to as the quaternary structure[41].

Proteins in their native state can be sorted in many ways; typical strategies include sorting by charge, shape/affinity and size. Traditional sorting methods involve passing the proteins through a column containing a porous solid matrix. Examples of matrices include charged beads which retain proteins of the opposite charge, beads covered with an antibody or enzyme substrate that will bind a specific protein and gels which retain proteins smaller than the gel pore size[41].

For sorting proteins by size, there are two approaches. The first approach sorts native proteins by overall diameter and can be referred to as the sieving approach. There is a simple intuitive model of sieving and a more complicated model. The intuitive model of sieving is sufficient when the analyte particles' diameters are on the micrometer scale. In this model, when the analyte particles are larger than the pore size, they will not go through the filter (retention); when the analyte particles are smaller than the pore size, they will pass through the filter (elution). This simple model does not hold up at the nanoscale, however. At the nanoscale, the phenomena that occur at the filter-analyte interface can lead to retention of analyte molecules that are smaller than the filter pore size and elution of molecules which exceed the filter pore size. Some examples of filter-analyte interactions that complicate things are filter-induced analyte conformation

changes, electrostatic repulsions between a charged analyte and the charged pore wall, and hydrodynamic hindrance (nearby walls can generate additional drag forces on the analyte). Detailed models of these phenomena can be found in the work of Jongyoon Han et al.[52].

The second approach sorts denatured proteins by molecular weight (the electrophoresis approach). The most common version of the second approach is SDS-polyacrylamide gel electrophoresis, or SDS-PAGE. In SDS-PAGE, the proteins are suspended in an aqueous solution containing the powerful negatively charged detergent SDS. This detergent binds to the hydrophobic regions of the proteins, causing them to unfold in the aqueous solution and lose their secondary structure. SDS also masks any of the proteins' intrinsic charges. A reducing agent like β -mercaptoethanol is then added to the solution to break any S-S bonds in the proteins. At this point, the proteins have a linear structure, a net-negative charge and a uniform charge-to-mass ratio. The proteins can now be separated by length (or equivalently, molecular weight) with gel electrophoresis[41]. The migration of the proteins through the gel can then be modeled in the same way that DNA migration through gel is modeled [45].

As shown in Figures 9 & 10, our multi-gate Nanopore Array Platform uses AAO nanopore arrays to separate proteins by charge (by functionalizing the pore walls with a charged moiety), affinity (by functionalizing the pore walls with antibodies or enzymes) and size (by simple filtering or electrophoresis).

2.3 Our DNA/Protein Separation Devices

2.3.1 Nanopore Array Platform

Our work up until this point has focused primarily on DNA separation via electrophoresis; of the two DNA separation platforms (Figure 9), the Nanopore Array Platform has shown the most promise. The first Nanopore Array Platform devices we fabricated were single-gate devices featuring a single AAO membrane (see Figure 13). We have experimented with two different types of membranes: one with pores that are 20 nm in diameter and 60 μm in length, and one with pores that are 50 nm in diameter and 140 μm in length. We have also experimented with two different membrane orientations, horizontal and vertical (see Figure 14).

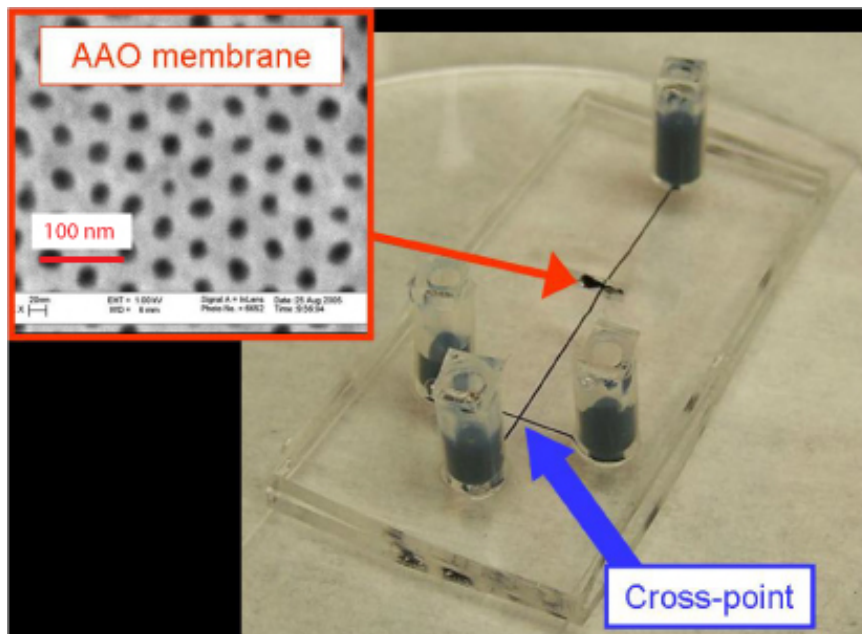


Figure 13: Single-gate Nanopore Array Platform separation chip. The right-hand image is a photograph of an actual chip. The left-hand inset is an SEM image of the actual AAO collision matrix prior to its insertion into the microfluidic channel. Overall chip dimensions: 20 mm (width) x 40 mm (length) x 2 mm (depth). Courtesy of Dr. Jin Ho Kim at Brown University.

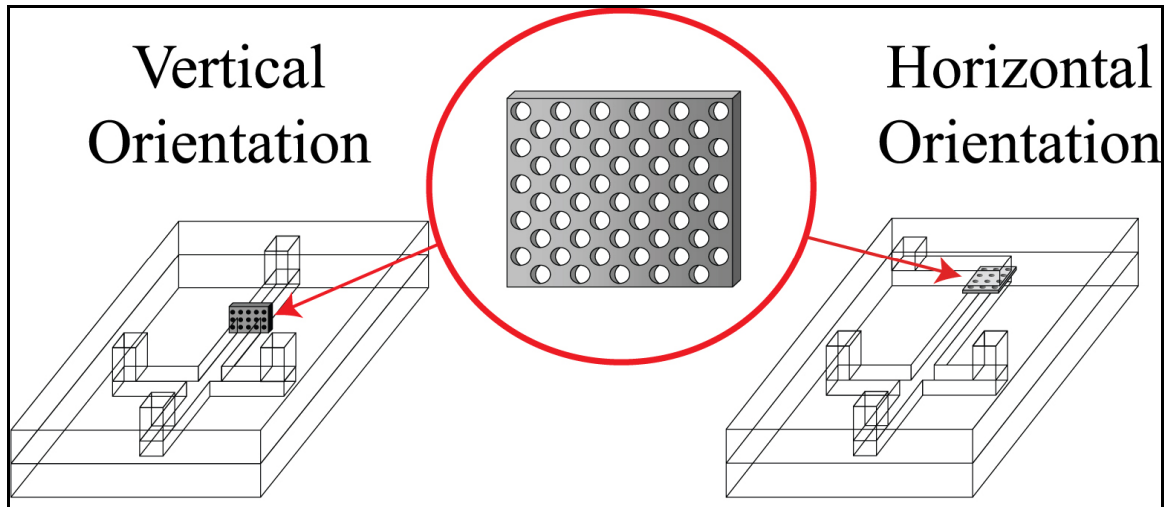


Figure 14: Comparison of vertical and horizontal AAO orientations (the microchannels and nanopores are exaggerated in the diagram).

Figure 13 shows our most successful chip; this chip employs a vertically-oriented 20 nm diameter membrane and has the following overall dimensions: 20 mm x 40 mm x 2 mm. This fluidic chip has elastomer poly(dimethylsiloxane) (PDMS) channels that are 200 μm in width and 50 μm in height. The AAO membrane is placed 15 mm from the cross-point.

2.3.1.1 Fabrication

Figure 15 shows the fabrication method, pioneered by Dr. Jin Ho Kim at Brown University, for our most successful chip.

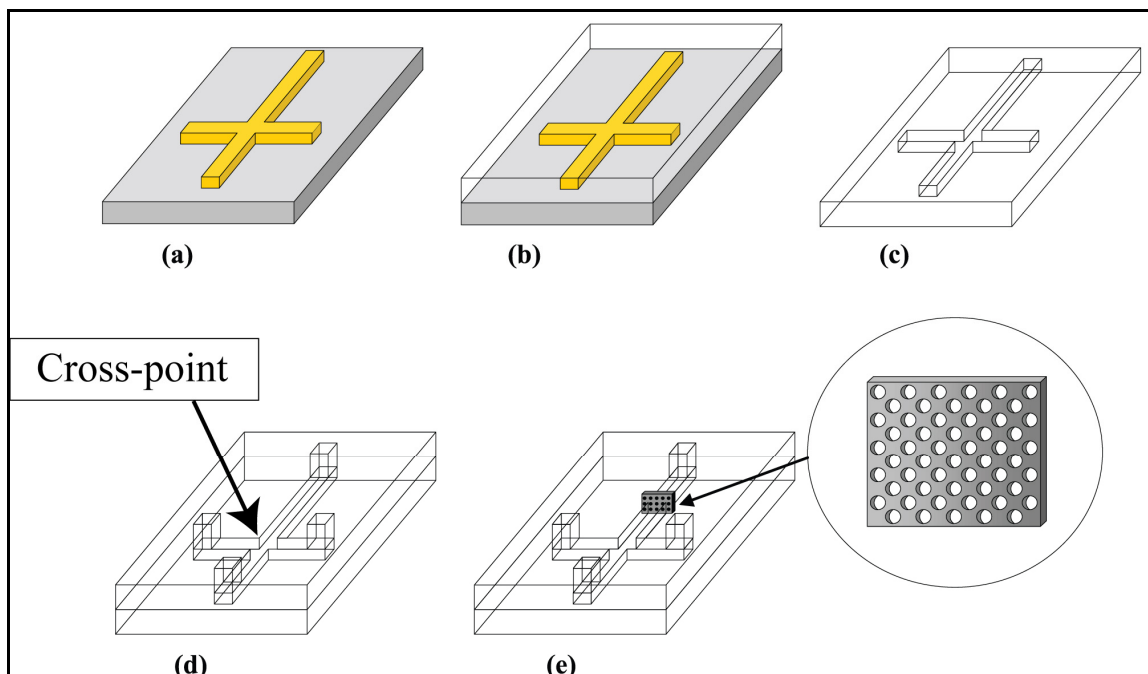


Figure 15: Fabrication steps for vertically-oriented AAO Nanopore Array Platform microfluidic chips (the microchannels and nanopores are exaggerated in this diagram). (a) Create a cross-shaped SU-8 mold on a silicon wafer using standard photolithography methods. (b) Pour PDMS solution over the SU-8 mold and cure the PDMS. (c) Peel off the cured PDMS and flip it over (revealing the microchannels). (d) Close the microchannels by covering them with a pre-made PDMS coverslab. (e) Make a cut in the longest PDMS microchannel with a razor blade, insert the AAO membrane, and seal carefully with PDMS.

This world’s-first manual incorporation of a vertically-oriented nanopore membrane into the separation channel of a microfluidic chip allows for multiple nonlithographic “gates” (with a theoretically unlimited range of diameters[10]) to be placed in sequence, allowing the device to sort a theoretically unlimited range of biomolecule analytes.

2.3.1.2 Experimental Procedure and Detection Method

Figure 16 shows the experimental setup for electrophoretic separation of DNA molecules with the Nanopore Array Platform. In brief, the fluorescently-labeled DNA sample was injected into the separation channel and driven through the AAO collision matrix with a

combination of pressure and electrokinetic force [53]. The eluting DNA bands' intensities were measured as a function of time with a photomultiplier tube (PMT) and then converted into electropherograms. In this scheme, the fastest-moving DNA fragments are detected first. Each intensity peak in the electropherogram represents a band of DNA moving by the PMT detection slit.

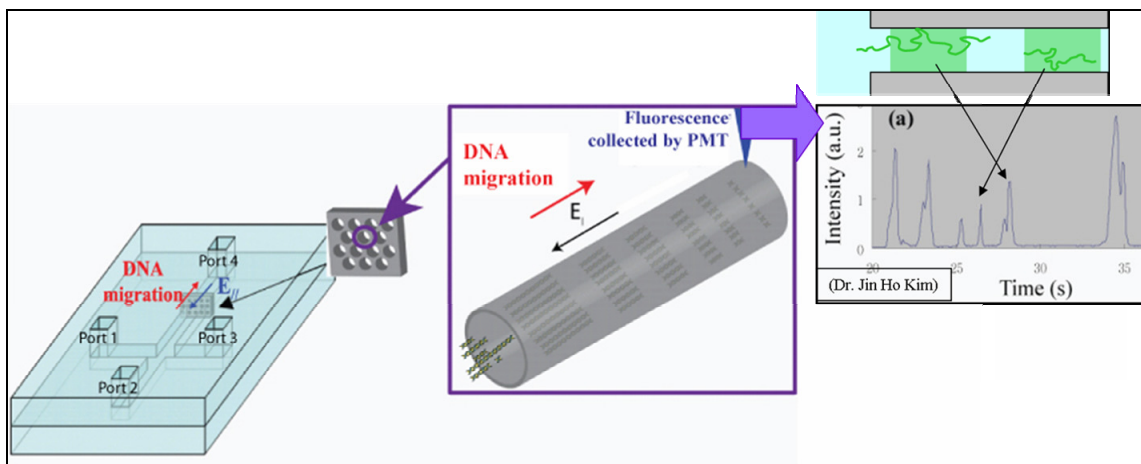


Figure 16: A schematic of the experimental setup for the Nanopore Array Platform (the microchannels and nanopores are exaggerated in the diagram). The fluorescently labeled DNA is detected by the PMT (photomultiplier tube) as it passes a fixed point. The smaller DNA fragments move faster in the pores (have fewer collisions with the walls) and thus are detected first. Intensity vs. time electropherogram plot courtesy of Dr. Jin Ho Kim at Brown University.

An inverted fluorescence microscope system to observe the DNA movement in the microfluidic channels; an 8-channel high-voltage and pressure controller was used to drive the DNA movement with a combination of pressure and electrokinetic force [53-57] (see Figures 17 & 18).

In our experience, one of the most important things in microfluidic DNA separation experiments is a carefully controlled simultaneous launch of all DNA fragments. There are many microfluidic methods for controlling the release of DNA fragments in the

literature; the two main methods are referred to as gated injection and pinched injection. Gated injection is simpler; pinched injection requires a more complicated voltage design. Pinched injection, however, offers better control over sample volume[53] and was therefore the injection scheme on which we focused.

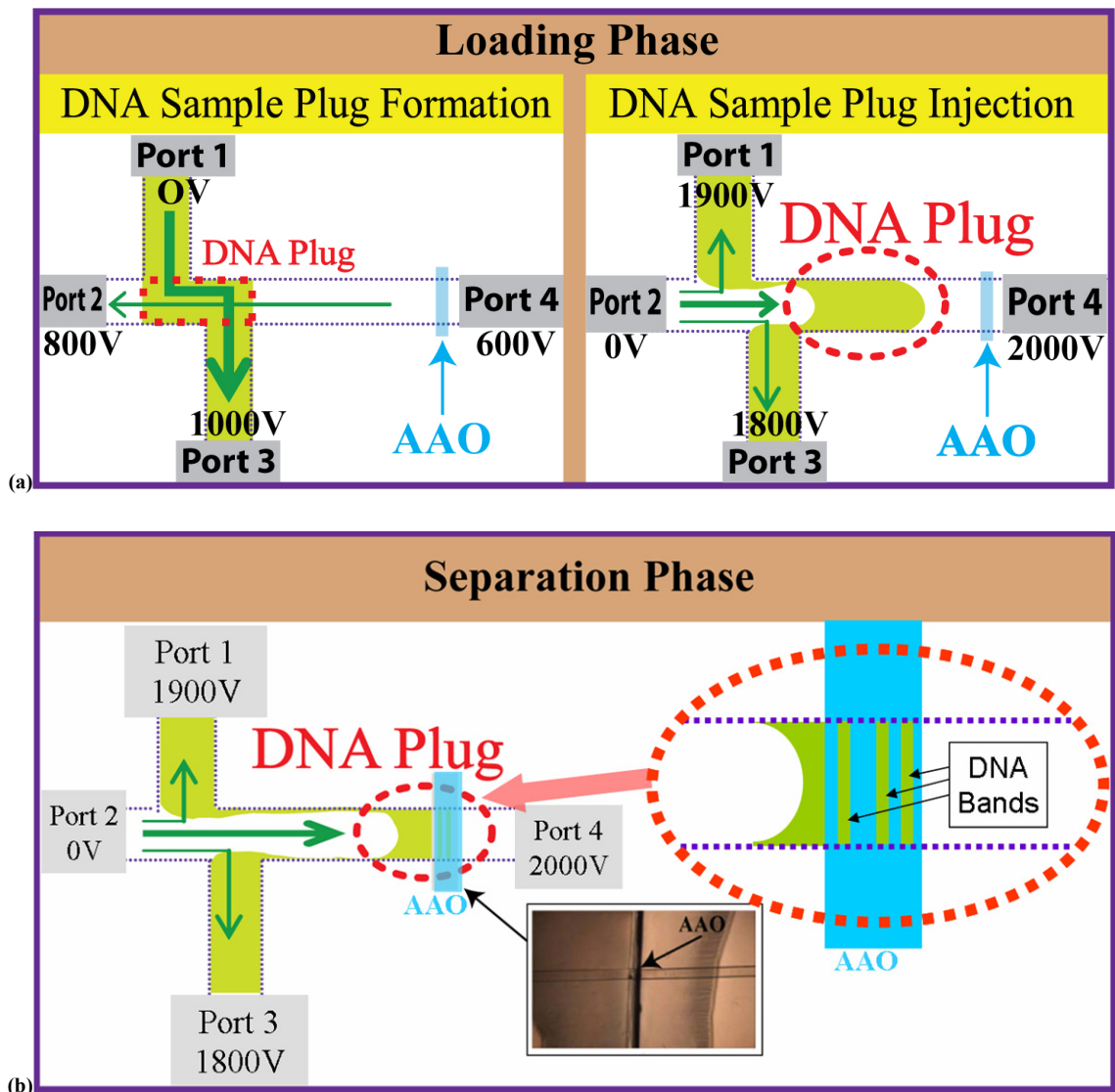
Generally speaking, all injection schemes involve two phases: (1) a loading phase in which a controlled amount of sample (commonly referred to as a “plug”, see Figure 17) is confined at the separation channel entrance and (2) a separation phase in which the analytes are sorted by their mobilities[57].

There are many channel geometries for sample injection in the literature [55-57], the most popular being the “simple cross” and “double-T” shapes [58]. We used a double-T design in our experiments as the offset between the inlet arm (Port 1) and outlet arm (Port 3) allows for precise geometric definition of and choices for a sample “plug” volume (unlike the simple cross design) [58]. The disadvantage of the double-T design is that the geometry is more complicated, resulting in more complicated fabrication procedures and more complicated electric field shapes and magnitudes at the junctions[58].

At the very beginning of the experiment, DNA sample (in buffer) is pipetted into Port 1’s silicone tube. Buffer (without DNA) is then pipetted into the silicone tubes of Ports 2 and 3. The loading phase then begins, starting with sample plug formation. The sample plug is formed by applying voltages to the ports as indicated in the left-hand diagrams of Figure 17a,c&d. The next step, plug injection, injects the sample plug into the separation

channel (using the voltage settings indicated in the right-hand diagrams of Figure 17a,c&d). The ports' voltage settings are kept the same for the separation phase (see Figure 17b).

The horizontal electric field in the nanopores during DNA plug injection and DNA fragment separation is approximately 800 V/cm (a voltage of 2000 V is applied across Ports 2 and 4 and the distance between Ports 2 and 4 is 37 mm).



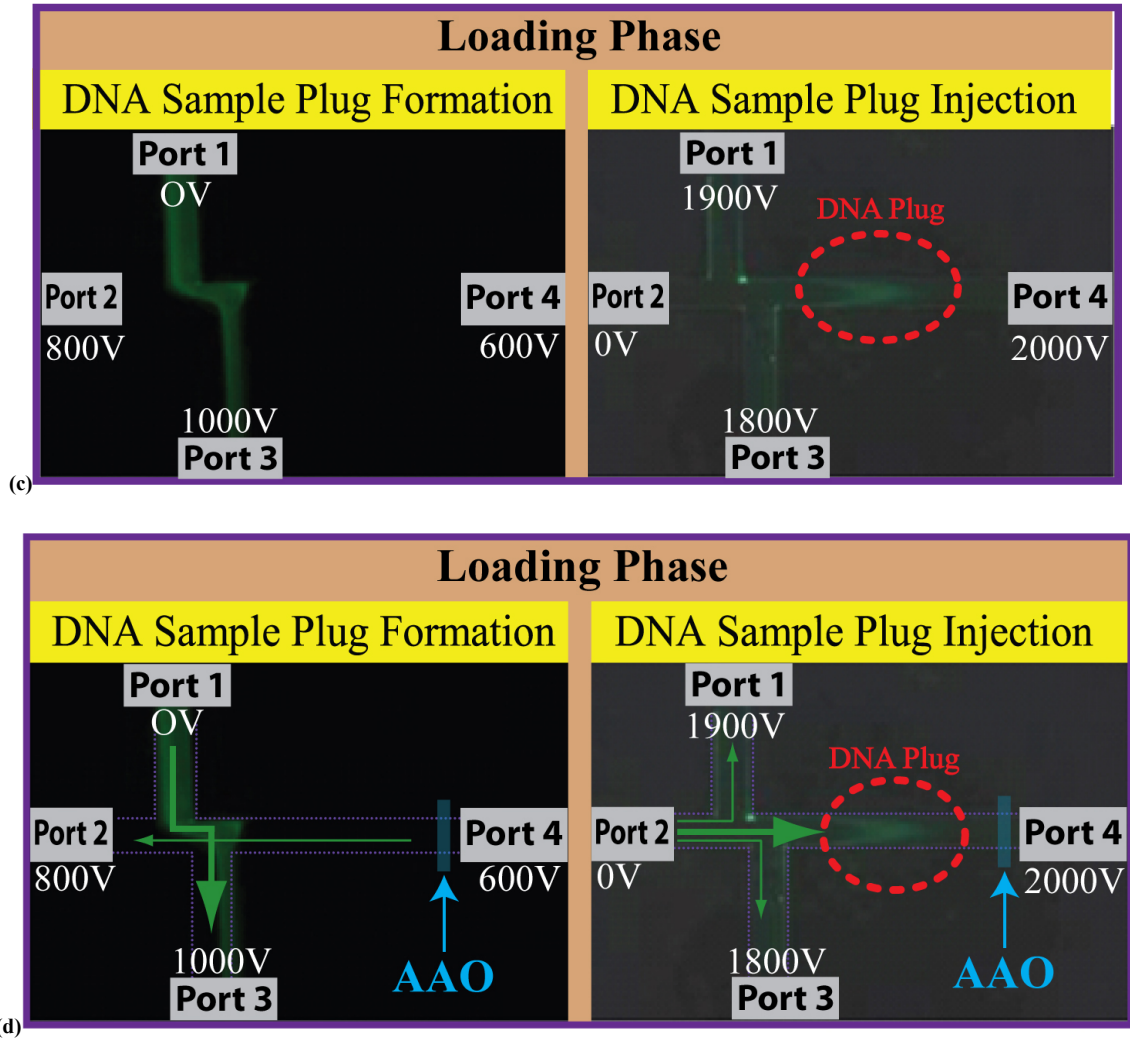


Figure 17: Pinched injection in a double-T microfluidic chip. (a) Cartoon of the loading phase. (b) Cartoon of the separation phase with a bright-field microscope image of an actual AAO membrane inserted into the microfluidic separation channel. (c) Fluorescent microscope images of the YOYO-1-labeled HindIII-digested lambda DNA sample during the loading phase. (d) Flow direction arrows overlaid over the image in (c). Images in (c) and (d) courtesy of Dr. Jin Ho Kim at Brown University.

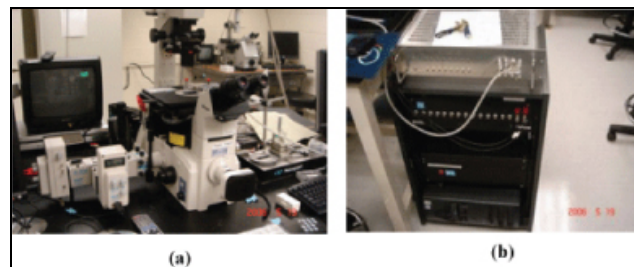


Figure 18: Detection system. (a) Photograph of inverted microscope system, (b) Photograph of 8-channel voltage controller.

All DNA samples were labeled with YOYO-1 iodide (Quinolinium, 1,1'-[1,3-propanediylbis[(dimethyliminio)- 3,1-propanediyl]] bis[4-[(3-methyl- 2 (3H)-benzoxazolylidene) methyl]]-, tetraiodide, Invitrogen Molecular Probes, Carlsbad, CA). Typical DNA sample concentrations were 1 µg/mL. In order to diminish electroosmotic flow, or EOF, which opposes field-directed DNA movement thus interferes with electrophoretic control of DNA, 0.5 X TBE was added to all buffer solutions and 0.5 wt% polyvinylpyrrolidone (PVP) was used in all solutions (including the buffer and DNA sample solutions).

Since PVP itself has been reported to act as a sieving material for DNA separation[22], we have run experiments verifying that the separation is indeed being done by the nanopore array membrane, and not by the PVP. Figure 19 shows electropherograms of DNA samples taken in the PVP medium just before the nanoporous membrane (at a point in the channel where the DNA has gone through PVP only). If the PVP medium were separating the DNA fragments, we would see multiple intensity peaks, or “bands”, in the electropherogram. Instead, we see one peak or “band”, indicating that the DNA fragments have the same mobility when they are in PVP medium only. The DNA fragments are not being separated by the PVP medium, hence the fragments are indeed separated by the AAO collision matrix itself.

2.3.1.3 Results

Figure 19 shows the results of our PVP control experiment.

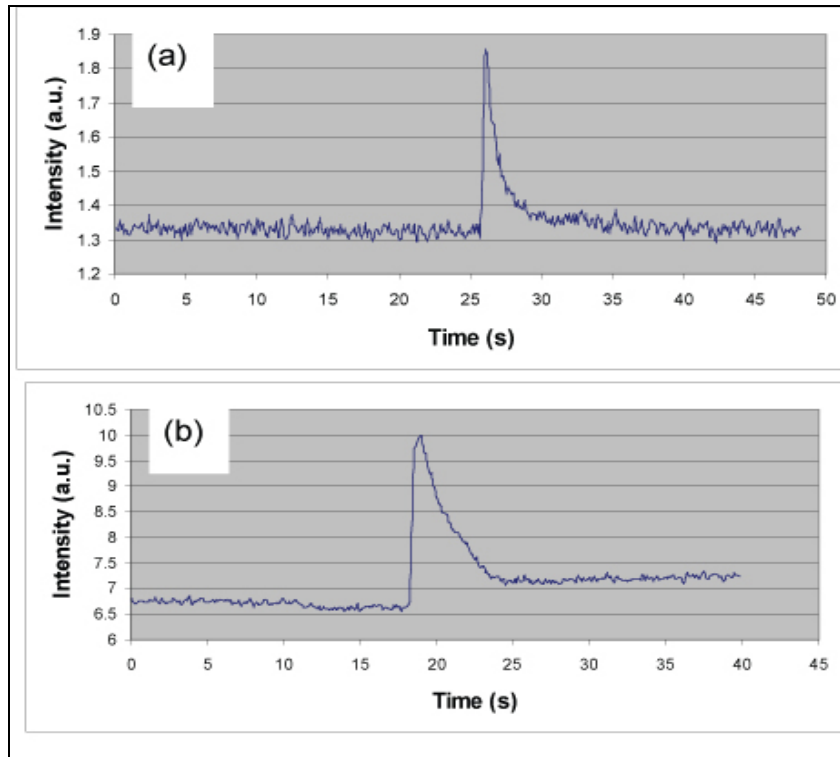


Figure 19: Control experiment electropherograms of both DNA ladders taken just in front of the nanopore array membrane (where the DNA has gone through the PVP medium only). (a) Hind III-digested λ -DNA (b) 1 kbp ladder. Courtesy of Dr. Jin Ho Kim at Brown University.

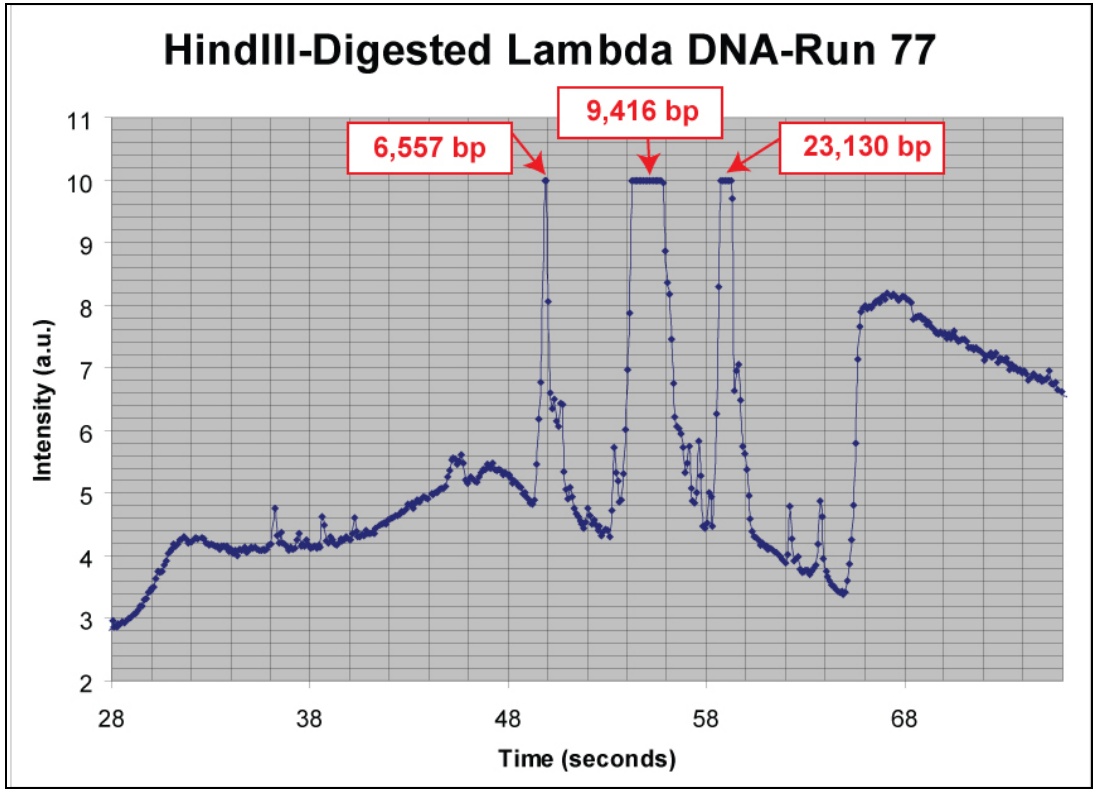
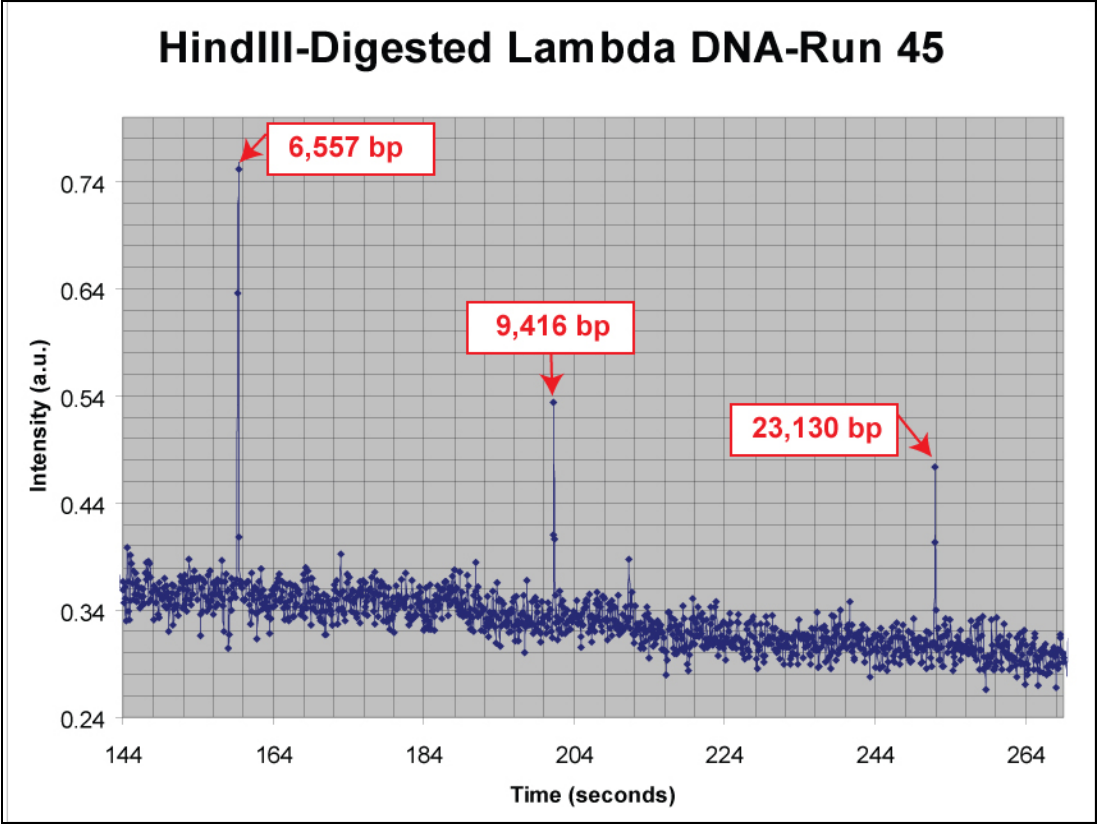
We now turn our attention to DNA ladders separated by our AAO nanopore array microfluidic chips. We found that when we used the 50 nm diameter nanopore arrays, we were not able to obtain clear separations for either DNA ladder. With the 20 nm diameter nanopore arrays, however, we were able to see separations for both DNA ladders.

This dissertation will focus on the results from the experiments with HindIII-digested lambda DNA. In order to examine how our data compared with the electrophoresis mobility models discussed in Section 2.2.1, we analyzed our electropherograms and plotted the log of the relative mobility of each fragment as a function of the fragment

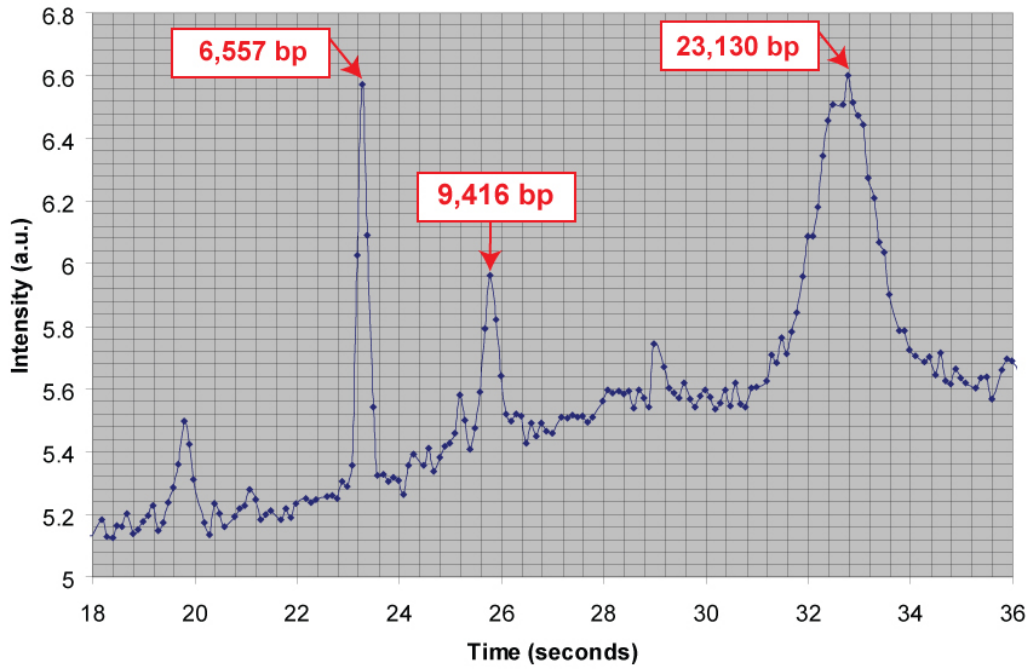
length (in terms of basepairs) for selected electropherograms. The selection criteria for the electropherograms is as follows: the microfluidic chip was new (had never been used), the microfluidic chip channels were rinsed with buffer immediately prior to the experiment and/or the DNA sample was switched from one ladder to the other ladder immediately prior to the experiment (for example, the sample was just switched from the 1 kbp ladder to the HindIII-digested lambda DNA ladder).

Out of approximately 50 experiments, or “runs”, 9 met the selection criteria (see Figure 20). Following the run selection, fragment sizes were assigned to intensity peaks with the following assumptions:

- the two smallest fragment sizes (125 and 564 bp) were assumed to not be visible[51].
- the more DNA of a particular fragment size there was in the original ladder sample (in terms of grams), the more emphasis was placed on assigning that fragment to a peak (for example, for every 1.0 μg of sample, there are 477 ng of the longest fragment and 42 ng of the smallest visible fragment[51], so a peak was always assigned to the longest fragment, but not always to the smallest visible fragment).
- the fragments were assumed to elute in the expected order (the longest fragment was assumed to come out last).

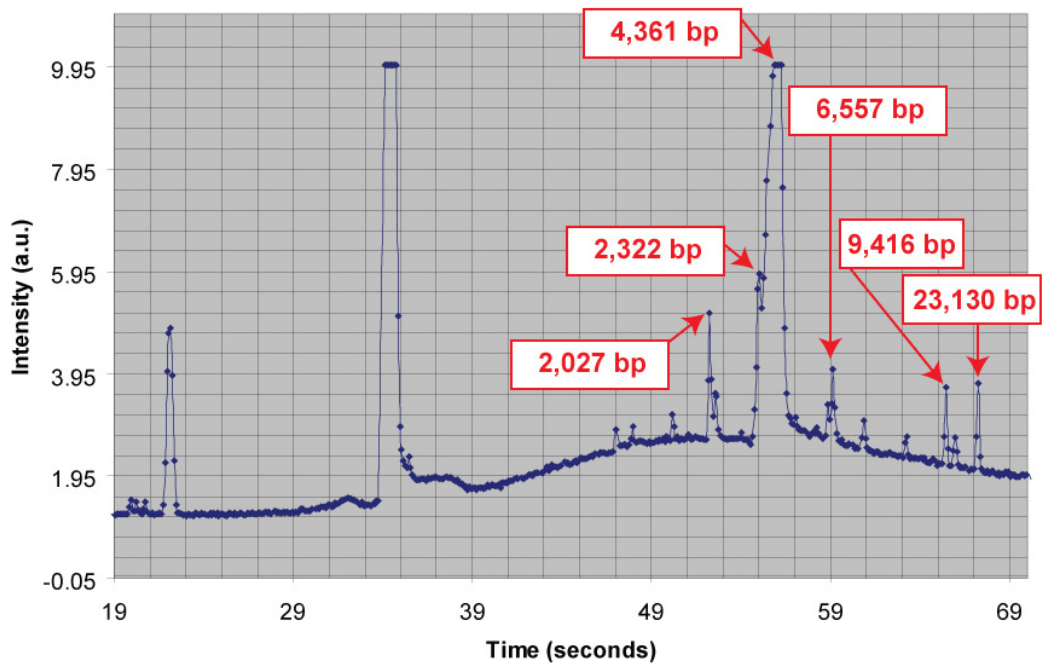


HindIII-Digested Lambda DNA-Run 194

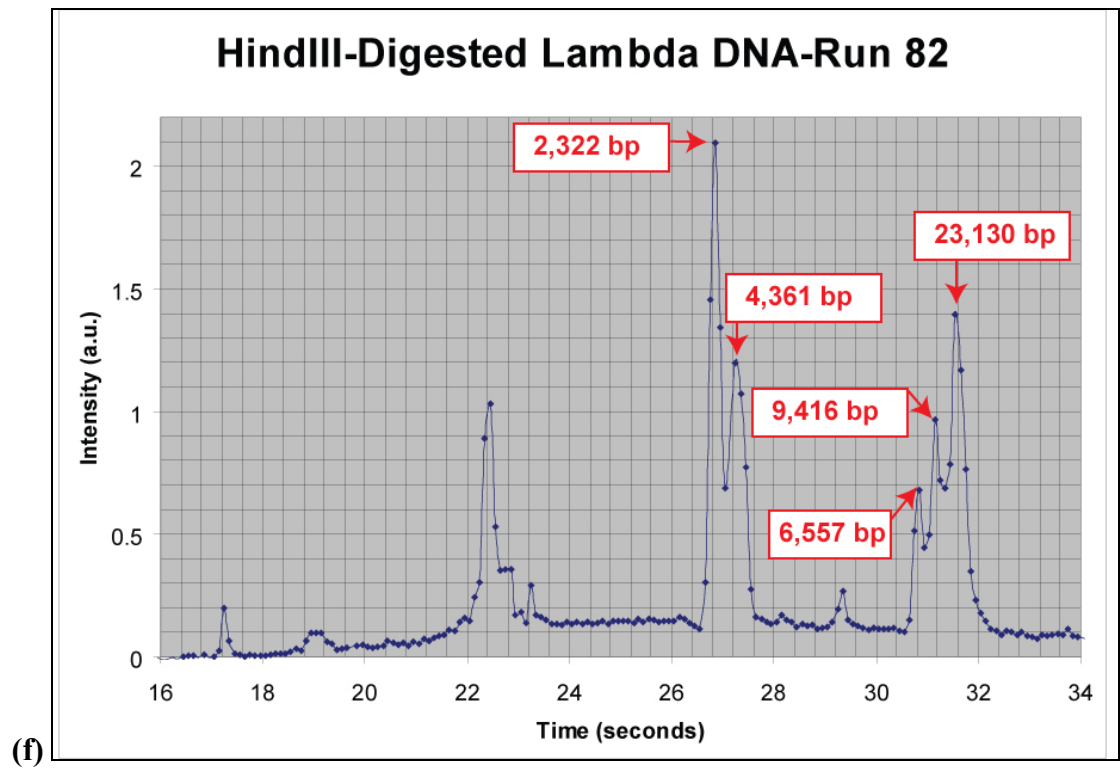
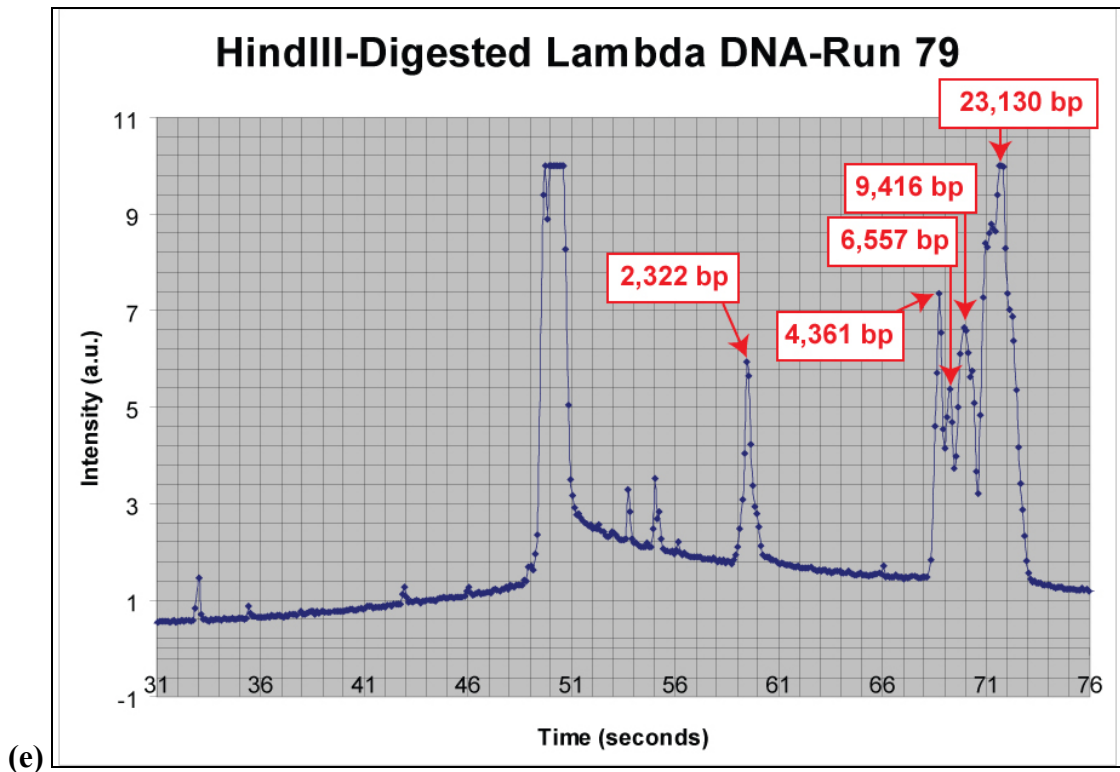


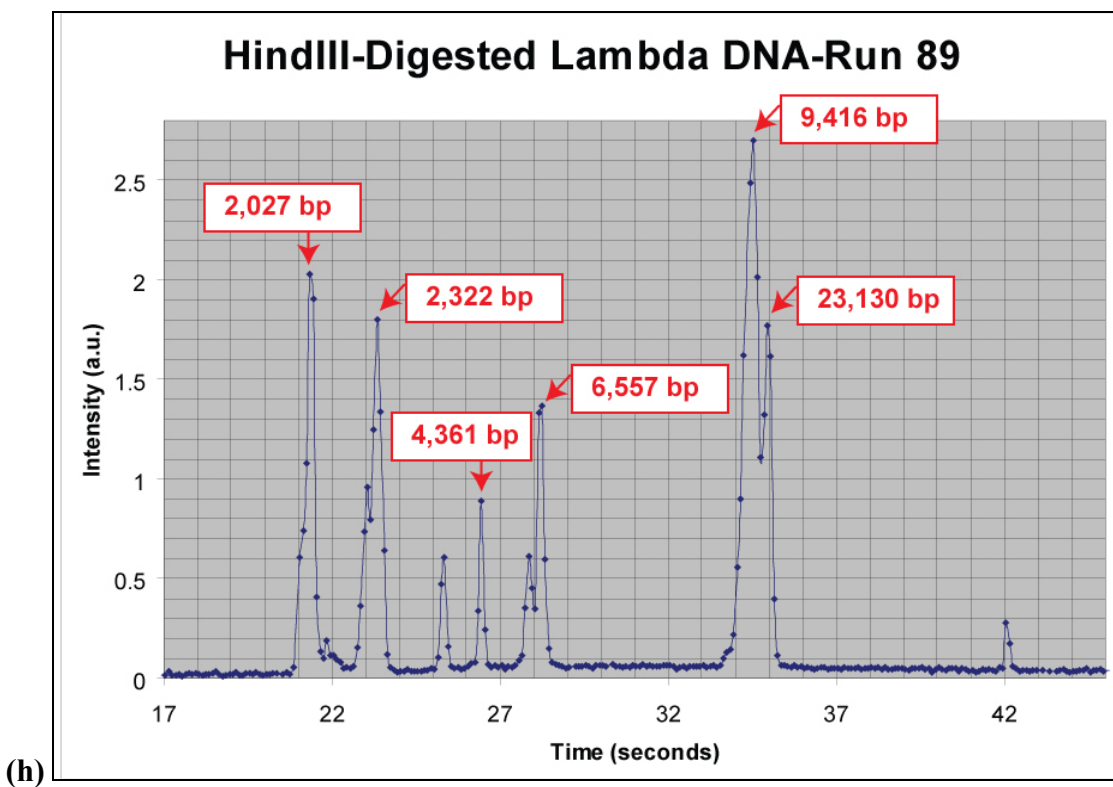
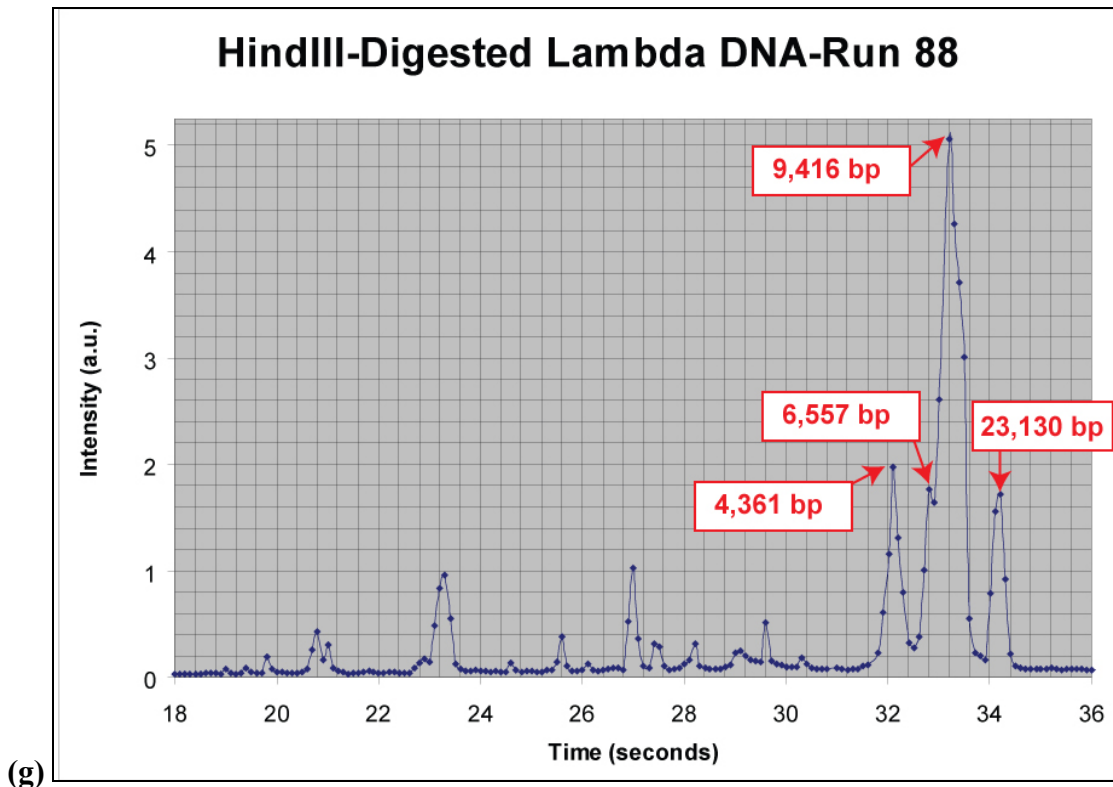
(c)

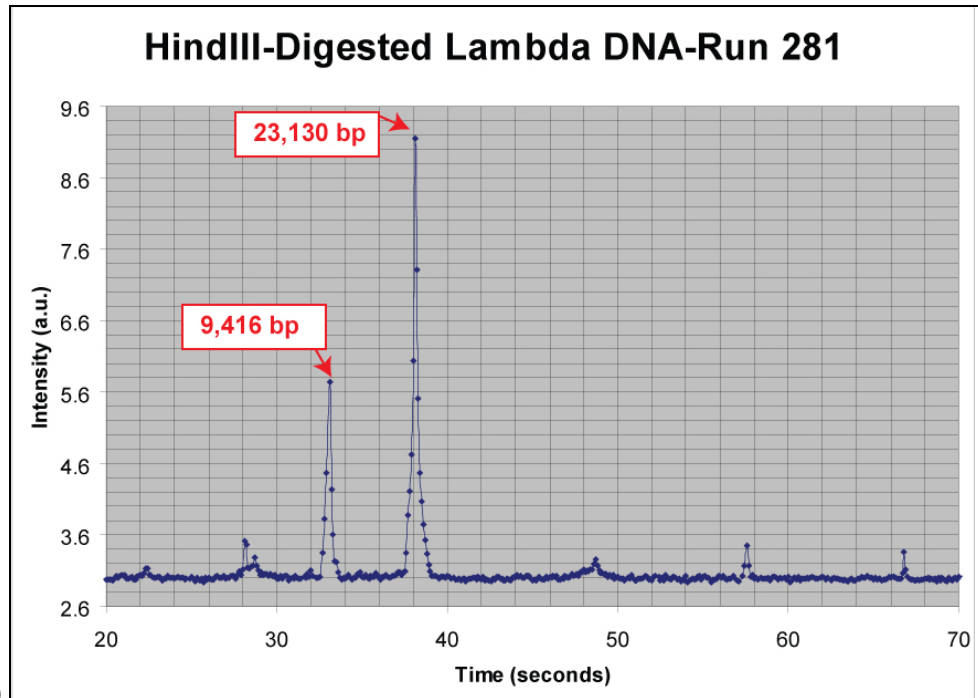
HindIII-Digested Lambda DNA-Run 78



(d)







(i)

Figure 20: Selected electropherograms from HindIII-Digested Lambda DNA experiments. The experiments are conducted with vertically-oriented AAO Nanopore Array Platform microfluidic chips (diameter of each nanopore: 20 nm, length of each nanopore: 60 μm). Electropherogram data gathered by Dr. Jin Ho Kim at Brown University.

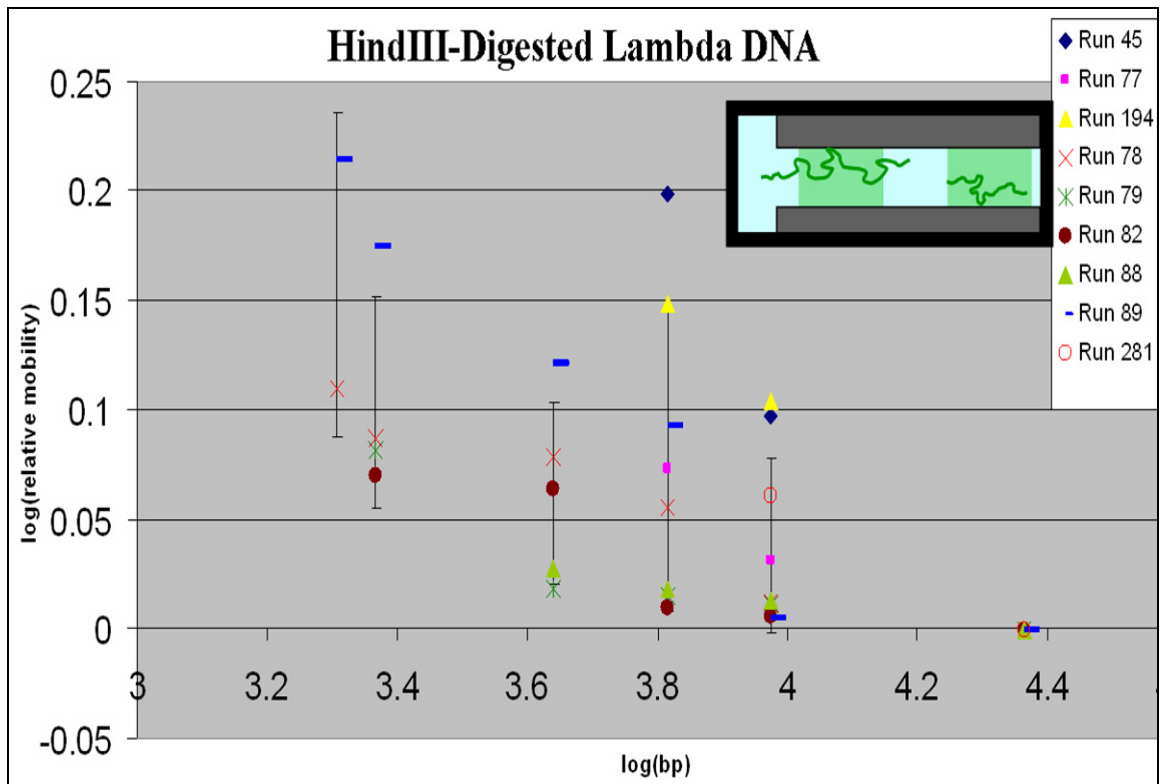


Figure 21: Mobility data from all selected HindIII-Digested Lambda DNA runs.

Excluding the runs with the fewest data points (Runs 45 and 194), we see that the plot becomes more consistent (see Figure 22).

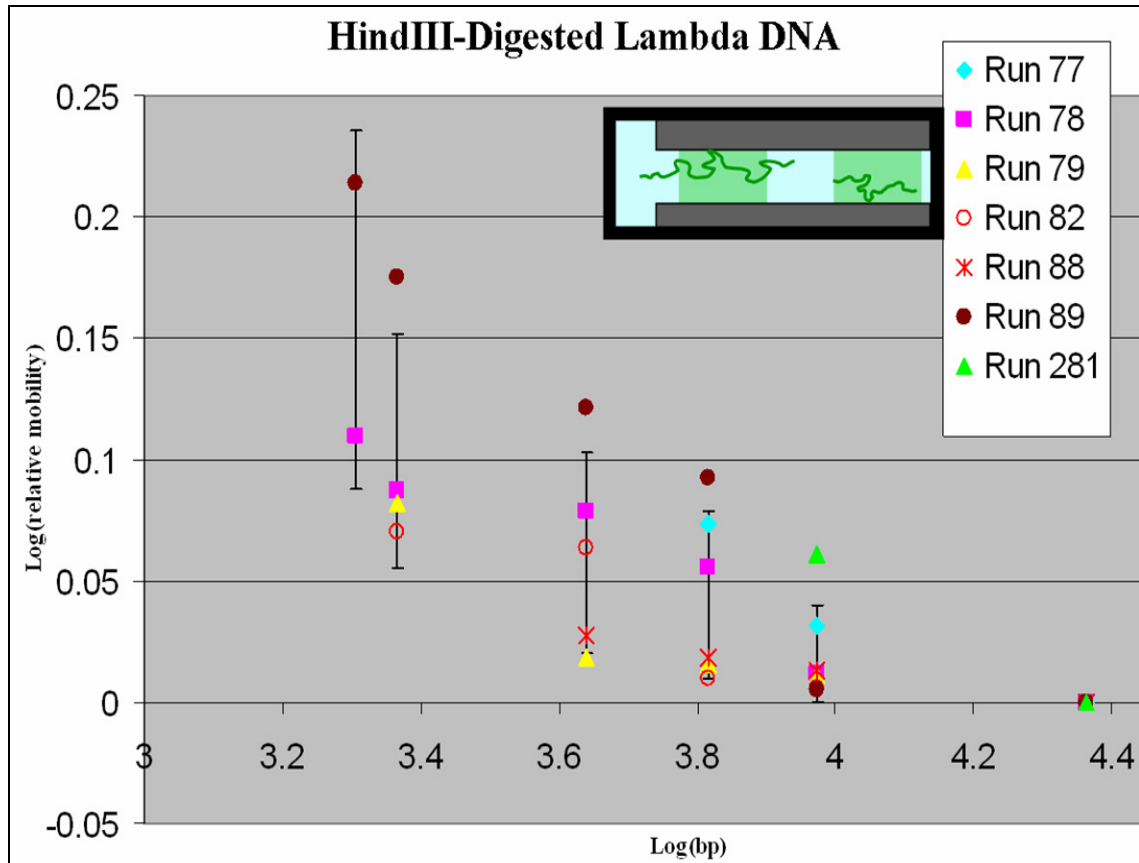


Figure 22: Mobility data from all selected HindIII-Digested Lambda DNA runs except for Runs 45 and 194 (the runs with the fewest data points).

This plot gives us some indication of what mobilities we see in our nanopore separation device, but we cannot yet conclude which regime we are in, as we do not yet have enough data or enough consistent data to draw meaningful slopes on our mobility plots and compare them to the slopes for the different regimes in the classic model [46]. The run-to-run differences that we have seen in our devices are not uncommon in nanofluidics [59] and can often be overcome by fine-tuning the experimental conditions and aggressively cleaning the chip before each run. We are taking these steps to improve our

reproducibility and move towards a full characterization of our electropherogram peak profiles and mobility data.

While our electropherogram profiles are not yet complete high-resolution separations, they are the world's first results for this type of approach and our devices are already extremely fast, sensitive and compact. On average, our HindIII-digested lambda DNA fragments were separated in approximately one minute. This is 30 times faster than commercial CE systems [60] and 20 times faster than microchip systems [61]. In our experiments, the typical volume of DNA sample being injected is 1 nL (200 μm channel width x 50 μm channel depth x 100 μm DNA band width). This is the same order of magnitude as microchip platform volumes [61]. In our devices, the typical amount of DNA injected is 1 pg. In commercial CE machines, it is typically ~ 2 mg [62]. In microchip platforms, ~ 0.1 g is injected [63]. Mature micron-sized Si nanopost platforms have separated ~ 10 ng DNA/hour as compared with our initial rate of 60 pg/hour [30]. Knowing our $S/N = 50$, we estimate the detection limit to be approximately 0.1 pg. In state-of-the-art CE, the detection limit is 20 pg [64]. Thus, our device operates with two orders of magnitude less DNA sample than CE machines [38].

2.3.2 Nanopost Array Platform

This platform, featuring an array of nanotubes (or other nanoposts) (see Figure 9), bears a close resemblance to the micropost arrays that have had remarkable success sorting DNA via electrophoresis[12]. There is a fundamental difference, however, between micropost platforms and nanopost platforms [65]. The scaling down of the posts and the inter-post

gaps brings the fluid–solid surface interactions into a new regime of fluidic transport in which the system manifests behavior drastically different from that seen in the micro counterpart. It also results in a tremendous sensitivity to nanoscale roughness (which can be ignored in micropost devices). This has a significant impact on the difficulty level of the fabrication aspect of these devices. The following sections discuss each nanopost prototype set, the problems encountered and our solutions.

2.3.2.1 Simple Chips

In the first prototype, we simply incorporated an AAO-templated carbon nanotube array into the polymeric, flexible, and transparent elastomer PDMS fluidic chamber (see Figure 23). In brief, an aluminum strip, the starting material for the CNT array, was placed on a glass slide. Next, PDMS solution was poured over the slide. After a two-hour curing at 70 C, the hardened PDMS was pulled off.

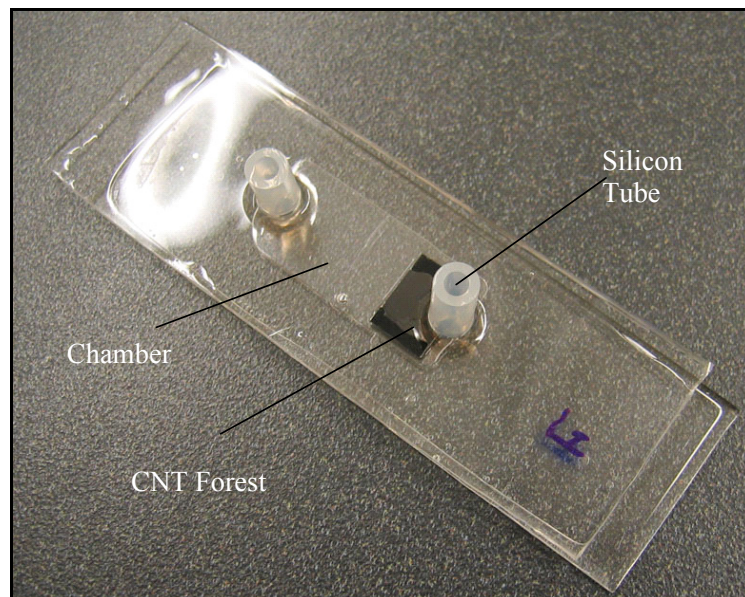


Figure 23: Photograph of the first Nanopost Array Platform prototype (“The Simple Chip”) for DNA separation via electrophoresis. The collision matrix is a carbon nanotube array. Buffer

solution and DNA sample can be introduced via the silicone tube input port, as can the electrodes.

This resulted in a PDMS chamber with an indent of the appropriate dimensions in which to place the CNT array. The CNT array was then fixed to the bottom of the PDMS depression. In order to create a sealed chamber, the CNT array-embedded PDMS was covered with a pre-made PDMS cover plate. The cover plate had two holes punched in it and silicone tubes glued above the holes for introducing buffer solution, DNA, and electrodes (for creating the electric field). The primary purpose of this prototype was to study the general properties of DNA in CNT arrays, such as the velocity of DNA and the adsorption of DNA onto the CNTs as the DNA moves through the array. As shown in Figure 24, because of the out-diffusion that naturally occurs at the DNA sample injection port, it was difficult to form a narrow band of DNA. This made it extremely challenging to discern the DNA dynamics in this prototype.

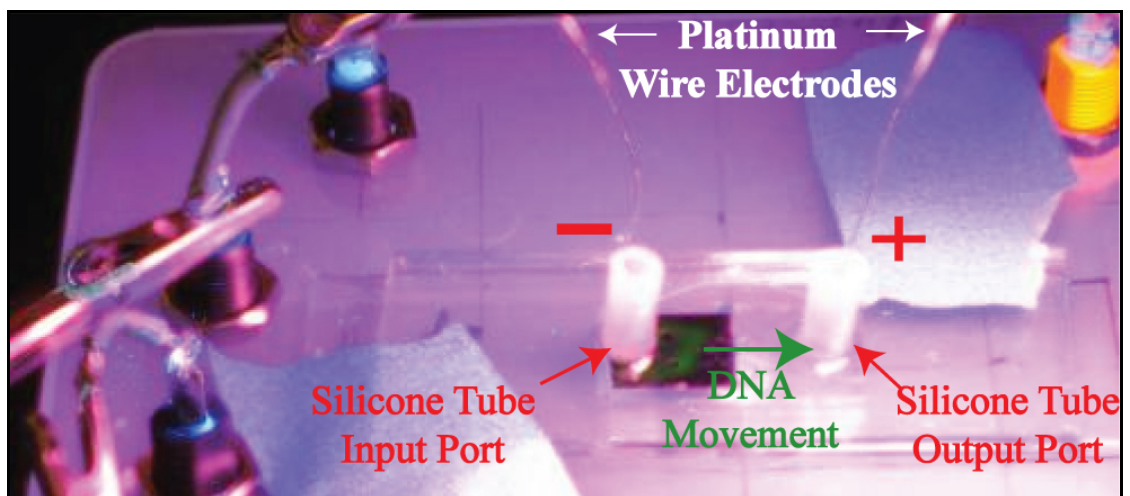


Figure 24: Photograph of the migration of fluorescently-labeled DNA (in green) within a UV-illuminated Simple Chip carbon nanotube array. A negative bias is applied to the input port and a positive bias is applied to the output port. The negatively-charged DNA fragments travel through the CNT array towards the positively charged electrode wire. The band pictured above is diffuse because of a post-electrophoresis pre-photo one-hour waiting time.

In the next prototype, we switched to the “starting line” design.

2.3.2.2 “Starting Line” Chips

Two thin platinum wires (125 μm) were stretched across the channel’s loading port and end port, as seen in Figure 25. A positive bias was then applied to the loading port wire, thus attracting the negatively charged DNA and concentrating the DNA at the starting line. In order to release the DNA at the beginning of each run, we reversed the bias, applying a negative potential to the starting wire and pushing the DNA away.

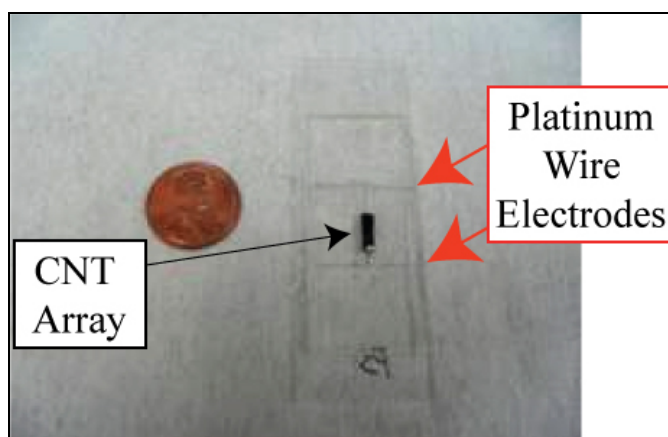


Figure 25: Photograph of a platinum wire “starting line” chip. The penny is included for scale.

As seen in Figure 26 (left image), we were able to concentrate DNA on the starting wire quickly and successfully. Releasing the DNA, however, was problematic, as seen in Figure 26 (right image). It took so long to push all of the DNA molecules off of the starting wire that the first DNA fragments released had already diffused into the forest before we finished “launching” the rest of the DNA fragments. In other words, the DNA

sample could not be launched all at once and diffusion took over, preventing distinct bands from forming.



Figure 26: Fluorescent microscope images of DNA in the “starting line” chip. Left: DNA concentrated on the positively-biased platinum wire. Right: DNA being released or “launched” when a negative potential is applied to the platinum wire.

While testing the above two prototypes, we encountered two major challenges in the study of DNA motion in a CNT array. The first challenge was forcing the diffusive DNA to remain gathered in a narrow band until it was launched. The second challenge was eliminating the free space, or gap, between the top of the nanotubes in the array and the PDMS cover plate, or “ceiling” (exaggerated for discussion purposes in Figure 27b).

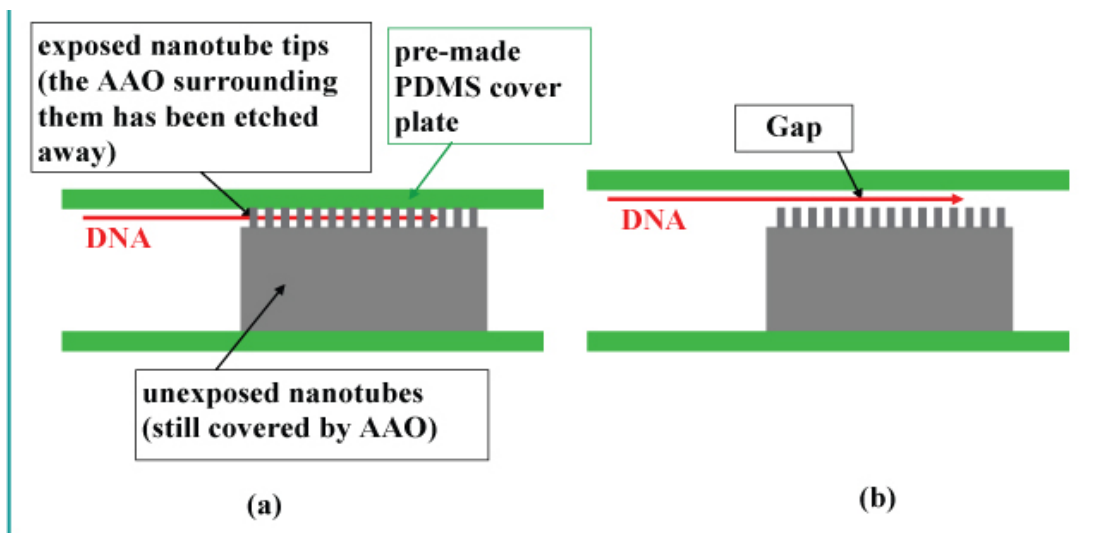


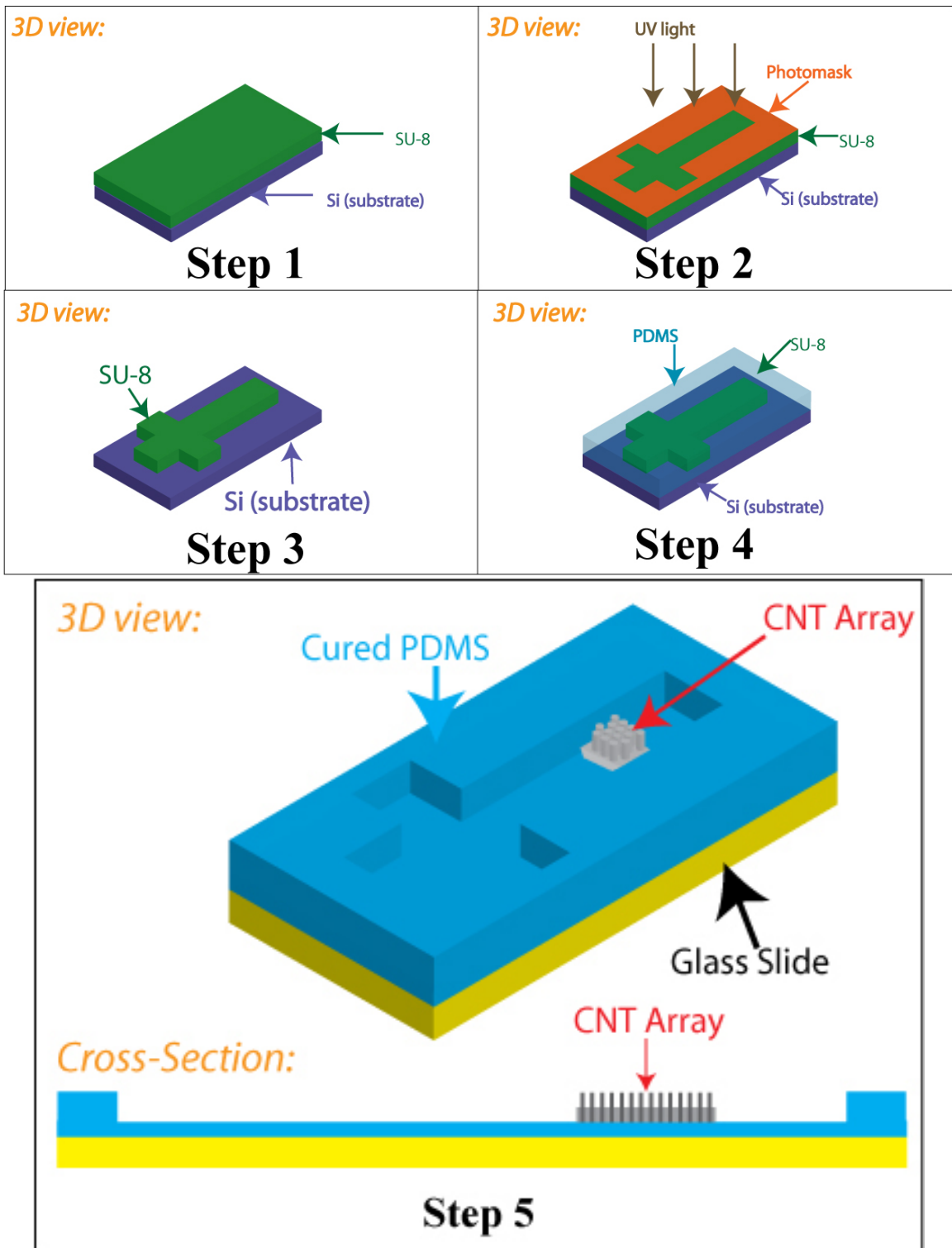
Figure 27: Illustration of the gap problem (exaggerated here for discussion purposes). (a) is an ideal nanopost array chip. (b) is a common mismatch that occurs in the fabrication process.

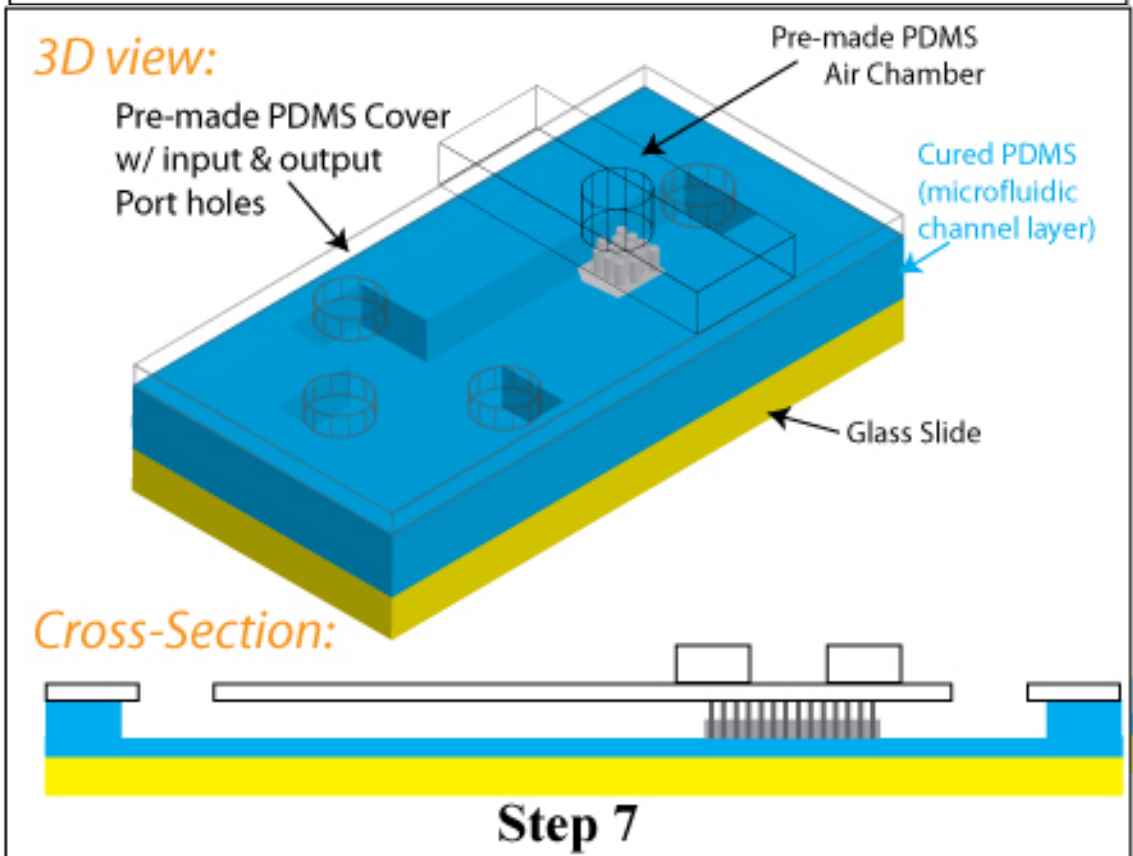
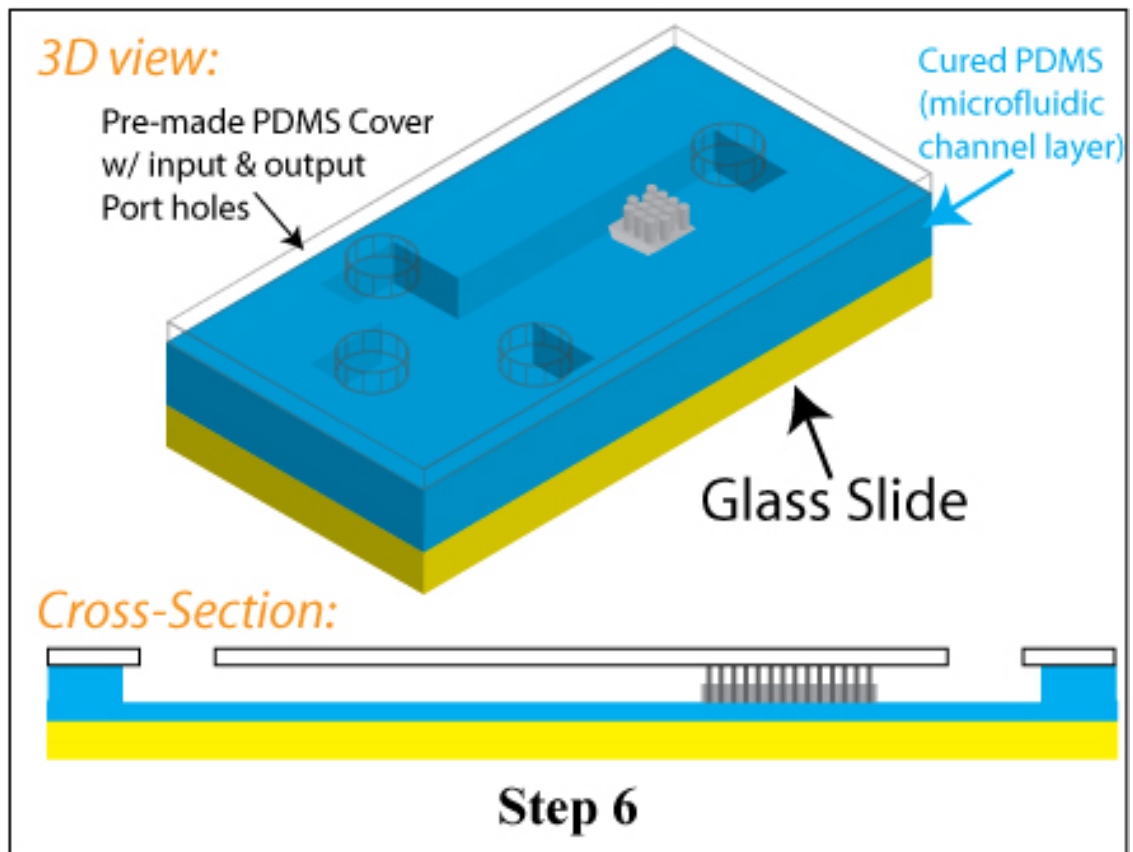
From the perspective of the DNA molecules, the unobstructed space, or gap, between the nanotube tips and the PDMS cover plate offers an easier path to navigate through than the spaces between the nanotubes in the CNT array. Accordingly, DNA prefers to go up and over the nanotubes instead of in between them. The difficulty in creating a perfect gapless chamber arises from the fact that the actual separating part of the CNT sample is the short exposed part of each nanotube (see Figures 7a,b & 27b). A mere few hundred nanometers of each nanotube is exposed in the wet-etching process. The PDMS chamber (and the total height of the CNT sample) is typically tens of microns deep. In our first prototype, we decided to use the aluminum strip to make the depression in the PDMS (which forms the chamber) because the aluminum strip is the starting material for the CNT sample. It is the aluminum strip that is anodized to make the AAO template which, in ideal conditions, determines the exact height of the sample. Indeed, the aluminum is very close in height to the final CNT sample, but it is not exactly the same. If, for example, the chamber ceiling is just 50 nanometers higher than the processed CNT sample, there is a gap that is roughly one quarter of the height of the actual separation matrix. Almost all of the DNA could flow through that gap and completely avoid the separation matrix. In order to overcome these obstacles, we designed and fabricated PDMS air chamber chips.

2.3.2.3 PDMS Air Chamber Chips

These chips have an expandable air chamber above the forest and inject a small amount of DNA sample and launch a narrow band of DNA into the CNT array. The general

fabrication procedure is shown in Figure 28 and a photo of a finished chip is shown in Figure 29.





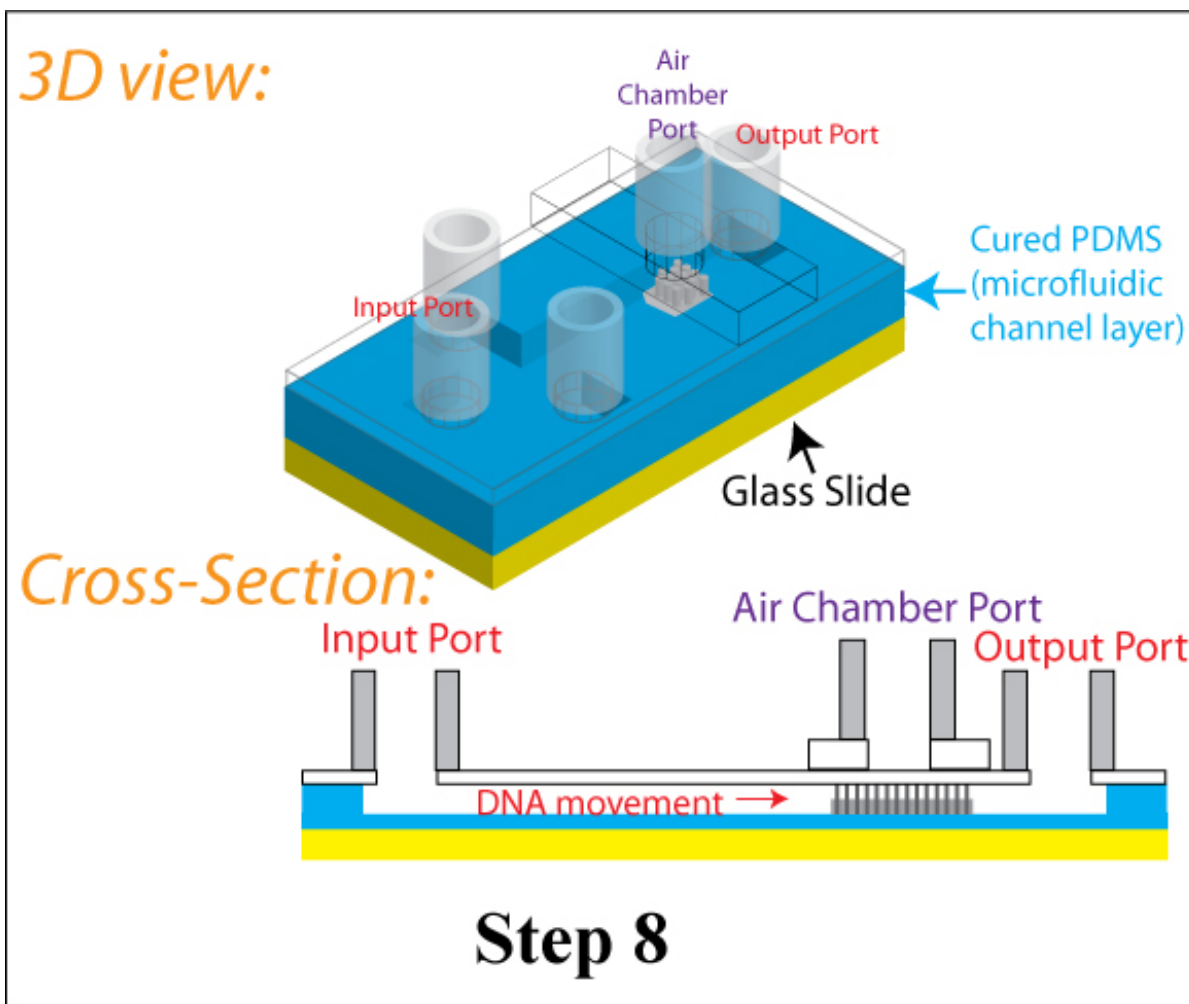


Figure 28: General fabrication procedure for PDMS air chamber chips (microfluidic channels and CNTs not to scale). In Step 1, a Si wafer substrate is coated with SU-8 photoresist. In Step 2, a photomask is placed over the SU-8 coated Si wafer. The photoresist is then exposed to UV light and the SU-8 is cured. Step 3 shows the shape of the cured SU-8 (after uncured SU-8 is removed). This cured SU-8 will serve as the master mold for poly(dimethylsiloxane) (PDMS) microchannel fabrication. In Step 4, uncured PDMS is poured over the mold and allowed to cure. The cured PDMS is then peeled off the mold and flipped over, revealing a cross-like depression (Step 5). The microchannels within this depression serve as pathways for DNA migration during electrophoresis. The carbon nanotube array collision matrix is then manually inserted (Step 5). In Step 6, the microchannels are covered with a pre-made PDMS coverslab. The PDMS coverslab has holes punched in it for input/output ports. The two PDMS layers will adhere to each other without any pretreatment (native PDMS is hydrophobic). The PDMS-PDMS seal is improved, however, by pretreating the layers with a Corona-Treater hand-held plasma generator. The oxygen plasma treatment creates Si-OH groups on the surfaces of both PDMS layers; this means that when the two layers come into contact with each other, the surface Si-OH groups react, forming covalent Si-O-Si bonds between the two layers. The oxygen plasma treatment also results in hydrophilic microchannel walls which are more compatible with aqueous DNA solutions. In Step 7, a plasma-treated pre-punched PDMS air chamber is placed atop the PDMS coverslab and allowed to bond. In Step 8, the silicone input/output port tubes are affixed with uncured PDMS. The PDMS is then allowed to cure.

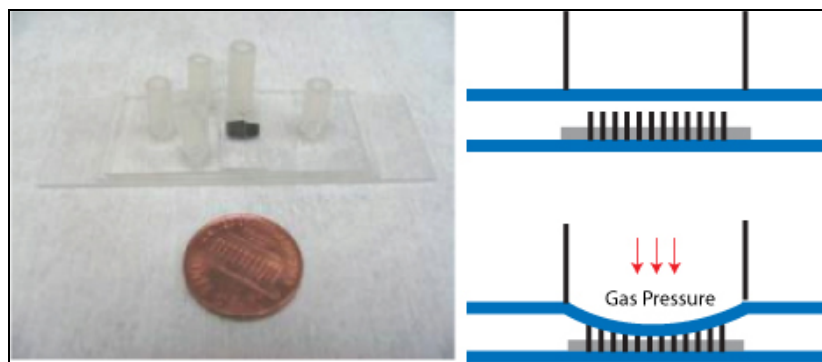


Figure 29: *Left: photograph of air chamber chip with a gap-closing PDMS air chamber. Right: schematic of the PDMS ceiling being pushed downward when pressure is applied via the air chamber. The bowing out of the PDMS ceiling closes the gap between the tips of the exposed CNTs and the ceiling (CNT array not to scale).*

In order to address the problem of overhead space (the nanoscale gap between the nanotube tips and the PDMS ceiling), we affixed a PDMS air chamber above the CNT array. Ideally, when we fill the air chamber with high pressure gas, the flexible PDMS cover slab bends, making contact with the CNT array and closing the gap. In this prototype, the gap was monitored by looking at the current at a constant voltage under external air pressure. We were able to remove the nanogap by applying air pressure to the air chamber (the current went abruptly to zero). The process, however, was irreversible; we could not fine-tune the degree of contact to ensure that the PDMS was neither deforming the nanotubes nor squeezing into the inter-nanotube spaces. We had additional difficulties with nanoscale gaps on the sides of the forests as the CNT arrays were hand-cut with a razor blade and manually incorporated into the microchannels. Due to the unavoidable variation in the size of razor-cut CNT arrays, we were not able fit them into microchannels without leaving some nanoscale gaps on the sides.

2.3.2.4 CNTs on Si, Si nanospikes, Au-NP coated CNTs, and CNTs anchored in PDMS

We attempted to solve the above problems by growing aligned CNTs directly on silicon without an AAO template; we expected this design change to make it easier to incorporate the forest into the chamber without leaving ceiling gaps and side gaps. We successfully fabricated aligned CNTs on Si wafers as large as 3” in diameter using Plasma-Enhanced Chemical Vapor Deposition (PECVD). As seen in Figure 30, the CNTs have a high degree of ordering in the vertical orientation, good uniformity and high density and are therefore well-suited to DNA separation. As the CNTs were grown on a Si wafer, one would expect them to be easily incorporated into microchannels with silicon microfabrication methods.

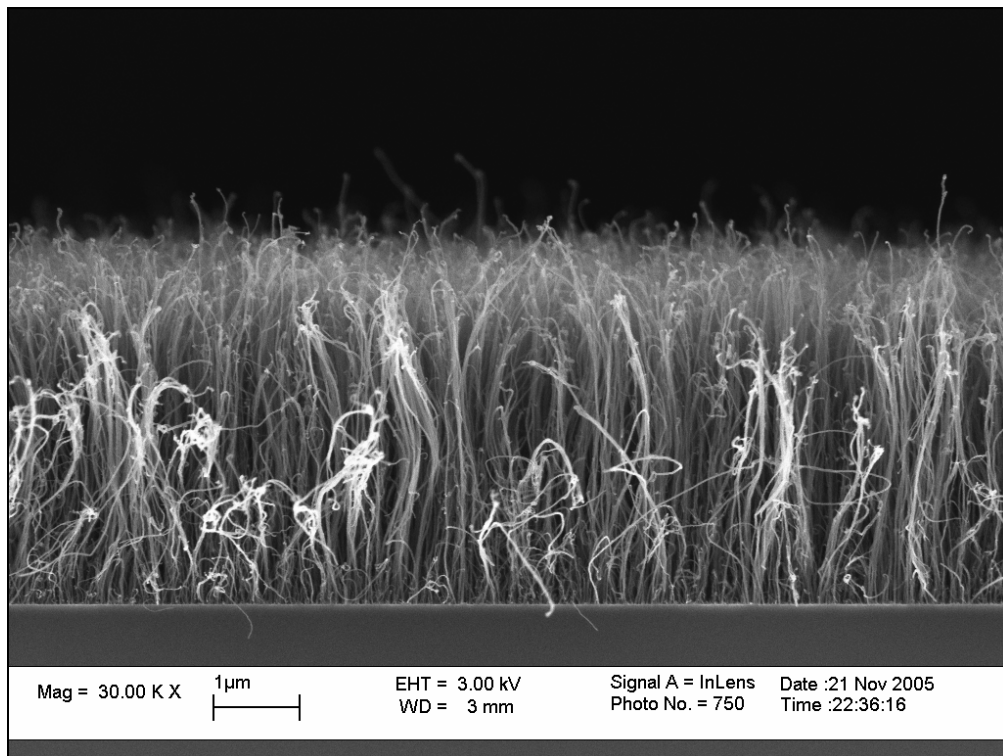


Figure 30: SEM image of aligned CNTs grown with PECVD. Courtesy of Chih-Hsun Hsu at Brown University.

In order to have more parameters to tune (i.e. surface chemistry, transformability, surface topology, and matrix material), we fabricated the following: silicon nanopike arrays for facile integration into silicon electronics, gold nanorod arrays for a broad range of chemical modifications of the separating surface, gold nanoparticle-coated CNT arrays for increased collision efficiency, CNT arrays embedded in elastomer polymer (PDMS) for transparency, and polymeric nanopost arrays for easy conversion to various shapes.

2.3.2.5 Directly Patterned Chips

In parallel, we worked on directly patterning microchannels in our carbon nanotube forests. The fabrication procedure for direct patterning is illustrated in Figure 31.

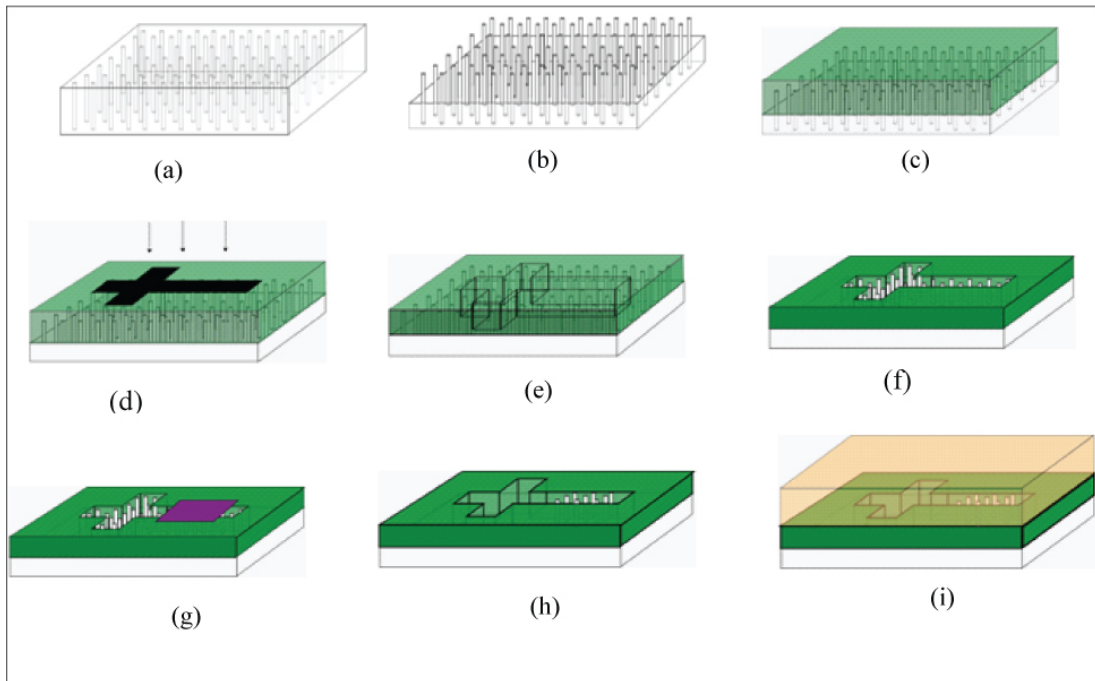


Figure 31: Diagram of direct microchannel fabrication on CNT arrays (the microchannels and CNTs are not to scale). (a) Original CNT array. (b) Tips of the nanotubes in the CNT array are exposed. (c) SU-8 is spin-coated onto the array. (d) The sample is illuminated through the cross-shaped photomask with UV light. (e) Here, the regions of SU-8 that were protected from the

UV-light are outlined. (f) Unilluminated regions of SU-8 are removed. (g) Square Reactive Ion Etching (RIE) etching mask is placed atop sample. (h) The unprotected CNTs are removed with RIE etching. (i) Pre-made PDMS coverslab is placed on top of the sample to close the SU-8 microchannels.

As shown in Figure 32, we have successfully fabricated microchannel structures onto CNT arrays.

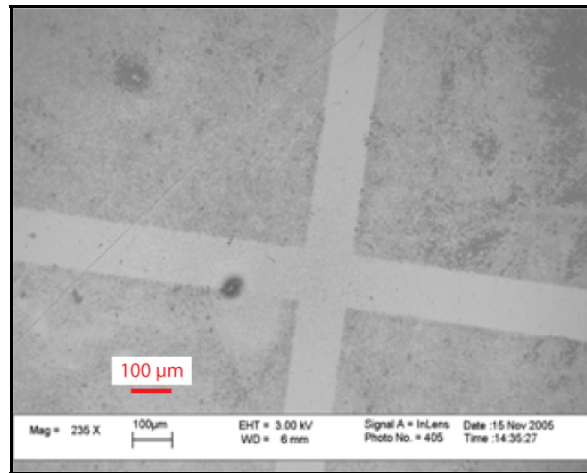


Figure 32: SEM image of direct microchannel fabrication on a CNT array. Courtesy of Dr. Jin Ho Kim at Brown University.

With this prototype set, the integrity of CNT forest became compromised and some of the microchannels became blocked (usually during steps (f) and (h)). We addressed these problems with more complex photolithography designs.

2.3.2.6 Complex Photolithography Chips

We made three types of complex photolithography chips: tunnel-type, upward-type, and downward-type. They are shown in the Figures below.

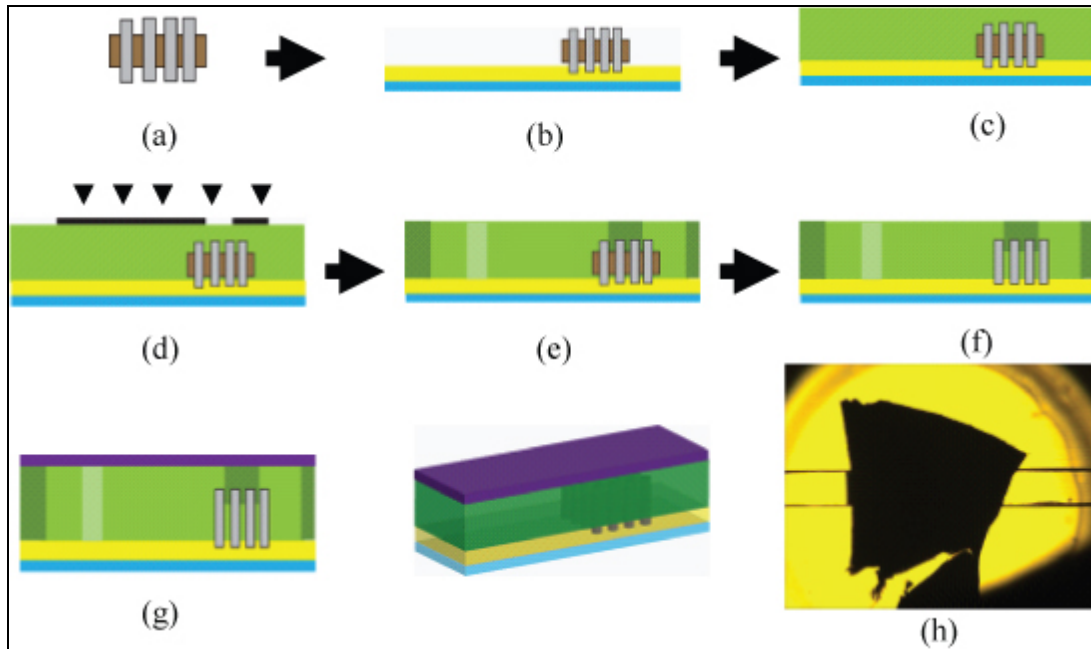


Figure 33: Diagram of tunnel-type complex photolithography chip fabrication. (a) The process starts with a CNT array etched (exposed) on both sides. (b) The CNT array is pressed into SU-8-coated glass. The entire sample is then exposed to UV light and developed. (c) SU-8 photoresist is poured over the sample. (d) UV exposure and development harden the second SU-8 layer through the modified cross-shaped mask. (e) The SU-8 is developed. The illuminated regions (shown in dark green) remain and the unilluminated regions (shown in light green) are dissolved. (f) The alumina (shown in brown) is removed using an etchant (typically a mixture of phosphoric and chromic acid). (g) The microchannels are covered with a pre-made PDMS coverslab. (h) Bright-field light microscope image of an actual tunnel-type complex photolithography chip, courtesy of Dr. Jin Ho Kim at Brown University..

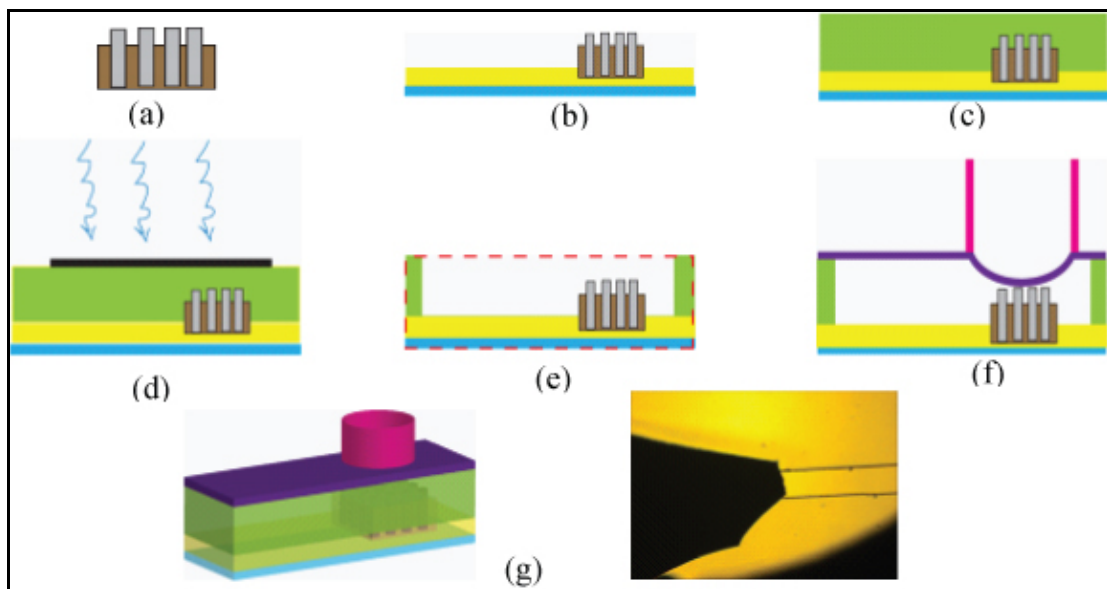


Figure 34: Diagram of upward-type complex photolithography chip fabrication. (a) The process starts with a CNT array (etched on one side only). (b) The CNT array is placed on SU-

8-coated glass and hardened with UV light and photoresist developer. (c) A second SU-8 coating is added. (d) The photomask is placed atop the sample and the sample is exposed to UV light. (e) The SU-8 photoresist is developed. (f) A pre-made PDMS coverslab and air chamber are placed on top of the PDMS microchannels. (g) Bright-field light microscope image of an actual upward-type complex photolithography chip, courtesy of Dr. Jin Ho Kim at Brown University.

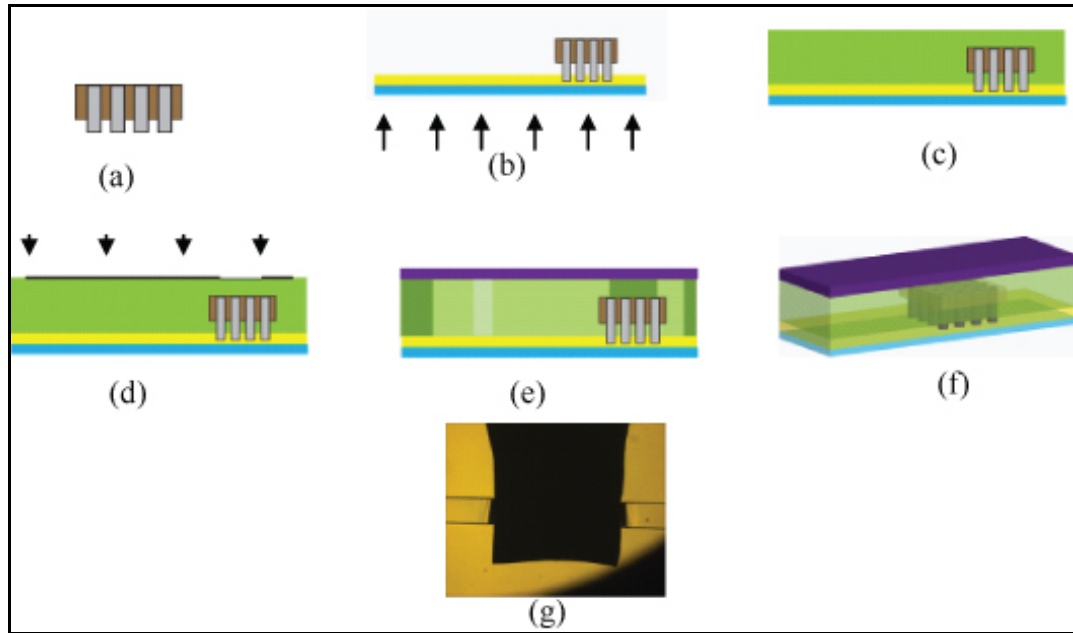


Figure 35: Diagram of downward-type complex photolithography chip fabrication. (a) The process starts with a CNT array etched on just one side. (b) The CNT array is pressed into SU-8-coated glass and hardened with UV exposure and developer. (c) A second SU-8 coating is added. (d) The photomask is placed on the sample and the sample is exposed to UV light. (e) The SU-8 is developed and the pre-made PDMS coverslab is placed on top of the SU-8 microchannels. (f) Bright-field light microscope image of an actual downward-type complex photolithography chip, courtesy of Dr. Jin Ho Kim at Brown University.

Using these more complicated photolithography approaches, we successfully incorporated CNT arrays into microfluidic channels without leaving any gaps. However, when we used conventional sealing methods (in which the SU-8 and PDMS cover plate are treated with plasma and pressed together), the adhesion force between the PDMS and the SU-8 was not sufficiently strong and the layers detached when we applied air pressure to fill the channels with buffer. As there did not appear to be a better method in the literature for joining PDMS and SU-8, we developed our own new sealing methods. In

preliminary tests, we saw a good seal form and observed stable fluidic movement under rather high air pressure without any delamination. Our sealing method was as follows:

- First, spin-coat a thin ($\sim 5 \mu\text{m}$) SU-8 layer onto the PDMS plate. The PDMS needs to be pre-treated with plasma so that the SU-8 spreads uniformly.
- Bake the SU-8-coated PDMS plate at $65 \text{ }^\circ\text{C}$ for 20 seconds and place it on the plasma-treated SU-8 microchannel structure.
- Cross-link the slightly hardened SU-8 with UV light, bake at $65 \text{ }^\circ\text{C}$ for 1 min, and then bake at $95 \text{ }^\circ\text{C}$ for 2 min.

After several tens of microfabrication trials, we succeeded in making a few chips with a good seal and unblocked fluidic movement. As soon as we tried to run DNA samples in these chips, however, we observed considerable bubble generation at the edge of the CNT tunnel.

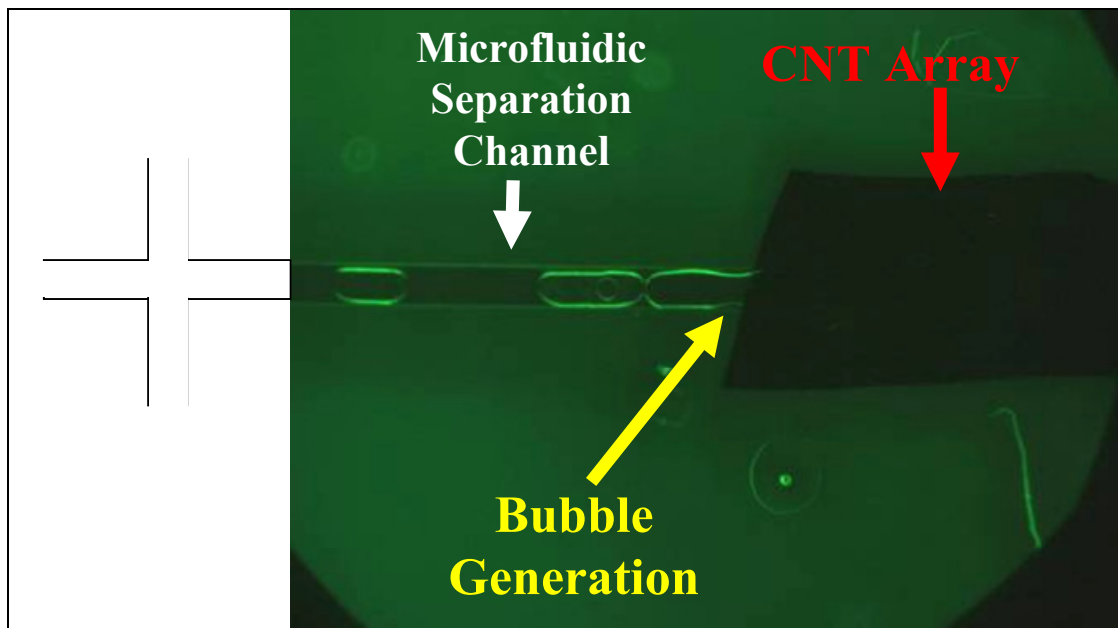
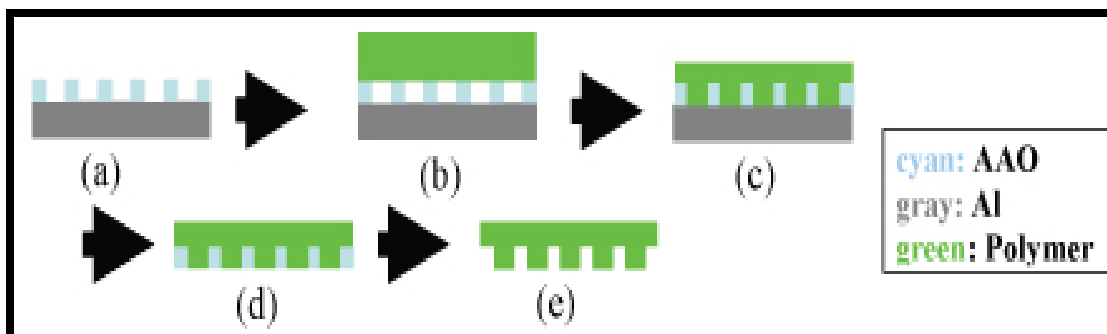


Figure 36: Bright-field microscope image of bubble generation at the edge of the CNT array in a complex photolithography DNA electrophoresis chip (the bubble generation is caused by the applied electric field). Courtesy of Dr. Jin Ho Kim at Brown University.

This bubble generation is caused by the electrolysis of water and is the result of the voltage drop across the CNT tunnel. This voltage drop originates from the electrical resistance difference between the buffer-filled channel and the CNT tunnel region. The highly conductive CNTs act as secondary electrodes for hydrogen gas generation from water. In order to resolve this issue, we made a line of non-conducting (polymeric) nanopost arrays.

2.3.2.7 Polymeric Nanopost Chips

The polymeric, non-conducting nanopost arrays have the same post diameter and spacing as the CNT arrays. The fabrication scheme and resulting arrays are shown below.



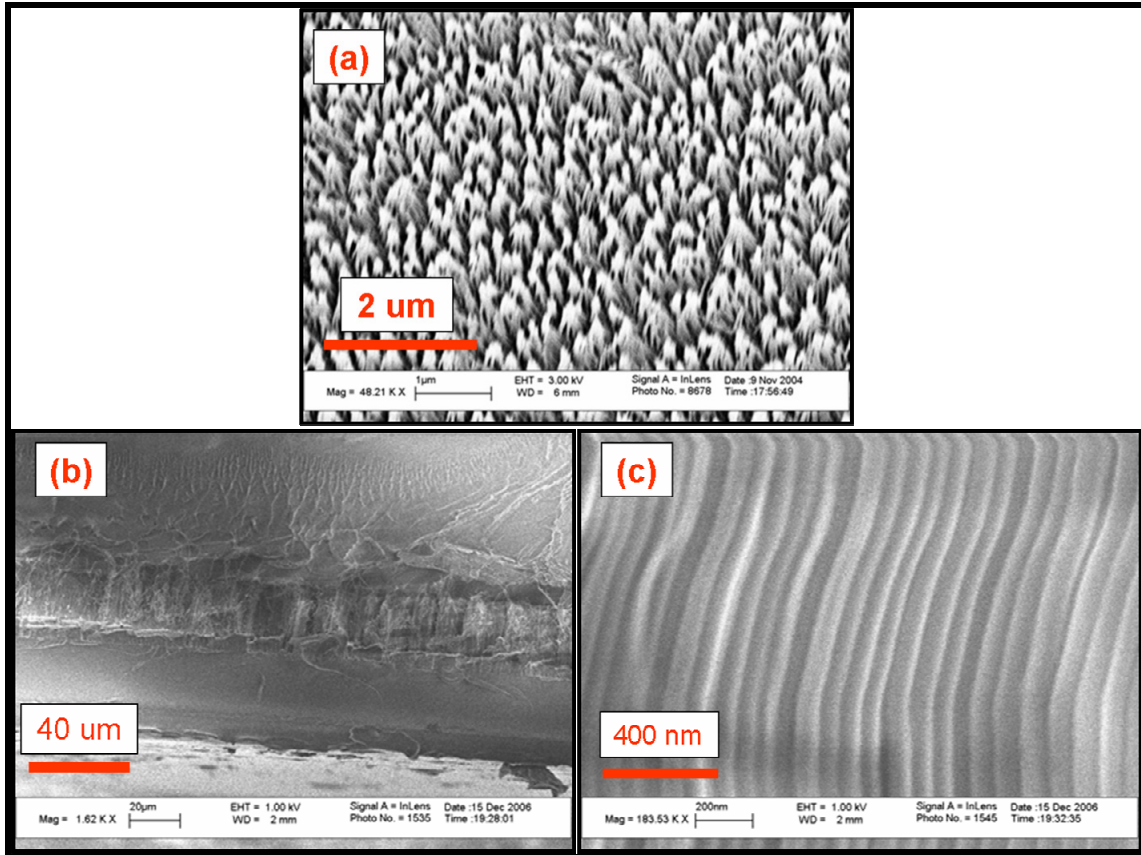
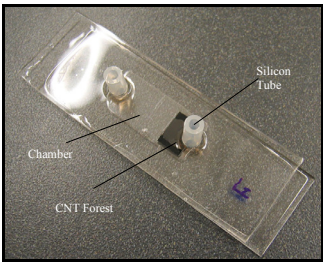


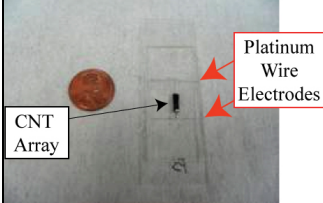
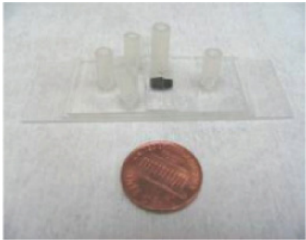
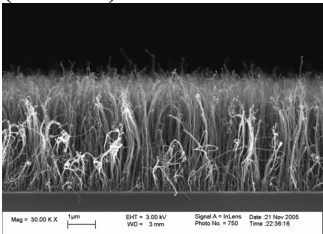
Figure 37: Top: Nanofabrication steps for making polymeric nanopost arrays. (a) Create the AAO membrane. (b) Place a sheet of polymer on top of the AAO. Apply mechanical pressure to the sample under a vacuum until the sample gets above the glass transition temperature of the polymer. (c) The AAO channels will fill with polymer. (d) Remove aluminum. (e) Remove the AAO via wet-etching. Bottom: Fabrication results from polymeric nanopost prototypes. (a) Polymeric polystyrene nanopost array. (b) A tunnel through an SU-8-supported polymeric nanopost array. (c) A higher magnification view of the SU-8-supported polymeric nanopost array.

The problems encountered in our polymeric nanopost chips include blocked fluid flow where the microchannel meets the nanopost array and severe nanopost bundling (due to polymer nanopost flexibility and hydrophobicity). We expect improved results with shorter stiffer polymer nanoposts and surface treatments (for making the nanopost surfaces hydrophilic). These steps should reduce bundling, bending and blockage.

2.3.2.8 Summary of Nanopost Array Platform Prototype Progression

The following table summarizes the efforts made in our prototypes as we encountered and overcame challenges. Overall, it seems, the least successful strategies were attempting to load/launch DNA without gated injection, attempting to close nanoscale roughness gaps with PDMS swelling, attempting to maintain uncompromised solidly anchored CNTs during long harsh channel-clearing RIE steps and viscous photoresist channel-flushing steps and attempting to eliminate the persistent bubbles of conductive nanoposts. The most successful strategies seem to be double-T gated injection, multi-step processing to avoid having to “cut out and insert” the nanopost array into a pre-made microfluidic chip, pre-treating PDMS with a corona treater to increase SU-8 spreading during spin-coating, controlling SU-8 stickiness “pre-baking” steps, and decreasing the length of polymeric nanoposts to avoid bundling and fluid blocking.

Recap of Previous Nanopost Prototypes		
Prototype Set	Problem(s) encountered	Solution(s)
1. Simple Chips 	<ul style="list-style-type: none"> The DNA fragments began to diffuse across the CNT array before we had a chance to apply the electrophoresis bias. 	<ul style="list-style-type: none"> We gathered DNA at a platinum wire “starting line”.
2. Starting Line Chips	<ul style="list-style-type: none"> The “launch” took too long (the DNA fragments were not launched simultaneously). 	<ul style="list-style-type: none"> We added a PDMS air chamber above the CNT array. We tried gated injection.

	 <p>CNT Array</p> <p>Platinum Wire Electrodes</p>		
<p>3. PDMS Air Chamber Chips</p>	<p>An air chamber was used to close the gap between the CNT tips and the PDMS ceiling and a gated injection scheme was used to create a narrow band of DNA that could be launched all at once.</p> 	<ul style="list-style-type: none"> • We could not “unstick” the PDMS ceiling from the CNT tips if too much pressure was applied while tuning the parameters (and the separation channel became completely blocked). • We ended up with side gaps because we were cutting our CNT samples by hand. 	<ul style="list-style-type: none"> • We tried different nanopost materials and different substrates.
<p>4. CNTs on Si, Si nanospikes, Au NP-coated CNTs, CNTs anchored in PDMS</p>	<p>We grew aligned CNTs on 3” Si wafers (a “new substrate” approach) using plasma enhanced chemical vapor deposition (PECVD).</p>  <p>Mag = 30.00 K X 1µm 0.0V = 3.00 kV Digital A: 100.0kV Date: 21-Nov-2006 Print No.: 120 Time: 22:36:12</p> <p>We fabricated the following alternate-material arrays: (a) Silicon nanospikes, (b) gold nanorod arrays, (c) gold nanoparticle-coated CNT arrays, (d) CNT arrays in PDMS and (e) polymeric nanopost arrays.</p>	<ul style="list-style-type: none"> • We found that integrating these alternate-material arrays into microfluidic chips was difficult. 	<ul style="list-style-type: none"> • We tried “direct patterning” of microfluidic channels in CNT arrays.
<p>5. Directly Patterned Chips</p>	<p>We fabricated microfluidic channels directly on CNT arrays.</p>	<ul style="list-style-type: none"> • We found that the integrity of CNT arrays became compromised and the microfluidic channels became blocked during the 	<ul style="list-style-type: none"> • We tried more complex photolithography.

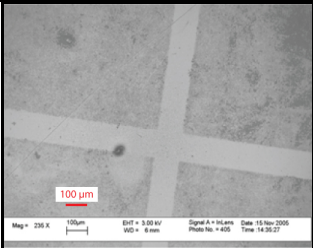
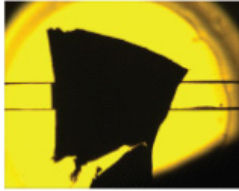
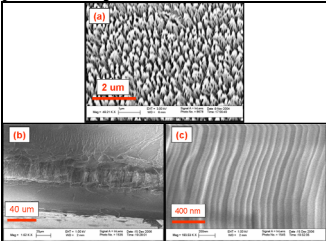
		photolithography process.	
6. Complex photolithography Chips	<p>We designed more complex photolithography procedures.</p> 	<ul style="list-style-type: none"> We found persistent bubble generation at the edge of the CNT arrays upon application of E-field. We had sealing problems. 	<ul style="list-style-type: none"> We pursued polymer nanoposts further. We worked on a new sealing method.
7. Polymeric Nanopost Chips	<p>We tried to eliminate bubble generation problems by switching to non-conductive polymer post arrays.</p> 	<ul style="list-style-type: none"> We found fluid flow blocked at the interface between the polymeric nanopost array and the microfluidic channel. We found that our polymer nanoposts bundled together (which often led to blocked arrays). 	<ul style="list-style-type: none"> We are now working on robust straight polymer nanoposts by reducing their length, using a hard polymer, and making the polymer surface hydrophilic.

Table 1: Recap of Nanopost Prototype Progression. Images in Rows 5-7 courtesy of Dr. Jin Ho Kim at Brown University. Image in Row 4 courtesy of Chih-Hsun Hsu at Brown University.

The goal of the DNA and protein separation project was to explore never-before-studied nanopore-DNA and nanotube-DNA interactions and exploit those interactions in a fast, sensitive, portable, multi-stage, contamination-free and low-cost device aimed at revolutionizing DNA and protein analysis. As we made progress, other groups made progress as well, developing 40 nm wide nanotrench [28, 29] and 5-20 μm inter-post gap [31] separation devices. Our device may not be the highest resolution biomolecule separation device in the field, but it is the first-ever device to take advantage of the properties of self-organized AAO and feature a vertically-oriented nanopore membrane.

The vertical orientation design gives this device platform the potential to perform compact multi-gate sorting in one separation channel and bring us closer to a device that can separate noninvasively collected body fluids into their individual components within minutes, allowing patients to have their genome and proteome analyzed on-the-spot.

2.4 Future DNA/Protein Separation Work

Future work for the Nanopore Array Platform includes improving the DNA separation reproducibility of our single-gate nanopore array devices, using the single-gate devices to separate proteins (AAO's physical and chemical properties can be easily modified for ion-exchange and affinity chromatography) and performing separations with multiple gates. Future work for the Nanopost Array Platform involves focusing on double-T pinched injection, multi-step processing to avoid manual integration of arrays, pre-treating PDMS with a corona treater to increase SU-8 spreading during spin-coating, controlling SU-8 stickiness with "pre-baking" steps and decreasing the length of polymeric nanoposts to avoid bundling and fluid blocking.

Chapter 3: Intracellular Probing and Drug Delivery

In this chapter, the interactions between free nanotubes and cells, tissues, and organ systems are explored with the intention of using those interactions to deliver drugs noninvasively to targets beyond the reach of conventional noninvasive delivery methods.

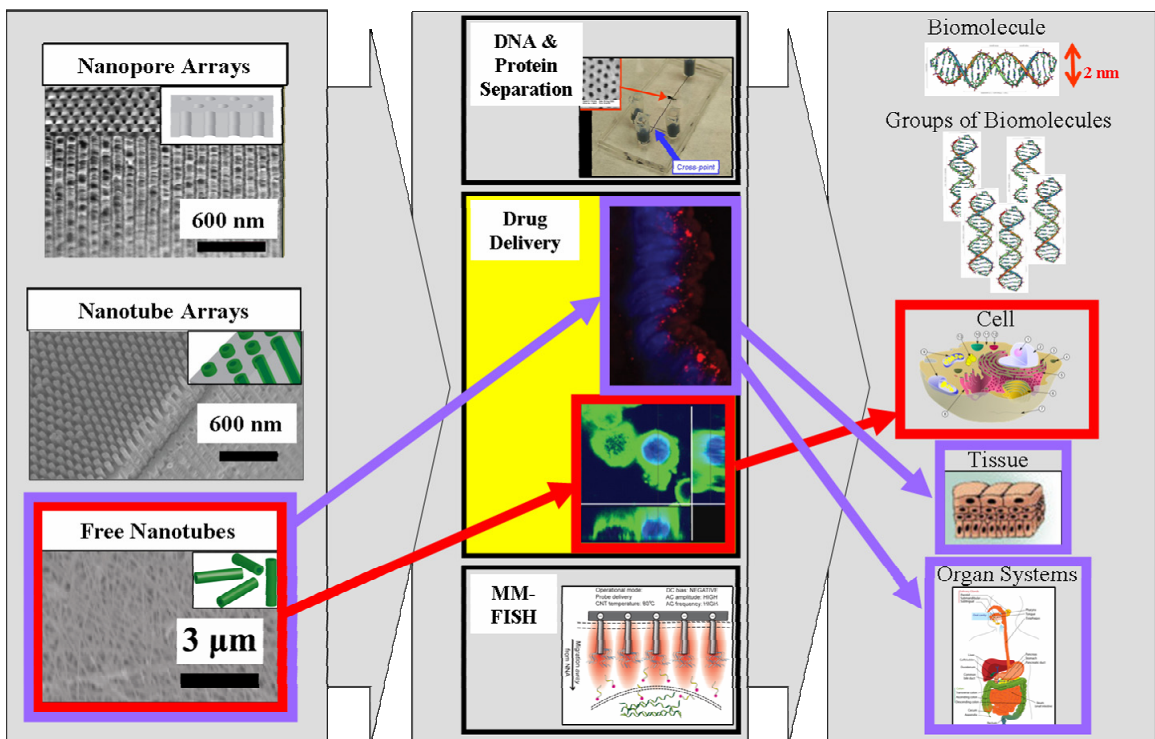


Figure 38: The drug delivery project focused on the interactions between free nanotubes (first column[1-3]) and the following three targets: individual cells, tissues and organ systems (third column[5-8]). Second column, first image: courtesy of Dr. Jin Ho Kim at Brown University. Second column, third image: from [4]. Second column, fourth image: courtesy of Dr. Gary Withey.

This project has two main branches: (1) interactions between mounted nanoneedles made from free nanotubes and individual cells (Section 3.3.1) and (2) interactions between free nanotubes dispersed in solution and cells, tissues, and organ systems (Section 3.3.2).

These project directions are highlighted in Figure 38: the “mounted” interactions branch is labeled in red and the “dispersed” interactions branch is highlighted in purple.

The goal for the “mounted” interactions branch is to gain unprecedented high-precision noninvasive access to individual live cells and exploit this access for novel trauma-free drug delivery methods for in vitro studies. The goal for the “dispersed” interactions branch is to develop nanotube-based noninvasive in vivo localized drug delivery methods for preventing the spread of infectious diseases (sexually transmitted diseases in particular) at mucosal membranes (where the infections start). The benefits of localized drug delivery include increased efficiency, reduced costs and fewer side effects.

There are many candidate materials for drug delivery [66]. Carbon nanotubes, in general, are very promising materials[67], as discussed in Section 1.3.1. They have many of the advantages that other materials have: they are easily functionalized and solubilized, have small diameters (as low as 2 nm) for easy penetration of blood vessels and cell membranes, and come with a fillable cavity for protected and timed release of drugs [66]. In addition to the aforementioned advantages, carbon nanotubes have extremely high aspect ratios (as high as 2000[4]), are chemically inert when capped, have a hydrophobic site (sidewalls) and hydrophilic site (tips), are mechanically strong (MWNT tensile strength ~ 63 GPa[19], $\sim 50X$ that of carbon steel), and are highly conductive (resistivity of SWNTs $\sim 10^{-4}$ $\Omega \cdot \text{cm}$ at 27 °C [19]). Template-grown CNTs have the added benefit that their diameter, length, and layering can be precisely engineered in massive quantities. The high aspect ratio, uniform diameter, and strength of carbon nanotubes is a unique and

powerful combination. There are other materials that have high aspect ratios (pulled glass pipettes [68]), high strength (stainless steel tensile strength ~ 1 GPa[69]), and low resistivity (resistivity of copper at 20 °C ~ 16 n Ω ·m[70]). There is no other material, however, that ranks as highly as carbon nanotubes do in all four categories. This unparalleled combination of properties gives our carbon nanotube nanoneedles an advantage over current state-of-the-art biomolecule delivery tools and techniques.

3.1 Toxicity Concerns

Carbon nanotube toxicity is a hot topic and will no doubt continue to be debated. At the moment, however, it seems that other than in extreme cases (direct injection of high concentrations of nanotubes, etc.), carbon nanotubes are cleared by the body in a timely fashion [71] [72] and do not pose a serious threat. There are some studies indicating that they may accumulate in the body due to their aspect ratio (they are similar in geometry to asbestos fibers)[73], but many studies indicate that their toxicity can be reduced by functionalizing them in certain ways[74, 75]. The exact uptake mechanism of carbon nanotube intake has been investigated [76] and it appears that the uptake mechanism is a form of endocytosis.

3.2 Prior Art

Nanotube-based drug delivery has been explored by many groups. Lacerda et al. have produced some excellent summaries of carbon nanotubes being used in medicine[67]. Nanotubes have been wrapped in ssDNA[74], loaded with plasmid DNA[77] and

protein[78], mounted on AFMs for confocally-imaged cell penetration[79], used to deliver siRNA in vitro[80] and in vivo[81], used to deliver an apoptosis-inducing chemical in vitro [82], and used to selectively destroy cancer cells [83].

Comparing our mounted carbon nanotube nanoneedles to other current state-of-the-art mounted needles, we see that while other groups have made great advances in the field [68, 79], truly noninvasive electrically-addressable three-dimensional access and delivery to sub-cellular compartments of individual live cells is still beyond the reach of current state-of-the-art tools, but may indeed be within the reach of our carbon nanotube nanoneedles. Comparing our dispersed biomolecule-loaded carbon nanotube conjugates to current solution-based orally-administered delivery systems, we see that while the field has made great strides [67], our nanotube conjugates have the potential to deliver payloads to in vivo targets that cannot be reached with the techniques that are available today.

3.3 Intracellular Probing and Delivery with Carbon Nanotubes

3.3.1 Mounted Nanoneedle Probe Delivery

We have developed a method for quickly and inexpensively manufacturing extremely high aspect ratio mounted nanotube bundle probes or “nanoneedles” at the tip of microelectrodes[84]. These nanoneedles have successfully delivered materials to individual cells. We have used them to load Alexa 1363 fluorescent dye onto a nanoneedle probe (via nonspecific adsorption) and deliver the dye to a human oral

epithelial cell [84]. The focus of this chapter, however, is the successful electrostatic loading and delivery of DAPI dye to an individual HeLa cell under a confocal microscope (see Figures 40 & 41).

3.3.1.1 Fabrication

As shown in Figure 39, our mounted nanoneedles are made by applying an electric field between two microelectrodes and placing a droplet of carbon nanotube solution (typically multi-walled carbon nanotubes in water or ethanol) between the microelectrode tips (Figure 39a). The droplet is then moved back and forth (Figure 39b) as the microelectrode tips are pulled farther and farther apart. The carbon nanotubes are aligned by the electric field and the strong hydrophobic-hydrophobic interactions between the carbon nanotube sidewalls make the nanotubes bundle together. The result is an extremely high aspect ratio tapered nanotube bundle at the tip of a microelectrode (right-hand image in Figure 39).

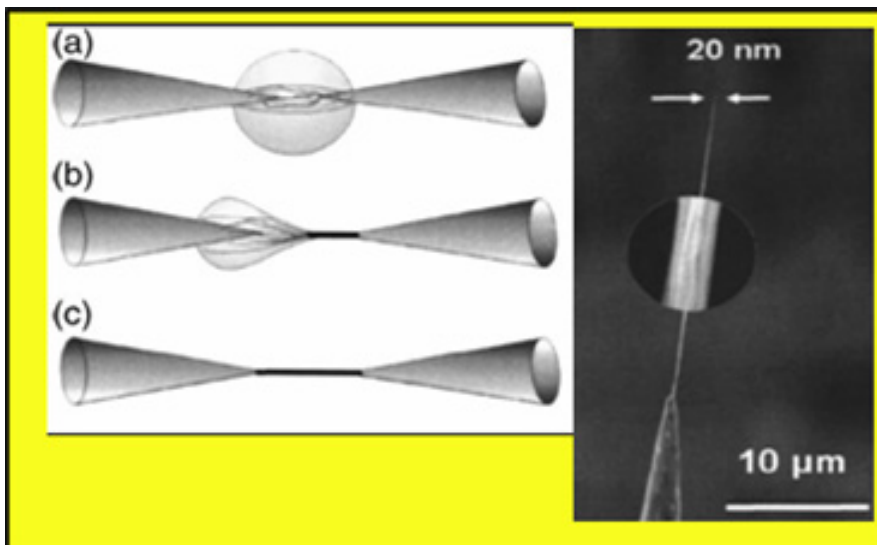


Figure 39: Left: Fabrication steps for mounted nanoneedle probes. Right: SEM image of a finished mounted nanoneedle probe[84].

3.3.1.2 Experimental Setup

To test the feasibility of such a delivery system, we first attempted to deliver a fluorescent dye to an individual cell in vitro under a confocal fluorescent microscope. The “payload” to be delivered in this case was the positively charged fluorescent dye commonly known as DAPI (4',6-diamidino-2-phenylindole, Invitrogen Molecular Probes, Carlsbad, CA). The experiments were performed on cultured HeLa cells which were pre-stained with a plasma membrane dye (Wheat Germ Agglutinin-AlexaFluor 488 conjugate, Invitrogen Molecular Probes, Carlsbad, CA).

The positively-charged DAPI dye was electrostatically loaded onto the nanoneedle tip; a negative bias was applied to the microelectrode base of the probe while the nanoneedle tip was submerged in an aqueous solution containing the DAPI dye molecules and viewed with a confocal microscope. Once the nanoneedle began to glow blue (the emission wavelength of DAPI is 461 nm[85]), it was lifted out of the DAPI solution and inserted into an individual HeLa cell (Figure 40). The DAPI payload was then electrostatically released into the cell by switching the applied bias from negative to positive. The targeted HeLa cell and a neighboring cell were then scanned with the confocal fluorescent microscope (see Figure 41). The three-dimensional information from the confocal scans confirms that we have indeed delivered our payload to the inside of the individual targeted cell (and not just its outer surface). The cell adjacent to the targeted cell was not affected and the targeted cell plasma membrane stayed intact during and after the nanoneedle insertion, supporting the notion that the hydrophobic sidewalls

and high aspect ratio of nanotubes are less invasive than conventional probes and more conducive to localized delivery.

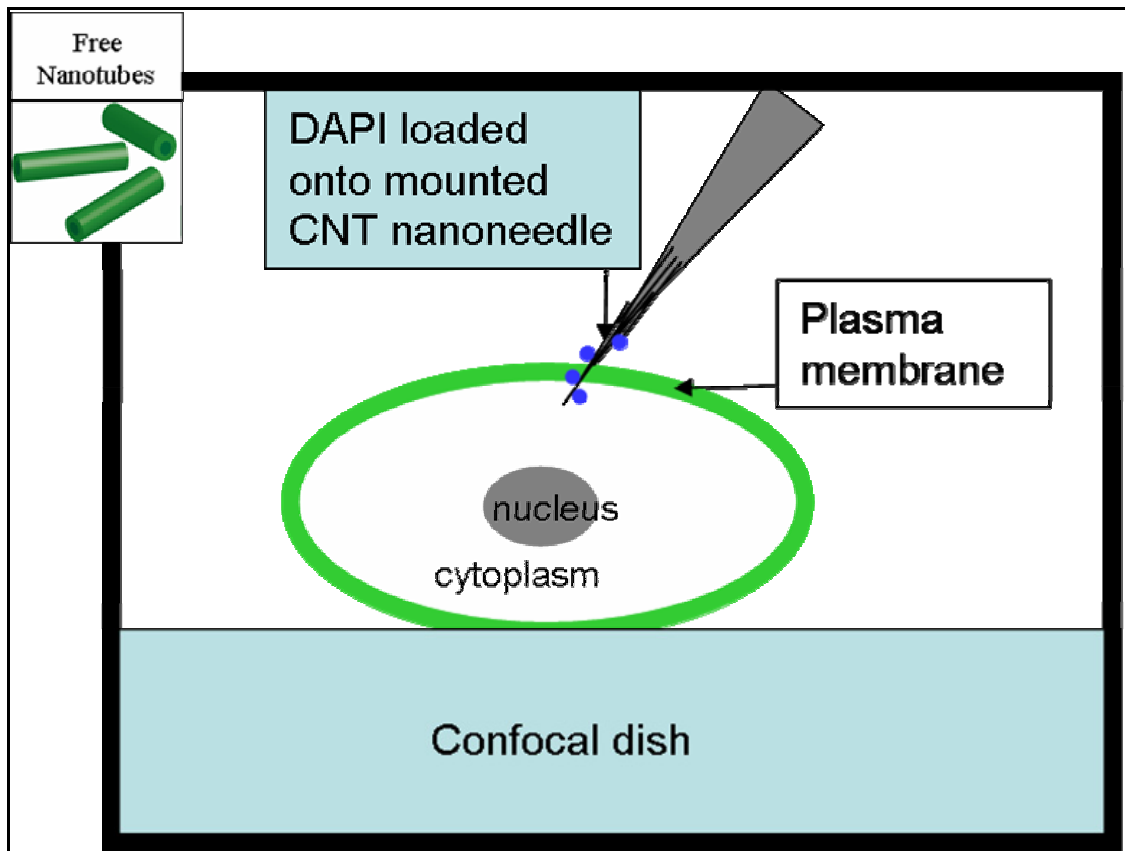


Figure 40: Experimental setup schematic for the mounted nanoneedle payload delivery confocal microscope experiment.

3.3.1.3 Results

Figure 41 shows the results of the mounted nanoneedle electrostatic payload delivery experiment. Plasma membranes are shown in green and the DAPI dye is shown in blue.

Cell #1 is the targeted cell and Cell #2 is the neighboring cell.

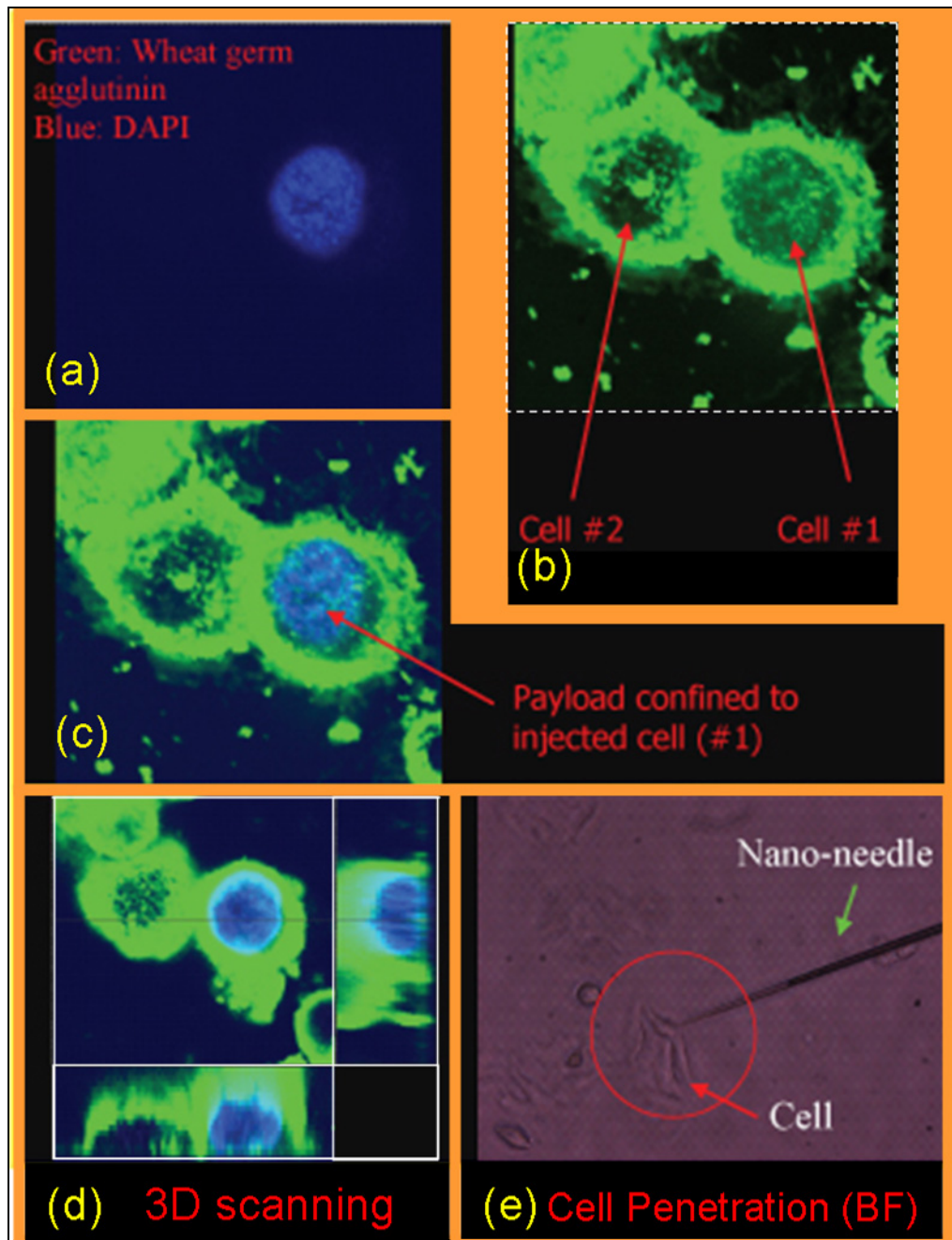


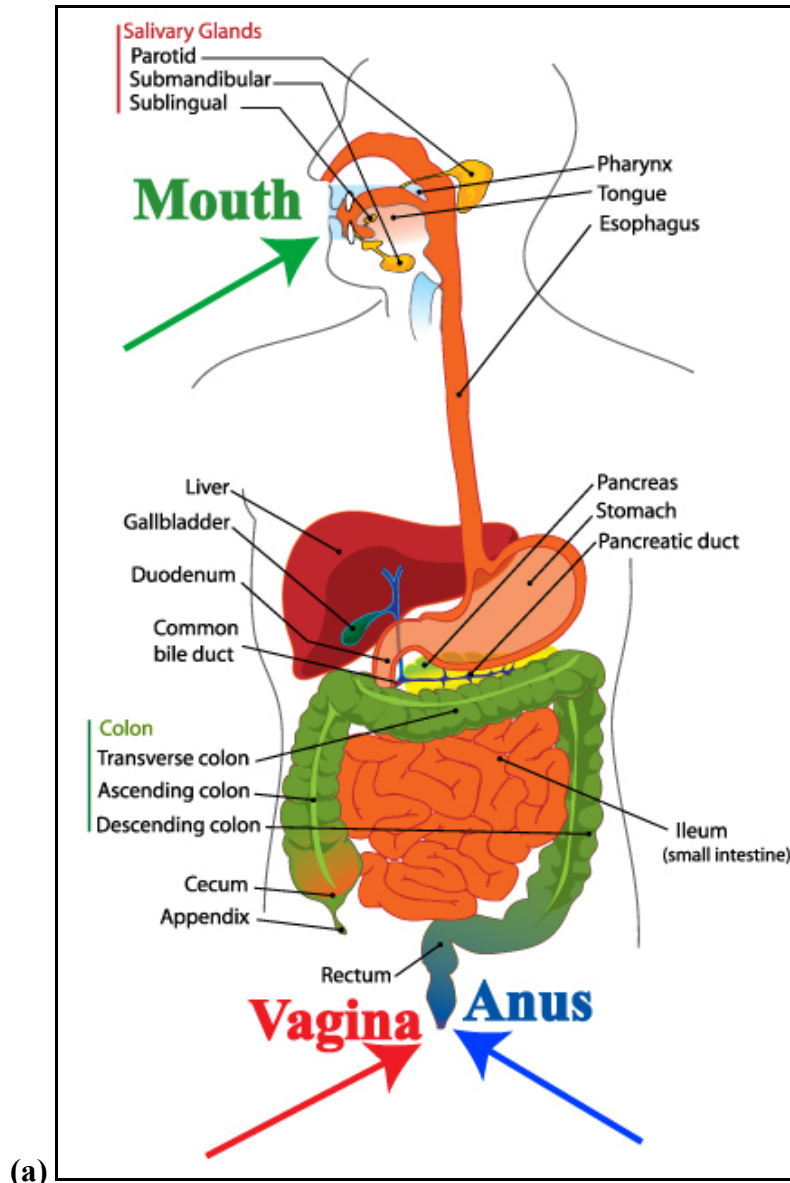
Figure 41: Confocal microscope image of electrostatic delivery of DAPI to an individual HeLa cell using a mounted carbon nanotube nanoneedle. (a) an image of the DAPI dye. (b) an image of the plasma membrane dye. (c) Image (a) overlaid with image (b). (d) Three-dimensional scanning of the targeted cell and its neighbor. Here, you can see the cross-sections (side view) of the cells. The blue DAPI payload is clearly confined within the plasma membrane of the targeted cell and is not present in the neighboring cell. (e) A Bright-Field image of the nanoneedle penetrating the target cell [4].

The experiment proved the nanotube nanoneedle concept for in vitro applications.

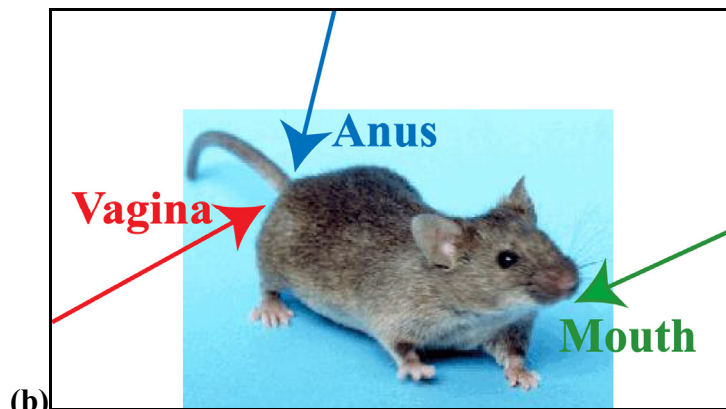
However, as tissue penetration is difficult for any probe with a diameter in the nanoscale range (and we eventually wanted to work on in vivo delivery), we soon shifted our drug delivery efforts to the “dispersed” interactions branch of the drug delivery project.

3.3.2 Free Nanotube Delivery

The “dispersed” interactions branch of our drug delivery efforts targeted mucosal membranes, where infectious diseases first enter the body. The primary mucosal membranes for sexually transmitted diseases (our main focus) are the mouth, the genitals, and the anus (see Figure 42). We explored interactions between dispersed nanotubes and the cells, tissues, and organ systems in mouse models (Figure 42 b), with the hopes of exploring interactions between dispersed nanotubes and human mucosal membranes in clinical trials in later stages of the project.



(a)



(b)

Figure 42: Mucosal membrane target areas for in vivo drug delivery in (a) human and (b) mouse model[8, 86].

We experimented with a variety of target tissues, conjugation methods and payloads, but this dissertation will focus on our most successful experiments which feature oral administration (the mucosal membranes in the mouth are the target), a conjugation scheme based on polyethylene glycol (PEG) and the fluorescent label AlexaFluor594 (to be described in greater detail in the next section) as the payload.

3.3.2.1 Conjugation

As shown in Figure 43, the conjugation method for this experiment is a multi-step process. The first step involved coating the hydrophobic sidewalls of single-walled nanotubes (SWNTs) with PEG-functionalized phospholipid surfactant. The phospholipid tails are hydrophobic and therefore interact with the sidewalls of the SWNTs. The PEG functional group is hydrophilic and helps to disperse the nanotubes in aqueous solutions (which is ideal for in vivo experiments where the sample is typically delivered in an aqueous PBS buffer base). The PEG functional group has an amine terminus.

The second step is to expose the PEG-coated SWNTs to an amine-reactive AlexaFluor 594 succinimidyl ester compound (Pyrano[3,2-g:5,6-g']diquinolin-13-ium, 6-[2-carboxy-4(or5)-[[2,5-dioxo-1-pyrrolidinyl]oxy]carbonyl]phenyl]-1,2,10,11-tetrahydro-1,2,2,10,10,11-hexamethyl-4,8-bis(sulfomethyl)-, inner salt, Invitrogen Molecular Probes, Carlsbad, CA). The amine group on the PEG reacts with the AlexaFluor compound, resulting in fluorescently labeled SWNTs.

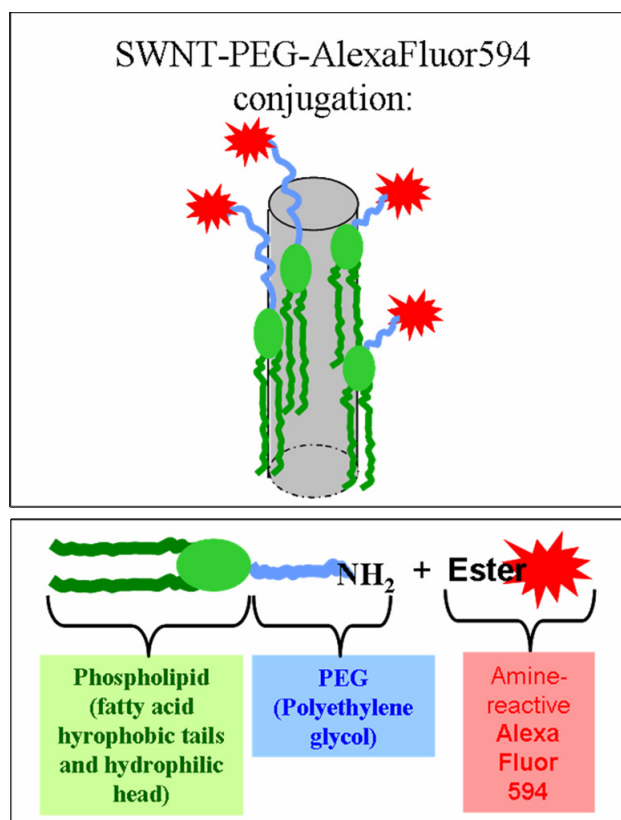


Figure 43: Conjugation scheme for our most successful “dispersed” nanotube interactions in vivo experiment. Single-walled carbon nanotubes (SWNTs) coated with a phospholipid-PEG surfactant and reacted with an amine-reactive fluorescent label.

3.3.2.2 Experimental Setup

The in vivo experiments were performed in collaboration with Dr. Bharat Rhamratnam and his colleagues at the Miriam Hospital in Providence, RI. The SWNT-PEG-AlexaFluor594 conjugates were suspended in a PBS buffer and orally administered to several mice. The incubation period was approximately 1 day. One control mouse was given PBS buffer and the other control mouse was given a PBS buffer solution with AlexaFluor 594 dye molecules in it (but no nanotubes). The results are shown in Figure 44-46.

3.3.2.3 Results

The results of the experiment are shown below. The results are promising, but not conclusive. We do see some differences between the control mice and the nanotube-administered mouse in these tissue sections (the nanotube-exposed mouse tissue seems to have more of a red pattern at the tissue wall, indicating possible uptake of the red-stained nanotubes at the epithelial wall of the lower bowel), but so far, we have not been able to repeat the result.

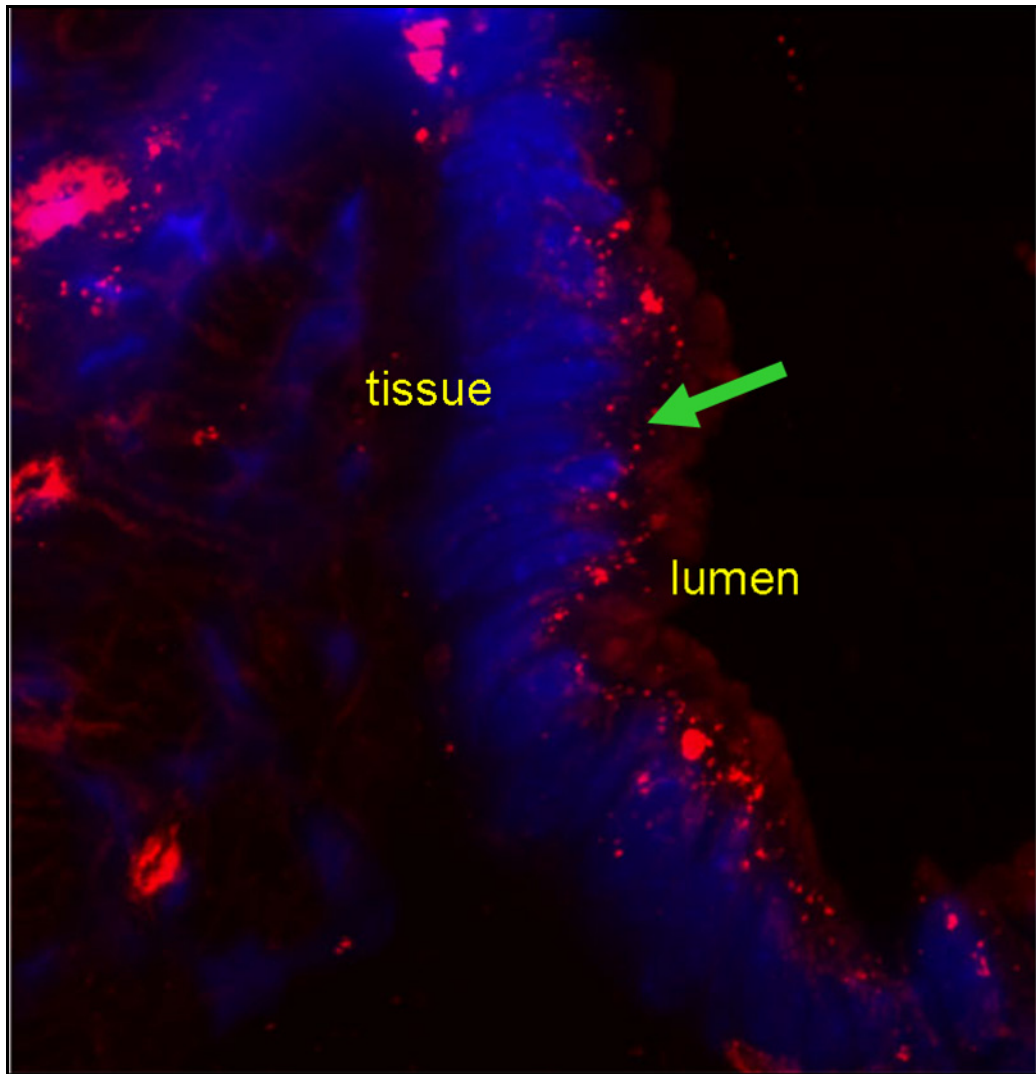


Figure 44: Orally administered SWNT-PEG-AlexaFluor 594 conjugates. Tissue sections were taken from the lower bowel after a 1-day incubation period. Nuclei in blue. SWNT conjugates

in red. The green arrow points to the epithelial cell layer of the mucosal membrane where we believe we are seeing nanotube uptake.

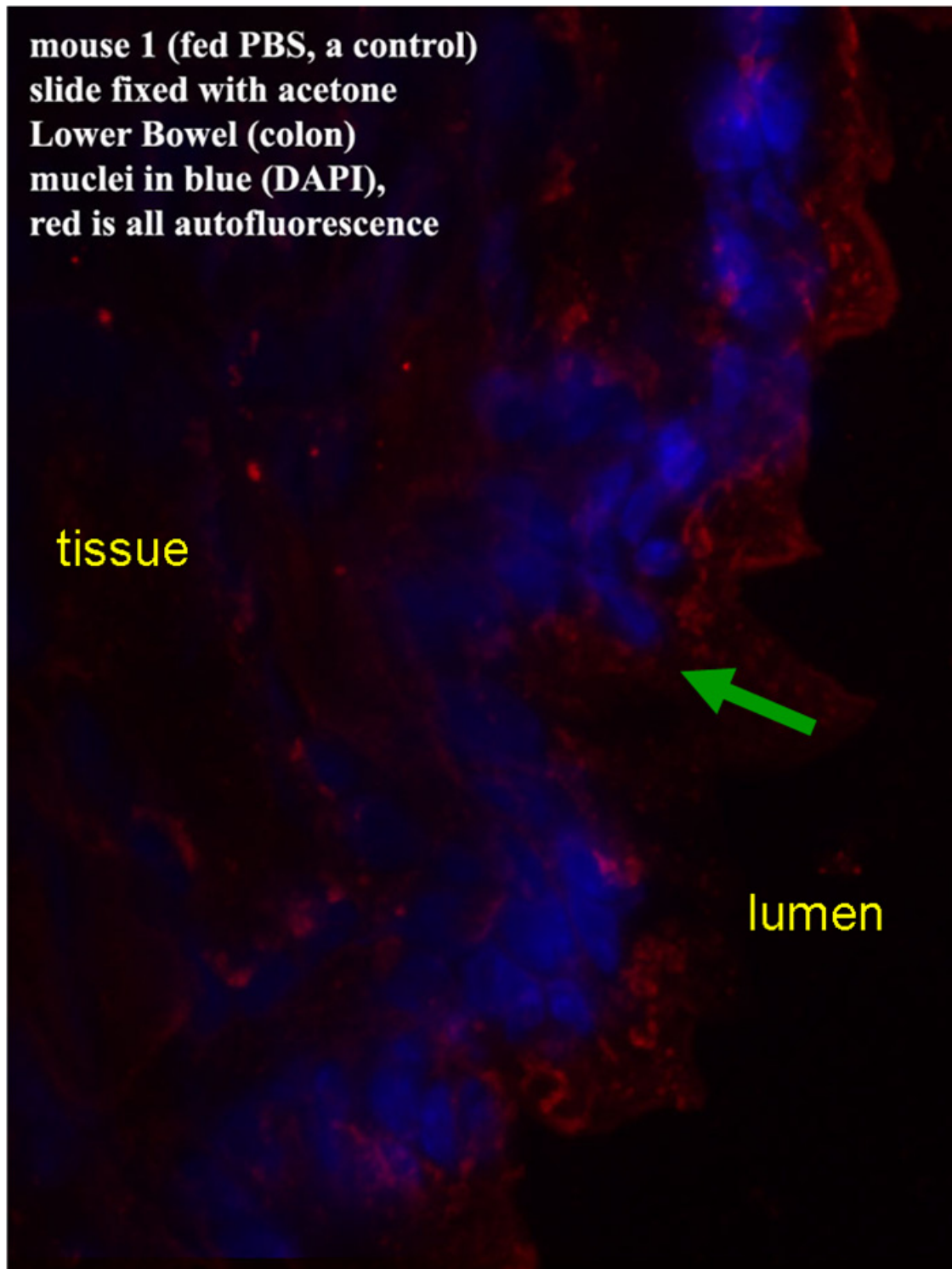


Figure 45: PBS control mouse tissue section. Lower Bowel. Cell nuclei in blue. Nanotube conjugates in red. The green arrow points to the epithelial cell layer of the mucosal membrane where we believe we are seeing nanotube uptake.

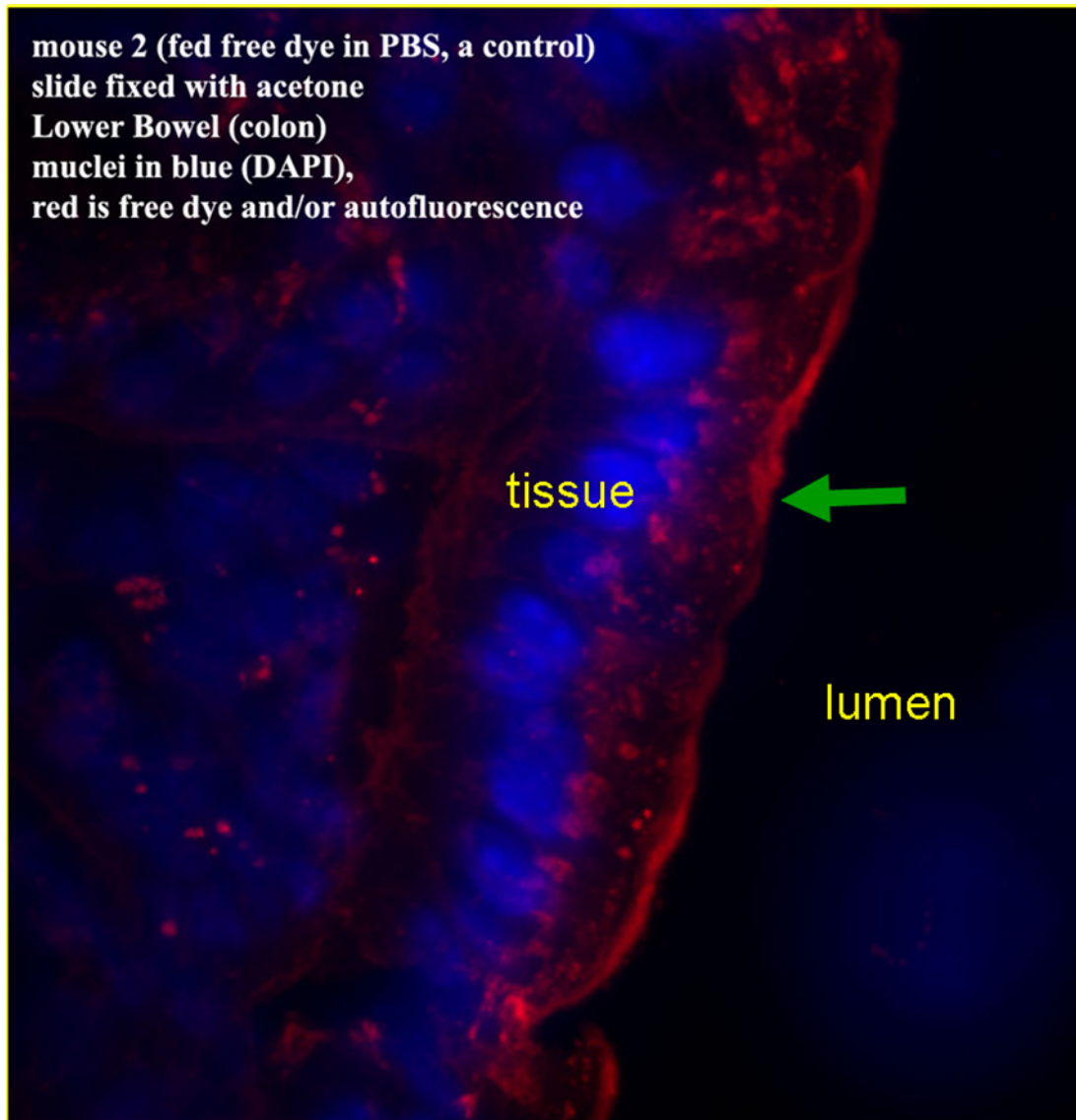


Figure 46: Free dye (just AlexaFluor 594 dye molecules, no nanotubes) in PBS (control) mouse tissue section. Cell nuclei in blue. Free dye in red. The green arrow points to the epithelial cell layer of the mucosal membrane where we believe we are seeing nanotube uptake.

3.4 Future Intracellular Work

Future work will include delivering STD-combating drugs to mucosal membranes via noninvasive pathways (pills, topical creams) as well as delving into biodegradable materials to be used as nanotubes and loaded (using our AAO templates). One potential layering strategy that could be applied is the approach of Zelikin et al[87].

Chapter 4: Massively-Multiplexed Fluorescence In Situ Hybridization (MM-FISH)

4.1 Introduction

The aim of the MM-FISH project is both to explore interactions between nanotube arrays and groups of cells (see Figure 47) and to utilize those interactions to massively multiplex a genetic analysis technique called Fluorescence In Situ Hybridization (FISH) (see Figure 48), resulting in fast clinical screening of genetic mutations in the chromosomes of individuals.

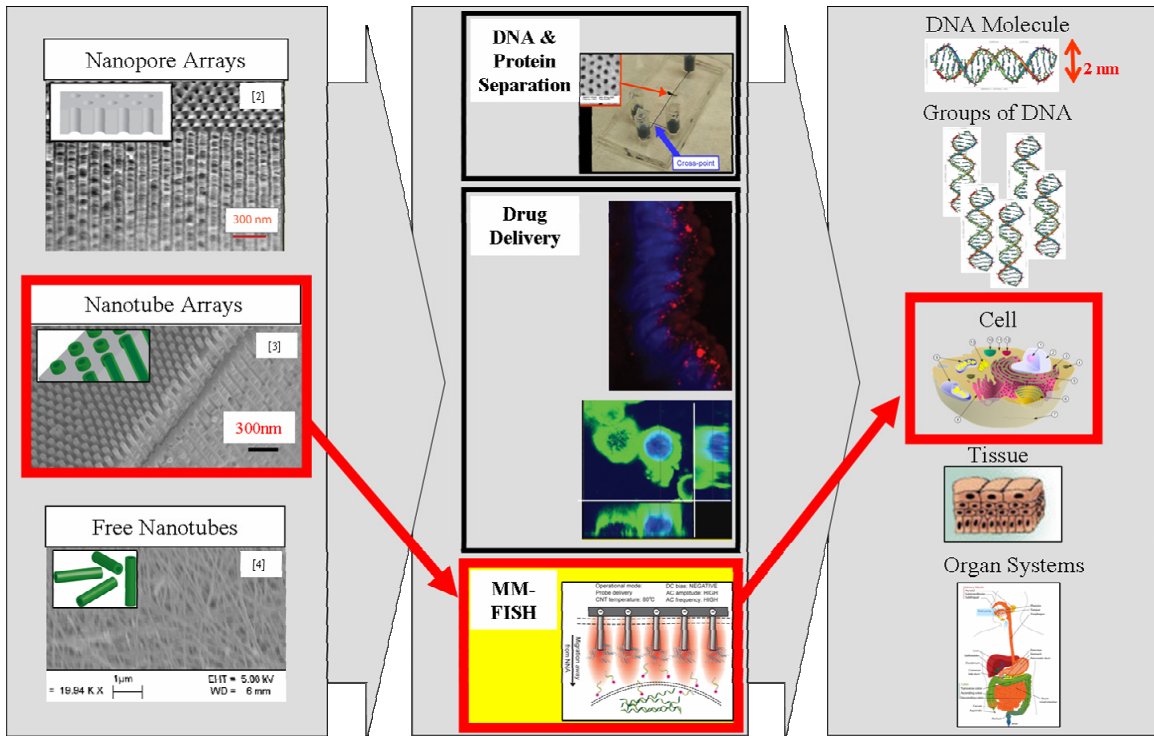
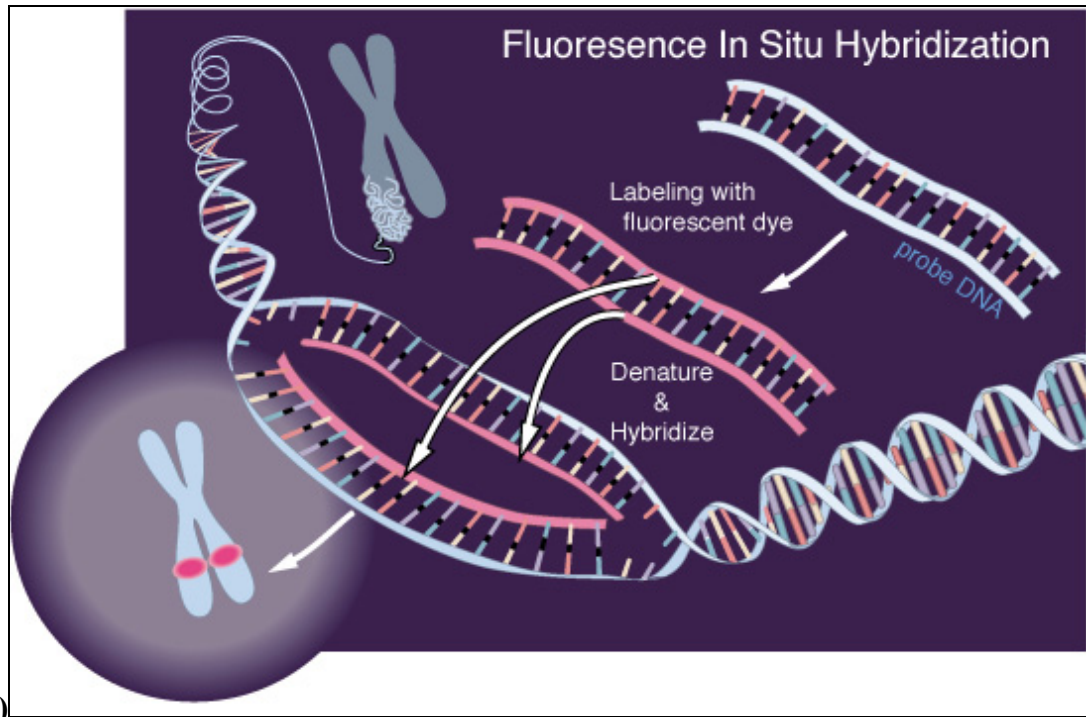
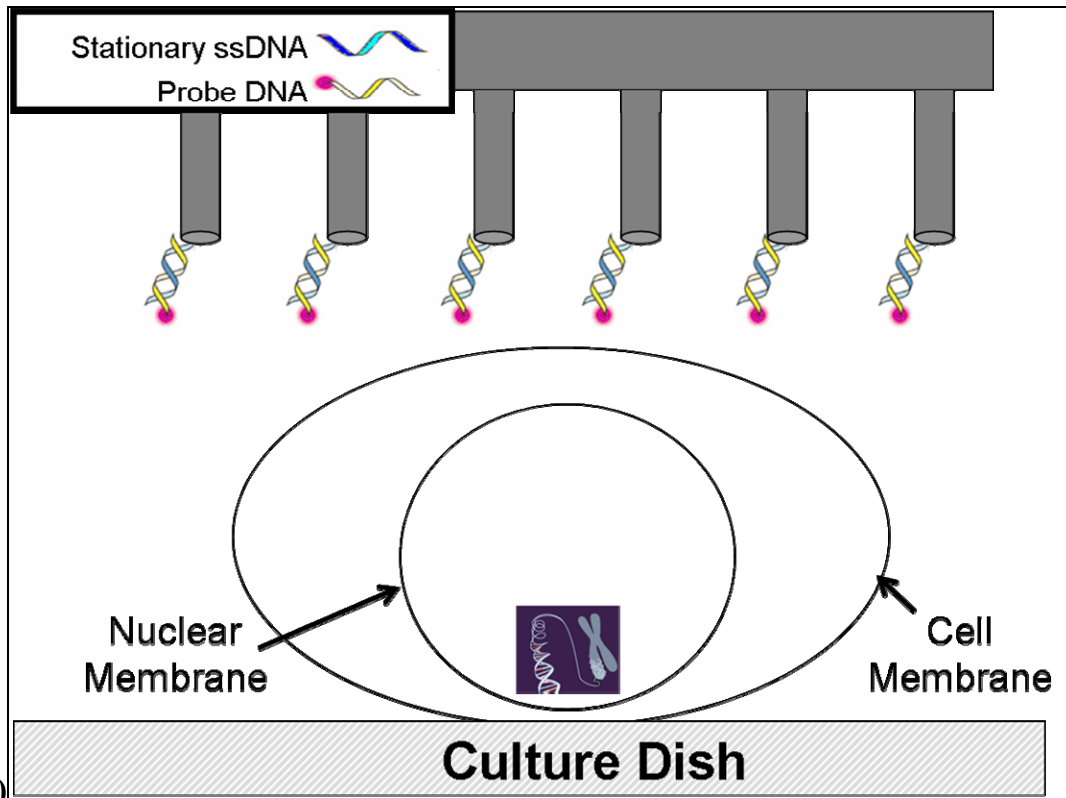


Figure 47: The Massively Multiplexed Fluorescence In Situ Hybridization (MM-FISH) project focused on the interactions between nanotube arrays (first column[1-3]) and groups of cells (third column[5-8]). Second column, first image: courtesy of Dr. Jin Ho Kim at Brown University. Second column, third image: from [4]. Second column, fourth image: courtesy of Dr. Gary Withey.



(a)



(b)

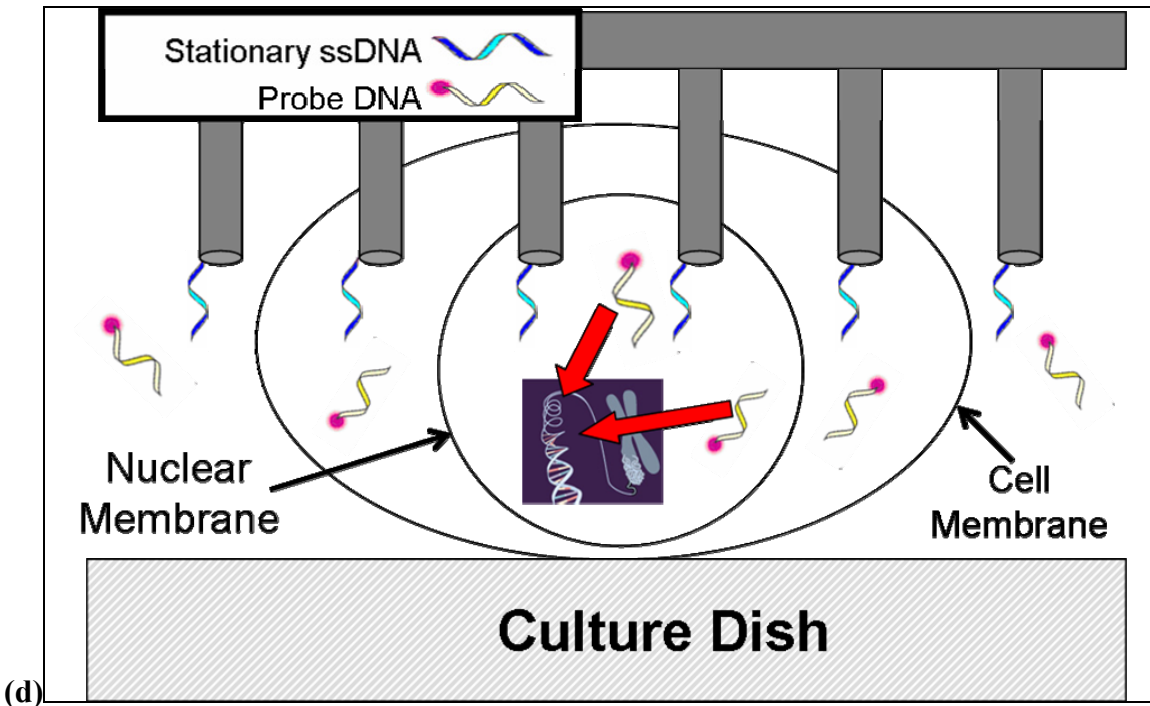
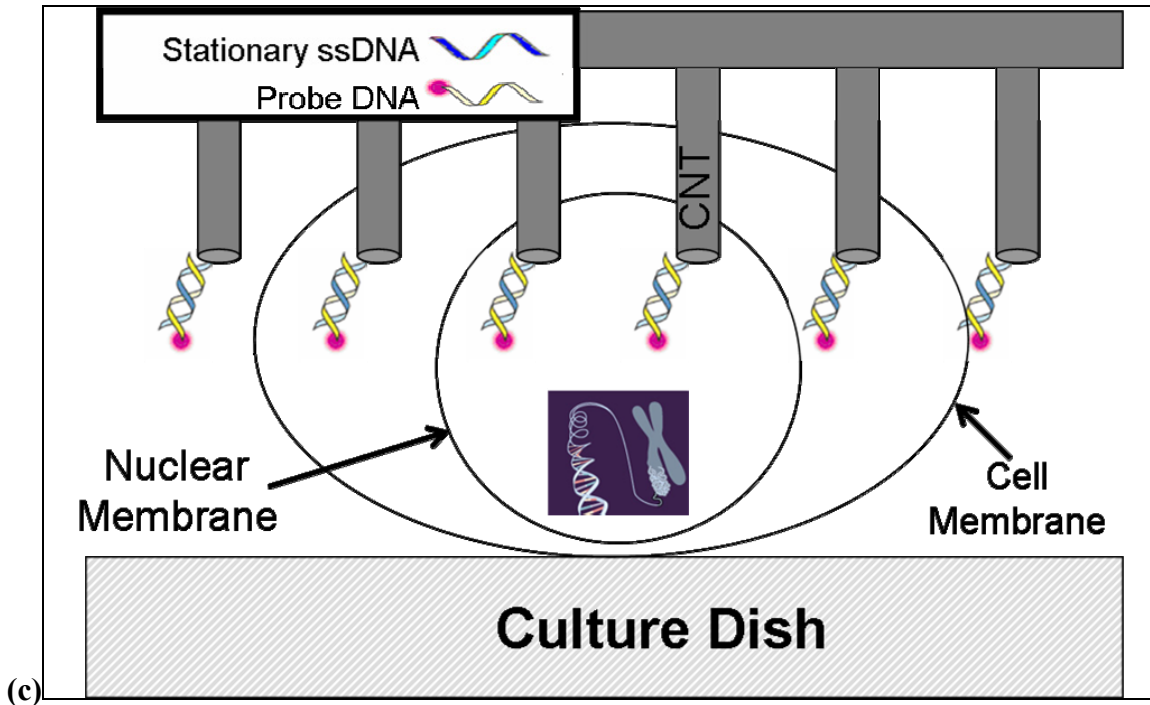


Figure 48: (a) How conventional Fluorescence In Situ Hybridization (FISH) works[88]. (b-d) A schematic of how MM-FISH would work. (b) “Stationary” ssDNA, which are compliments to the “probe DNA” are covalently bound to the carbon nanotube tips (conjugation protocol described in detail in [89]). The hybridization reaction between the stationary ssDNA and the “probe DNA” is used to “load” the CNT array with FISH probe. (c) The loaded CNT array is

then mechanically pressed into the cultured cell (or cells), piercing the cell membrane. (d) The probe DNA is then released from its stationary ssDNA anchor. Probe DNA inside the nuclear membrane is then allowed to hybridize with chromosomal DNA and sequence matches will fluoresce.

FISH is a method of locating a specific genetic sequence on chromosomal DNA. In brief, FISH involves sending fluorescently-labeled “probe DNA” sequences (the complement to a sequence of interest) to the vicinity of denatured chromosomal DNA and then checking to see where the “probe DNA” hybridized to the chromosomal DNA (see Figure 48a).

Confirming whether or not a genetic sequence of interest is present in someone’s chromosome is of great interest to the scientific community, especially when the genetic sequence is a disease-specific mutation and early detection can save lives or at least lessen the impact of the disorder. Identifying and tracking the movement of chromosomal aberrations is extremely important in cancer studies because chromosomal instability and rearrangement in genomic material is inherent in the disease process of cancer [90-92]. Many disease processes like cancer have roots in specific genes and spatial location of mutations is a very important part of the puzzle. FISH can help screen for cancer and many infectious diseases; it can also aid in elucidating the underlying disease processes and providing a starting point for the discovery of therapeutic agents. The rapid acceleration in the use of FISH [93] stands as testament to its recognized utility in the field of molecular cancer research.

The aim of this project is to revolutionize the FISH technique by making it massively multiplexed; multiplexing FISH will dramatically increase the throughput and speed of the FISH technique. Commercializing MM-FISH could result in inexpensive portable

chromosomal abnormality screening devices. In the time it takes to take a patient's vital signs, a doctor could find out whether or not their patient will have an adverse reaction to a treatment or medication and whether or not the offspring of a particular couple would be likely to inherit a genetic disorder.

Improvements in speed have been made for almost every step of the conventional FISH procedure through incremental refinements of the protocol. There has been an increase in denaturation speed via reagentless denaturing protocols and an increase in diffusion rates via permeabilization protocol refinement. Post-hybridization washing speed has increased with the development of new protocols and microwaves have been used to accelerate the hybridization process [94]. It is apparent from reviewing speed refinements that the fundamental limitation is the rate of diffusion of molecules into the cell and nucleus.

Conventional FISH is limited not only in terms of speed, but also in terms of the number of probes that can be tested at once. The key to solving this throughput problem is in the massively parallel nature of our system. Our nanotube arrays can contain on the order of one billion nanotubes per cm^2 – truly a massively multiplexed FISH system. In order to accelerate the processes of probe delivery and washing, this project aims to replace the diffusion-driven steps of conventional FISH with direct insertion and intracellular delivery of labeled probe DNA molecules, followed by local removal (washing) of unbound probes with the same nanotube array.

Rather than permeabilizing the cell membranes for diffusion of the probe DNA into the cell, we perform a direct, physical insertion of the probe using the nanotubes. Once inside the cell, the probe will be contained by the cell membrane, unable to diffuse to neighboring cells over the time course of the assay, hence turning a traditional FISH barrier (limited diffusion through the cell membrane) into an advantage.

4.2 Relevant Carbon Nanotube Array Properties

As discussed in Section 1.3.1, nanotube arrays grown in AAO templates have many properties that make them ideal for the MM-FISH project. Template-grown CNT arrays have a high aspect ratio[15], allowing them to penetrate cell membranes noninvasively with their small uniform diameters while still delivering an impressive amount of probe DNA payload via their length. The chemically inert hydrophobic sidewalls of these nanotube arrays makes them even less invasive as the nanotube sidewalls will not disrupt with the hydrophobic lipid bilayer in cell membranes. These arrays have a high degree of tunability and uniformity in their tube dimensions[10, 16] and periodicity [14], ideal for optimizing of cell membrane piercing frequency and diameter. The template method's large-area fabrication [10, 17], low manufacturing cost [10, 14, 15, 17] and semiconductor-compatibility [10] make it easy to imagine widespread clinical use and disposable MM-FISH chips for contamination-free results. The template's high pore density[14] allows for a high probe DNA loading capacity and high-throughput MM-FISH. The high strength [18] of CNT arrays means that repeated probe DNA injections can be performed. Carbon nanotubes' high thermal conductivity, high current density, and low resistivity [19] make them ideal for DC and AC field-assisted FISH probe

loading and releasing. The AAO-template nanotube fabrication method allows us to multiplex our tools: we can create hundreds of millions of identical physical tubes that can be functionalized with any number of biological molecules.

4.3 Construction of MM-FISH CNT Probe Delivery System

The array will be divided into subsections, each ultimately to be designated to carry a different DNA probe, or several different probes. Our initial design does not attempt to deliver multiple types of probe DNA to cells, but our future work will include multiple DNA probes being delivered to individual cells. The subsections will be electrically contacted by depositing a gold patterned circuit on the base of the array and making contact with each of the subpopulations of nanotube arrays. The approximate dimensions of our array will be 2cm x 2cm and will contain 192 rows and 192 columns of 100 μm gold lines evenly spaced with the ultimate independent addressability of $\sim 37,000$ individual subsections. Electric fields can then be used to direct the loading and binding of DNA and proteins to specific subsections. Subsections will be physically divided by microfluidic channels (trenches) in the nanotube array base (Figure 49).

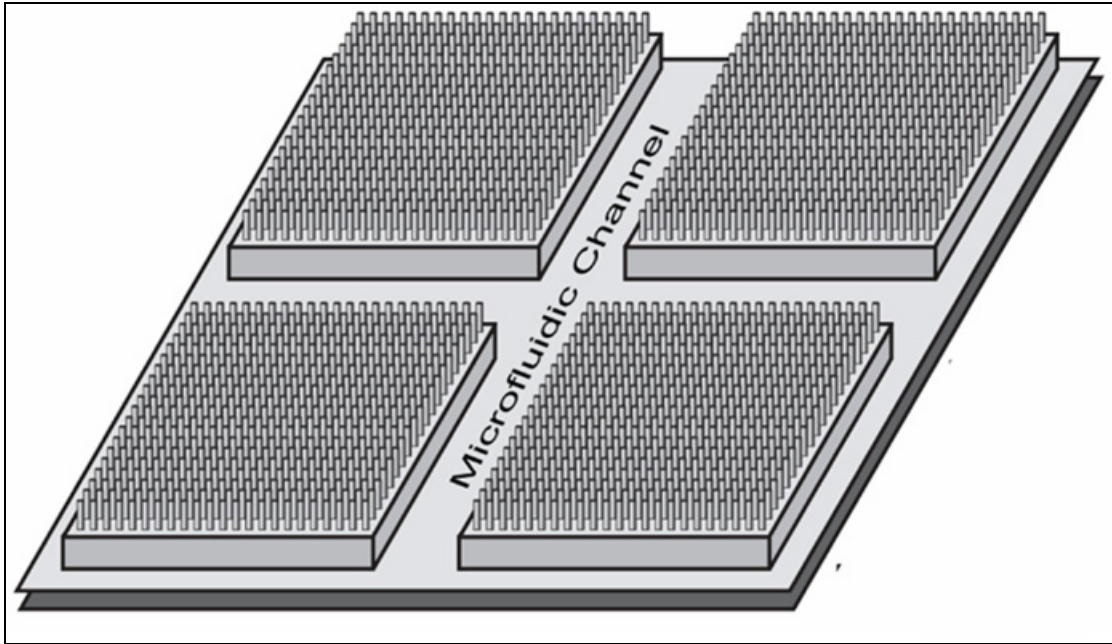


Figure 49: A schematic of a small area of our CNT array system. The area depicted would represent approximately a $200\mu\text{m} \times 200\mu\text{m}$ area of the array (CNTs not drawn to scale). Our subsection areas are $100\mu\text{m}$ by $100\mu\text{m}$. The CNT pillars will be modified with a DNA probe, then pressed down onto a cell culture to achieve probe injection. Diagram courtesy of Dr. Gary Withey.

These channels will be created by photolithography using simple masks and reactive ion etching (RIE). These channels will allow us to perform a continuous wash as needed during the probe delivery procedure to prevent probe spreading to neighboring subsections. The feature sizes of these trenches are relatively large ($10\mu\text{m}$ in width) by lithography standards and are therefore simple to incorporate.

4.4 MM-FISH Operation

The following section describes the role that our CNT array will play in our MM-FISH procedure.

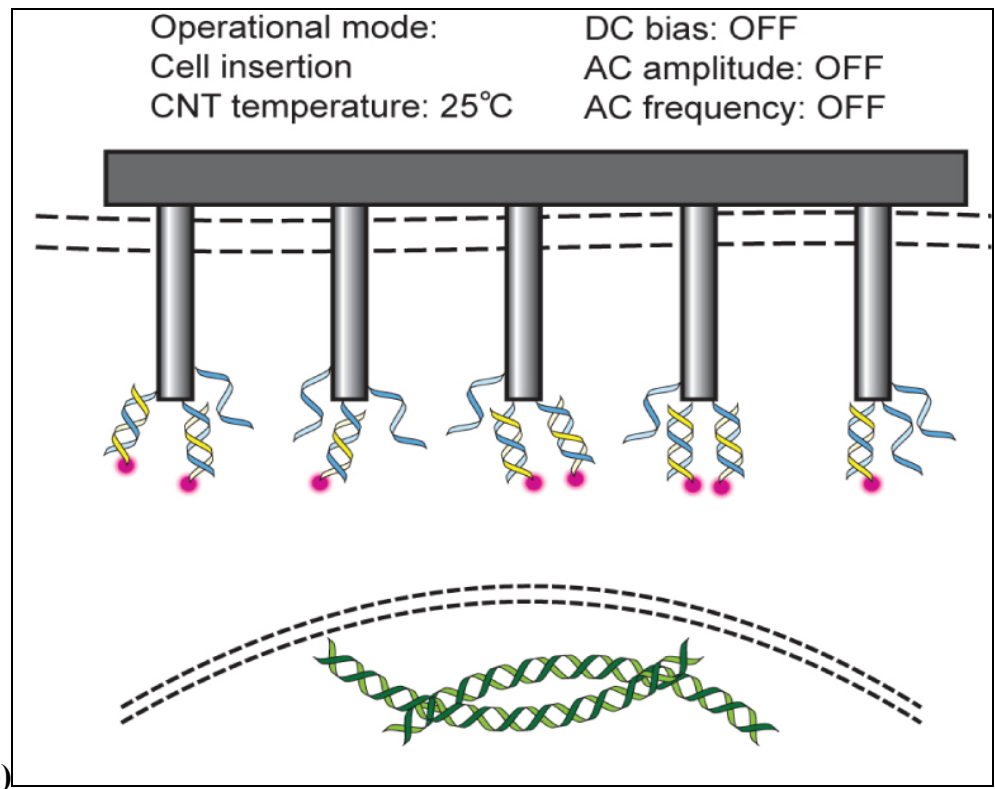
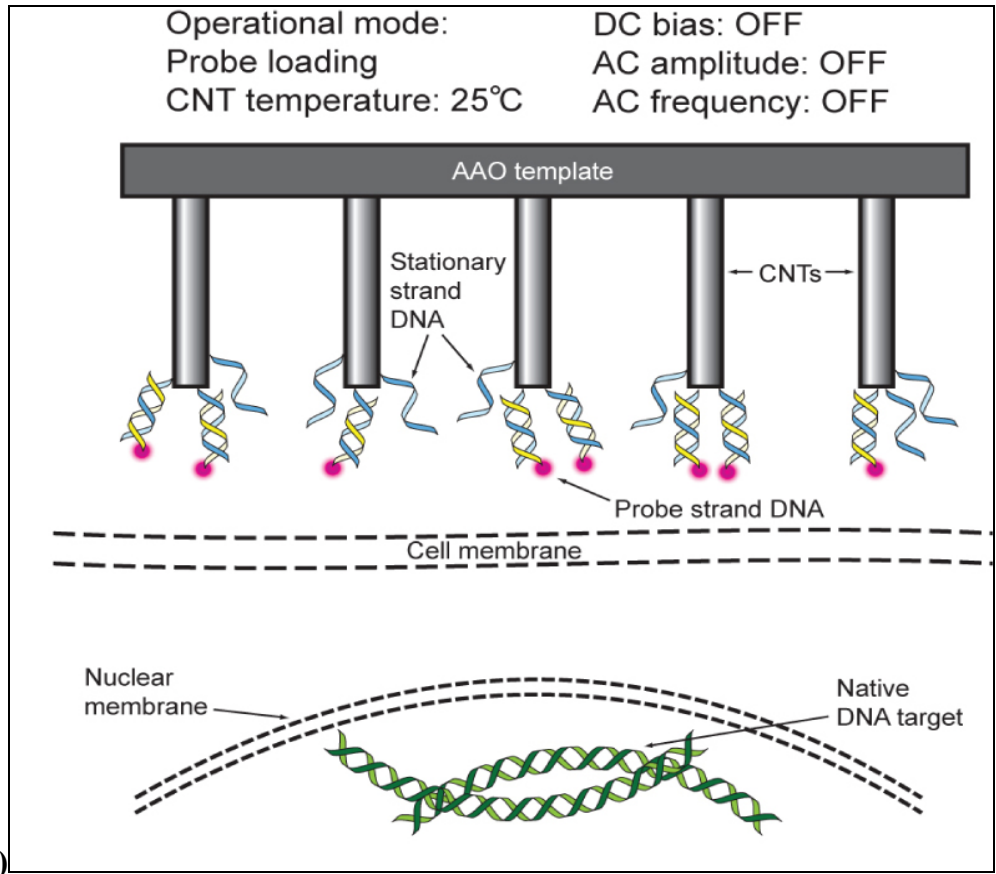
4.4.1 FISH Probe Delivery

In the conventional FISH procedure, probe delivery to the nuclear DNA target and subsequent washing of unbound probe are time consuming, rate-limiting steps.

Duration	Event
t_1	Diffusion through the cell membrane.
t_2	Diffusion through the nuclear membrane.
t_3	Diffusion through the nuclear environment and hybridization with its target.
t_4	Creation of negative probe concentration gradient across the nuclear membrane.
t_5	Diffusion of unbound probes across the nuclear membrane.

Table 2: Key Times in MM-FISH. Courtesy of Dr. Gary Withey.

Times, t_1 , t_2 and t_3 , correspond to the “hybridization” time in FISH protocols, while t_4 and t_5 correspond to the time it takes to perform the “post-hybridization wash”. We will replace diffusion as the transit mechanism (t_1 and t_2 events) with direct insertion. The amine-terminated stationary DNA oligos will be covalently linked to the CNTs by NHS/EDC carboxyl-amine coupling chemistry as described in [89].



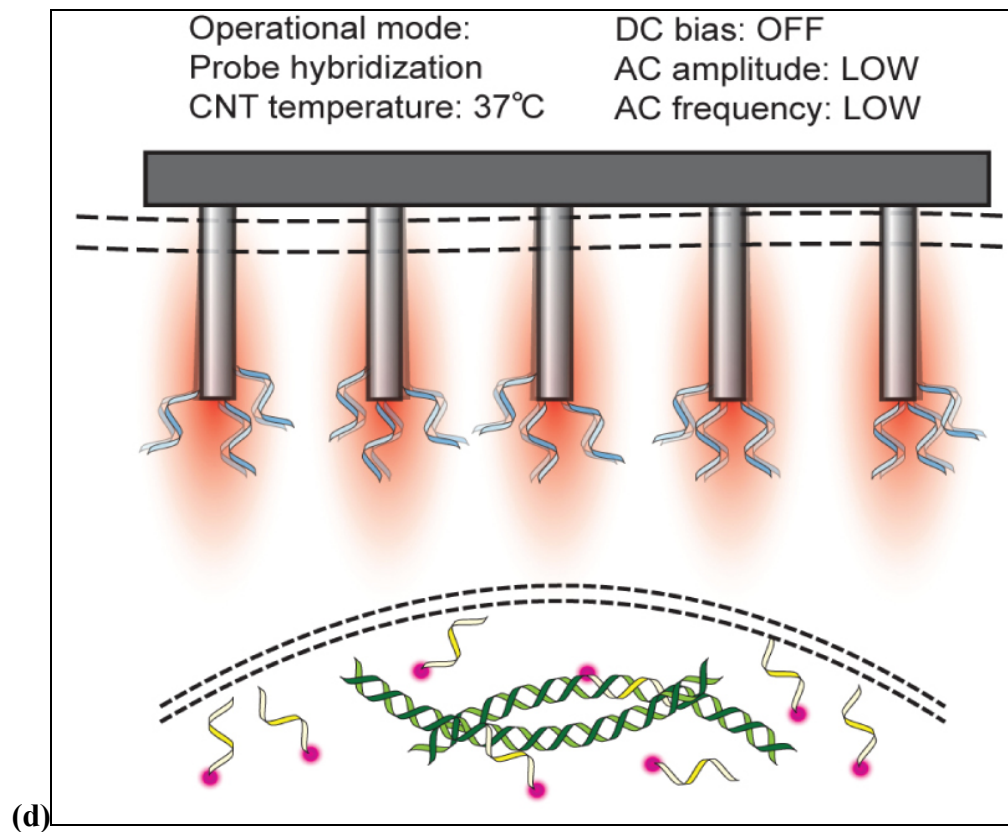
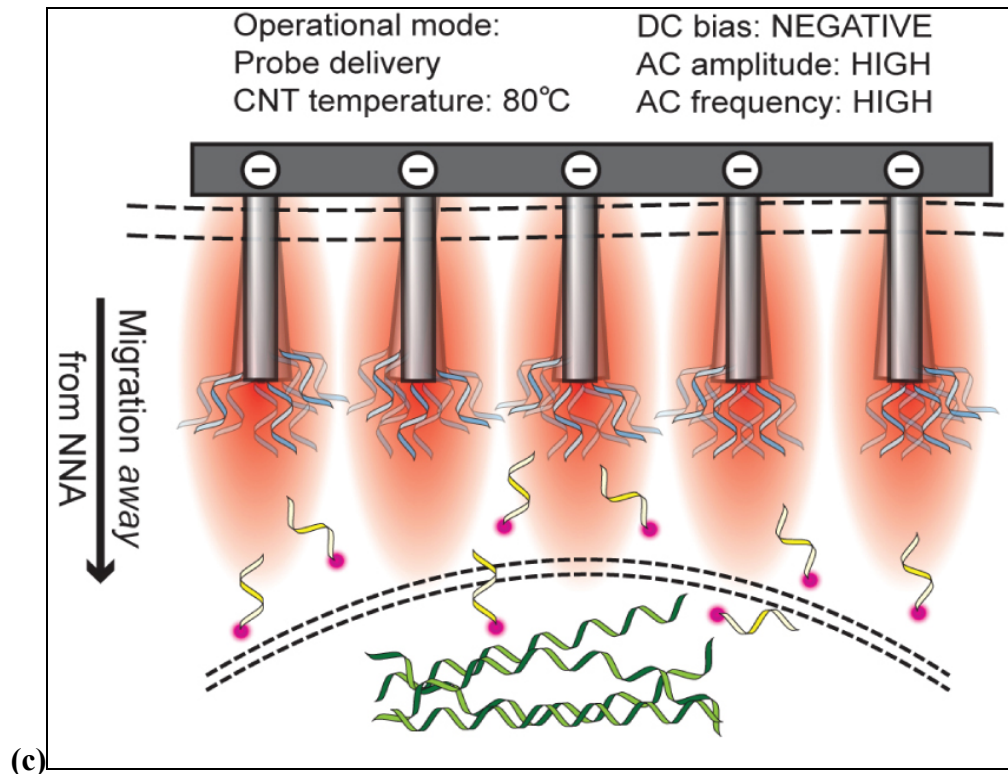


Figure 50: MM-FISH concept. Modes of nanotube array operation during the probe delivery and hybridization procedures. (a) Probe DNA is hybridized to stationary strand DNA that is

covalently linked to the CNTs. (b) The CNTs are then inserted through the cell membrane. (c) A DC-biased AC signal is then applied along with heat to melt the probe and native DNA, and drive probe DNA toward its nuclear target. (d) After probe DNA has arrived at its target, the temperature and induced CNT electromechanical vibration are reduced, and the DC bias is removed to allow the probe DNA to hybridize. Diagrams courtesy of Dr. Gary Withey.

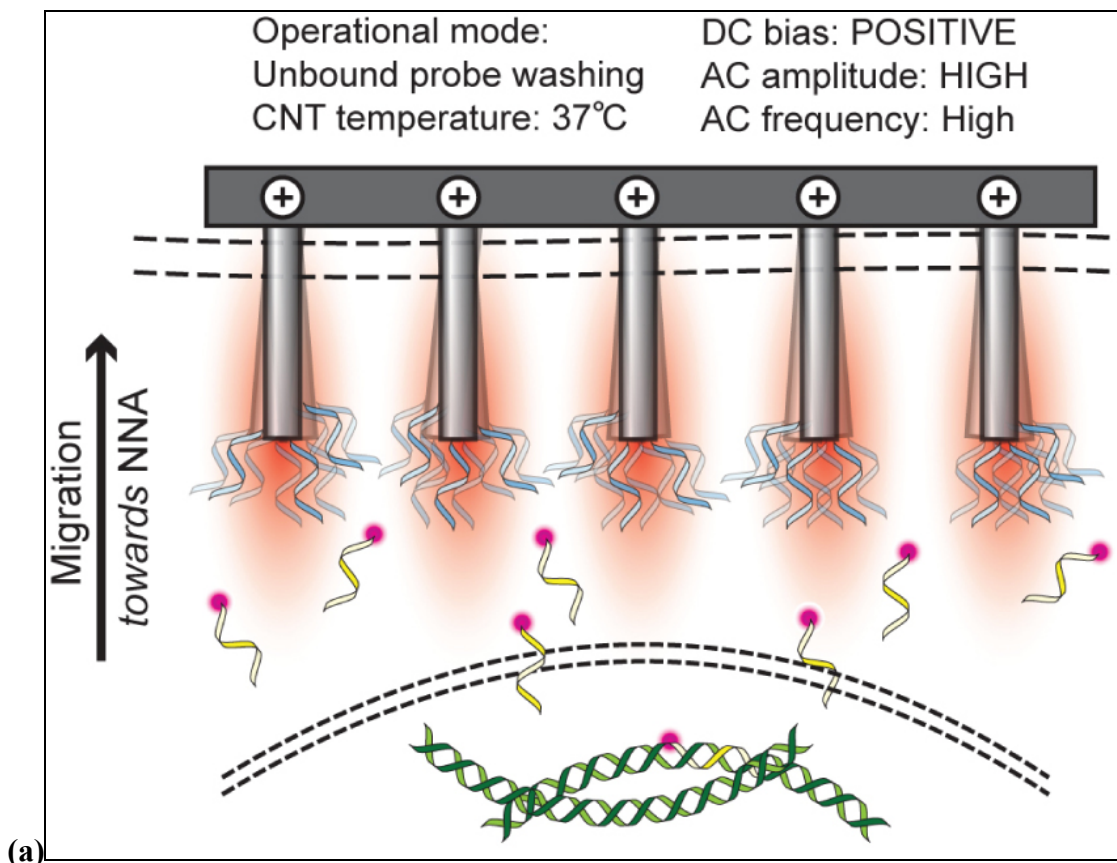
Modes 1 and 2 of Table 2 will be used to accelerate the delivery and hybridization of probe DNA with chromosomal DNA. The negative DC bias will repel the negatively charged probe DNA away from the CNTs and toward its nuclear target while the AC-induced electromechanical vibration of the CNTs will speed the diffusion process (Figure 50c). After the migration of probe DNA to its target, the temperature will be lowered to 37°C and the AC amplitude and frequency will be lowered to reduce the agitation of the nuclear environment and allow more rapid hybridization (Figure 50d). Unlike current FISH systems with dsDNA probes that can rehybridize to themselves after the melting phase (which ultimately reduces the sensitivity of the system) (31), we virtually eliminate the rehybridization problem by imposing a low negative bias on the CNT during the hybridization step. This has not only the effect of increasing sensitivity (i.e.: lowering the amount of probe material needed and the number of unbound probes) but also the speed of hybridization to the target (less competitive binding).

Mode	DC Bias	AC Amplitude	Result
1	Cathode (-)	High	DNA migration <i>away</i> from the CNT, enhanced melting due to agitation of nuclear media, enhanced target collision rate due to agitation of the media.
2	Cathode (-)	Low	DNA migration <i>away</i> from the CNT, accelerated hybridization with lower agitation.
3	Anode (+)	High	Excess DNA migration back <i>toward</i> the CNT, accelerated their recapture by CNT stationary probe.
4	Anode (+)	Low	DNA migration <i>toward</i> the CNT, enhanced rehybridization to the CNT ‘stationary’ probe due to electric field, and depleting (washing away) unbound probes.

Table 3: Modes of Operation for MM-FISH CNT Array. Courtesy of Dr. Gary Withey.

4.4.2 FISH Probe Spreading

Our FISH approach has an inherent advantage of *using* cellular membranes to help confine the diffusion of released probes to a small volume within the cell (also decreasing hybridization times). By taking this approach we avoid the problems of uncontrolled diffusion and lack of specific localization. Also, membrane permeabilization steps may be eliminated. As such, we convert the traditional *barrier* to fast FISH (cellular membranes) into an *advantage* (a system to reduce uncontrolled diffusion and promote spatial confinement).



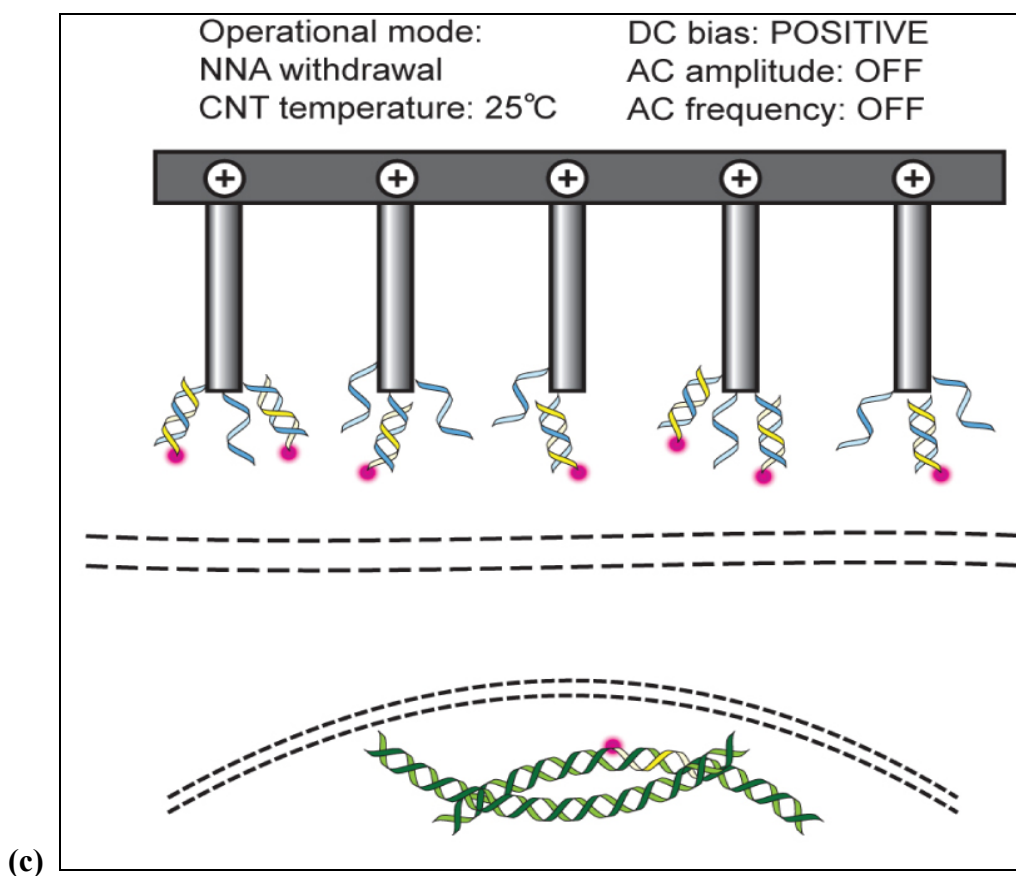
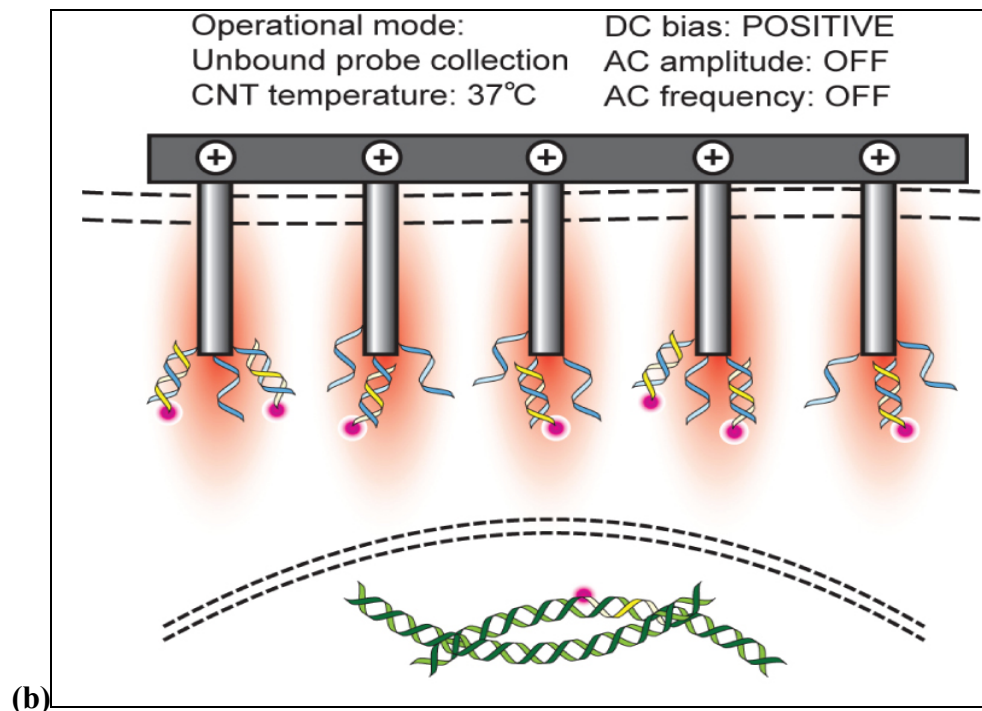


Figure 51: Modes of operation of the nanotube array during the solid state washing procedure.
 (a) A positive DC bias and high AC amplitude and frequency draw unbound probe back to the

CNTs while agitating the cellular environment to assist rapid diffusion. (b) When unbound probes have been drawn back to the array, the AC signal is turned off to allow probes to rehybridize to their complements linked to the CNTs. (c) The nanotube array is then withdrawn from the cell, removing excess probe. A positive bias is maintained to ensure that free probe will remain bound to the CNTs even in the event that they do not successfully rehybridize. Diagrams courtesy of Dr. Gary Withey.

4.4.3 Post-hybridization Solid-state “Wash”

Once the insertion and hybridization steps have been completed, we must remove the unbound DNA probes. Modes 3 and 4 of Table 3 will be employed during this “solid-state” washing phase of the procedure (t_4 and t_5 , Table 3). This step requires considerable additional time in current FISH systems but can once again be drastically reduced using our nanotube array system. The AC amplitude and frequency will be raised and a positive DC-bias will be applied to the nanotube array to agitate the cellular environment and draw unbound DNA probe back to their stationary complements on the CNTs (Figure 51a). The strength of the DC-bias will be optimized to attract unbound probe without stripping hybridized probe from its target, using SNR as an evaluation metric. The rate of “washing” can be enhanced not only by increasing the positive bias, but also through the attachment of excess stationary strands to the CNTs. As the unbound probe is collected at the CNTs, the AC amplitude and frequency will be lowered to facilitate hybridization to the stationary strands (Figure 51b). The nanotube array will then be retracted to withdraw the CNTs and unbound probe from the fixed cells (Figure 51c).

4.5 Preliminary Studies: Adapted FISH Protocol

The probe mix we used in our preliminary studies consists of a mix of aliphoid sequences

that simultaneously illuminate all human chromosome centromeres.

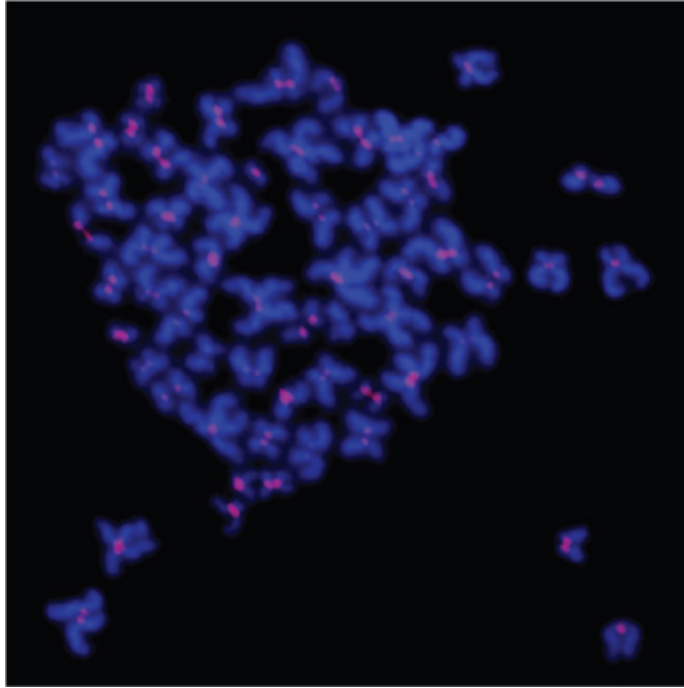


Figure 52: Fluorescence microscopy image of our adapted FISH protocol results. The centromeric region of each chromosome is clearly marked with a region of increased fluorescence from the selective hybridization of the fluorescently-labeled alpha satellite DNA sequence. This experiment confirms the viability of the underlying technology of the system we seek to develop.

The following is a basic protocol adapted from standard FISH procedure [95] that we have followed to perform conventional FISH:

4.5.1 Pre-hybridization

Slides will be incubated with 0.2N HCl for 30 minutes at 37°C, then rinsed twice in water (5 min each), followed by 2x saline sodium citrate (2x SSC; 2x 5 min each), and then 1M sodium thiocyanate or 10 mM citric acid buffer (pH 6.0) for 30 min at 80°C. Slides will be washed in 2x SSC (2x 5 min) followed by dH₂O. Slides will be treated with 0.005% pepsin in 0.01N HCl, pH 2.0 for 10 min at 37°C. Subsequently, the slides will be washed

in 2x SSC (2x 5 min) at 25°C, and then dehydrated through graded ethanol solutions (50% → 100%) and air-dried.

4.5.2 Denaturation and Hybridization

To perform the hybridizations, CNT-coupled fluorochrome (Cy5 or Cy3)-labeled DNA probes will be introduced by lowering the CNT array directly into the cultured cells.

DNA will be denatured by heating the CNTs optically or electrically from the base of the nanotube array, bringing the temperature to 75-80°C for 20 minutes in buffer containing 75% formamide, 50 mM Tris, 1 mM EDTA, and 100 mM NaCl. The application of DC-biased AC signal to the CNTs will assist the rapid delivery and hybridization of probe DNA to its target as previously described. The quantity of probe DNA linked to the nanotube array, the time schedule of the different modes, the strength of the DC offset, the magnitude of the AC amplitude and the AC frequency will all be incremented to determine optimal values. To exclude hybridization to mRNA, the cells will be pre-treated with DNase-free RNase A after the saponin permeabilization step. As negative controls, non-relevant probes will be used or the cells will be pre-treated with DNase I after the permeabilization step.

4.5.3 Post-hybridization Washes and Probe Detection

The solid state washing step will consist of the previously described schedule of applying a DC-biased AC signal to collect unbound DNA probe back at the CNTs. Again, we will increment the time schedule of the different modes, the strength of the DC offset, the

magnitude of the AC amplitude and the AC frequency to determine optimal values for these parameters.

4.6 Future MM-FISH Work

This platform, while still in its beginning stages, has the potential to exploit nanotube/cell membrane interactions to massively multiplex one of the most in-demand and powerful methods of studying chromosomal abnormalities in the field today. We will first focus on successfully delivering two probe sets, and then gradually increase the number of probe types and cell types we are working with until we can locate hundreds of abnormal chromosomal DNA sequences at once.

4.7 Conclusions

We have explored the interactions between engineered nanostructures and biomolecules through three projects and begun to exploit those interactions for the purposes of biomolecule separation, biomolecule delivery in vitro and in vivo, and a massively multiplexed biomolecule-nanotube hybridization system. Biomolecule separation is a crucial step in almost every form of genome and proteome analysis. Biomolecule delivery is needed to reach targets beyond current noninvasive methods. Massively multiplexed hybridization screening can give patients critical chromosomal defect information at a routine doctor's appointment.

While many groups have made impressive biomolecule separation devices[27-32], we are the first group to take advantage of AAO's properties and orient our nanopore membrane vertically, allowing for compact multi-gate sorting in one separation channel. As we made progress, other groups made progress as well, developing 40 nm wide nanotrench [28, 29] and 5-20 μm inter-post gap [31] separation devices. Our device may not be the highest resolution biomolecule separation device in the field, but it is the first-ever device of its type and brings us closer to a device that can separate noninvasively collected body fluids into their individual components within minutes, allowing patients to have their genome and proteome analyzed on-the-spot.

The drug delivery project has two main branches: (1) interactions between mounted nanoneedles made from free nanotubes and individual cells and (2) interactions between free nanotubes dispersed in solution and cells, tissues and organ systems. The goal for the "mounted" interactions branch was to gain unprecedented high-precision noninvasive access to individual live cells and exploit this access for novel trauma-free drug delivery methods for in vitro studies. The goal for the "dispersed" interactions branch was to develop nanotube-based noninvasive in vivo localized drug delivery methods for preventing the spread of infectious diseases (sexually transmitted diseases in particular) at mucosal membranes (where the infections start).

Comparing our mounted carbon nanotube nanoneedles to other current state-of-the-art mounted needles, we see that while other groups have made great advances in the field [68, 79], truly noninvasive electrically-addressable three-dimensional access and delivery

to sub-cellular compartments of individual live cells is still beyond the reach of current state-of-the-art tools, but may indeed be within the reach of our carbon nanotube nanoneedles. We have successfully delivered a payload to an individual cell; future work will explore delivering payloads to individual organelles.

Comparing our dispersed biomolecule-loaded carbon nanotube conjugates to current solution-based orally-administered delivery systems, we see that while the field has made great strides [67], our nanotubes conjugates have the potential to deliver payloads to in vivo targets that cannot be reached with the techniques that are available today. Our in vivo results for our orally administered SWNT-PEG-AlexaFluor 594 conjugates are promising, but not conclusive; future work will focus on biodegradable nanotube delivery systems.

The aim of the MM-FISH project was to revolutionize the FISH technique by massively multiplexing the process. This platform, while still in its beginning stages, has the potential to exploit nanotube-cell membrane interactions to massively multiplex one of the most in-demand and powerful methods of identifying chromosomal abnormalities in the field today. We will first focus on successfully delivering two probe DNA sets, and then gradually increase the number of probe types and cell types we are working with until we can locate hundreds of abnormal chromosomal DNA sequences at once.

References

1. Li, J., et al., *Highly-ordered carbon nanotube arrays for electronics applications*. Applied Physics Letters, 1999. **75**(3): p. 367-369.
2. Tzolov, M., et al., *Electronic transport in a controllably grown carbon nanotube-silicon heterojunction array*. Physical Review Letters, 2004. **92**(7): p. 075505.
3. Hartman, A.Z., et al., *Theoretical and experimental studies of carbon nanotube electromechanical coupling*. Physical Review Letters, 2004. **92**.
4. Jouzi, M., *Carbon Nanotube Nanoneedles and Their Electrical-Mechanical-Chemical Interactions with Biological Systems*, in *Department of Physics*. 2008, Brown University: Providence. p. 84-87.
5. *DNA*. Wikipedia, The Free Encyclopedia 14 Sep 2008, 21:40 UTC [cited 17 Sep 2008]; Available from: <http://en.wikipedia.org/w/index.php?title=DNA&oldid=238444758>.
6. *Cell (biology)*. Wikipedia, The Free Encyclopedia 18 Sep 2008, 04:57 UTC [cited 18 Sep 2008]; Available from: [http://en.wikipedia.org/w/index.php?title=Cell_\(biology\)&oldid=239195270](http://en.wikipedia.org/w/index.php?title=Cell_(biology)&oldid=239195270).
7. *Epithelium*. Wikipedia, The Free Encyclopedia 16 Sep 2008, 00:12 UTC [cited 18 Sept. 08]; Available from: <http://en.wikipedia.org/wiki/Epithelial>.
8. *Gastrointestinal tract*. Wikipedia, The Free Encyclopedia 8 Sep 2008, 02:55 UTC [cited 18 Sep 2008]; Available from: http://en.wikipedia.org/w/index.php?title=Gastrointestinal_tract&oldid=236992320.
9. Huczko, A., *Template-based synthesis of nanomaterials*. Applied Physics A-Materials Science & Processing, 2000. **70**(4): p. 365-376.
10. Chik, H. and J.M. Xu, *Nanometric superlattices: non-lithographic fabrication, materials, and prospects*. Materials Science & Engineering R-Reports, 2004. **43**(4): p. 103-138.
11. Ohanian, H.C., *Principles of Quantum Mechanics*, ed. N.C. Romanelli. 1990, Englewood Cliffs: Prentice Hall.
12. Tegenfeldt, J.O., et al., *Micro- and nanofluidics for DNA analysis*. Analytical and Bioanalytical Chemistry, 2004. **378**(7): p. 1678-1692.
13. Song, A.M. *Nanometre-Scale Technology and Devices*. [Home Page] [cited 17 Sept. 08]; Available from: http://personalpages.manchester.ac.uk/staff/A.Song/research/nano_research.htm.
14. Cao, G.Z. and D.W. Liu, *Template-based synthesis of nanorod, nanowire, and nanotube arrays*. Advances in Colloid and Interface Science, 2008. **136**: p. 45-64.
15. Sarkar, J., G.G. Khan, and A. Basumallick, *Nanowires: properties, applications and synthesis via porous aluminium oxide template*. Bulletin of Materials Science, 2007. **30**(3): p. 271-290.
16. Schneider, J.J. and J. Engstler, *Carbon and polymer filaments in nanoporous alumina*. European Journal of Inorganic Chemistry, 2006: p. 1723-1736.
17. Lei, Y., W.P. Cai, and G. Wilde, *Highly ordered nanostructures with tunable size, shape and properties: A new way to surface nano-patterning using ultra-thin alumina masks*. Progress in Materials Science, 2007. **52**: p. 465-539.

18. Saito, R., G. Dresselhaus, and M.S. Dresselhaus, *Physical Properties of Carbon Nanotubes*. 1998, London: Imperial College Press.
19. Shenderova, O.A., V.V. Zhirnov, and D.W. Brenner, *Carbon nanostructures*. *Critical Reviews in Solid State and Materials Sciences*, 2002. **27**(3-4): p. 227-356.
20. Straus, D.A., et al., *Photocurrent response of the carbon nanotube-silicon heterojunction array*. *IET Circuits Devices & Systems*, 2007. **1**: p. 200-204.
21. Yeh, J.I., et al., *Peptide nanowires for coordination and signal transduction of peroxidase biosensors to carbon nanotube electrode arrays*. *Biosensors & Bioelectronics*, 2007. **23**: p. 568-574.
22. Gao, Q.F., H.M. Pang, and E.S. Yeung, *Simultaneous genetic typing from multiple short tandem repeat loci using a 96-capillary array electrophoresis system*. *Electrophoresis*, 1999. **20**(7): p. 1518-1526.
23. Lo, R.C. and V.M. Ugaz, *Separation performance of single-stranded DNA electrophoresis in photopolymerized cross-linked polyacrylamide gels*. *Electrophoresis*, 2006. **27**(2): p. 373-386.
24. Kumaresan, P., et al., *High-throughput single copy DNA amplification and cell analysis in engineered nanoliter droplets*. *Analytical Chemistry*, 2008. **80**(10): p. 3522-3529.
25. Meng, Z. and T.D. Veenstra, *Proteomic analysis of serum, plasma, and lymph for the identification of biomarkers*. *Proteomics Clinical Applications*, 2007. **1**(8): p. 747-757.
26. Lai, K.K.Y., D. Kolippakkam, and L. Beretta, *Comprehensive and quantitative proteome profiling of the mouse liver and plasma*. *Hepatology*, 2008. **47**(3): p. 1043-1051.
27. Striemer, C.C., et al., *Charge- and size-based separation of macromolecules using ultrathin silicon membranes*. *Nature*, 2007. **445**(7129): p. 749-753.
28. Pennathur, S. and J.G. Santiago, *Electrokinetic transport in nanochannels. 2. Experiments*. *Analytical Chemistry*, 2005. **77**(21): p. 6782-6789.
29. Pennathur, S., et al., *Free-solution oligonucleotide separation in nanoscale channels*. *Analytical Chemistry*, 2007. **79**: p. 8316-8322.
30. Huang, L.R., et al., *A DNA prism for high-speed continuous fractionation of large DNA molecules*. *Nature Biotechnology*, 2002: p. 1-3.
31. Davis, J.A., et al., *Deterministic hydrodynamics: Taking blood apart*. *Proceedings of the National Academy of Sciences*, 2006. **103**(40): p. 14779-14784.
32. Blazej, R.G., P. Kumaresan, and R.A. Mathies, *Microfabricated bioprocessor for integrated nanoliter-scale Sanger DNA sequencing*. *Proceedings of the National Academy of Sciences of the United States of America*, 2006. **103**(19): p. 7240-7245.
33. Van den Berg, A. and M. Wessling, *Nanofluidics: Silicon for the perfect membrane*. *Nature*, 2007. **445**(7129): p. 726-726.
34. Lee, S.B. and C.R. Martin, *Electromodulated molecular transport in gold-nanotube membranes*. *Journal of the American Chemical Society*, 2002. **124**(40): p. 11850-11851.
35. Yamaguchi, A., et al., *Self-assembly of a silica-surfactant nanocomposite in a porous alumina membrane*. *Nature Materials*, 2004. **3**(5): p. 337-341.

36. Martin, F., et al., *Tailoring width of microfabricated nanochannels to solute size can be used to control diffusion kinetics*. Journal of Controlled Release, 2005. **102**(1): p. 123-133.
37. Liang, X.G., et al., *Single sub-20 nm wide, centimeter-long nanofluidic channel fabricated by novel nanoimprint Mold fabrication and direct imprinting*. Nano Letters, 2007. **7**: p. 3774-3780.
38. Seo, Y.S., et al., *DNA electrophoresis on nanopatterned surfaces*. Nano Letters, 2004. **4**(4): p. 659-664.
39. *Blood*. Wikipedia, The Free Encyclopedia 16 Sep 2008, 15:28 UTC [cited 17 Sep 2008]; Available from: <http://en.wikipedia.org/w/index.php?title=Blood&oldid=238821880>.
40. *Orders of magnitude (length)*. Wikipedia, The Free Encyclopedia 5 Sep 2008, 23:28 UTC [cited 17 Sep 2008]; Available from: [http://en.wikipedia.org/w/index.php?title=Orders_of_magnitude_\(length\)&oldid=236549166](http://en.wikipedia.org/w/index.php?title=Orders_of_magnitude_(length)&oldid=236549166).
41. Alberts, B., et al., *Molecular Biology of the Cell*. 4 ed. 2002, New York: Garland Science.
42. Calladine, C.R., et al., *Understanding DNA: The Molecule and How It Works*. 3 ed. 2004, London: Elsevier Academic Press.
43. *Electric Field*. Wikipedia, The Free Encyclopedia 26 Sep 2008, 17:22 UTC [cited 29 Sep 2008]; Available from: http://en.wikipedia.org/w/index.php?title=Electric_field&oldid=241165436.
44. *Drag (physics)*. Wikipedia, The Free Encyclopedia 21 Sep 2008, 22:12 UTC [cited 29 Sep 2008]; Available from: [http://en.wikipedia.org/w/index.php?title=Drag_\(physics\)&oldid=240095634](http://en.wikipedia.org/w/index.php?title=Drag_(physics)&oldid=240095634).
45. Oliver, G., et al., *Electrophoretic migration of proteins in semidilute polymer solutions*. Electrophoresis, 2008. **29**(5): p. 1152-1163.
46. Slater, G.W. and J. Noolandi, *The Biased Reptation Model of DNA Gel Electrophoresis: Mobility vs Molecular Size and Gel Concentration*. Biopolymers, 1989. **28**(10): p. 1781-1791.
47. Sartori, A., V. Barbier, and J.L. Viovy, *Sieving mechanisms in polymeric matrices*. Electrophoresis, 2003. **24**(3): p. 421-440.
48. *Persistence length*. Wikipedia, The Free Encyclopedia 21 Aug 2008, 23:03 UTC [cited 29 Sep 2008]; Available from: http://en.wikipedia.org/w/index.php?title=Persistence_length&oldid=233428433.
49. Maier, B. and J.O. Radler, *Conformation and self-diffusion of single DNA molecules confined to two dimensions*. Physical Review Letters, 1999. **82**(9): p. 1911-1914.
50. Zimbone, M. *Static and Dynamic Light Scattering on DNA Solution*. [Home Page] [cited 2008 23 Sept. 08]; Available from: www.ct.infn.it/~zimbone/softmatter/Dynamic%20Scattering.pdf.
51. *New England Biolabs Lambda DNA HindIII Digest*. [cited 28 Sep 2008]; Available from: <http://www.neb.com/nebecomm/products/productN3012.asp>.
52. Han, J.Y., J.P. Fu, and R.B. Schoch, *Molecular sieving using nanofilters: Past, present and future*. Lab on a Chip, 2008. **8**: p. 23-33.

53. Garcia, C.D., et al., *Versatile 3-channel high-voltage power supply for microchip capillary electrophoresis*. Lab on a Chip, 2003. **3**(4): p. 324-328.
54. Gai, H.W., et al., *Injection by hydrostatic pressure in conjunction with electrokinetic force on a microfluidic chip*. Electrophoresis, 2004. **25**(12): p. 1888-1894.
55. Blas, M., et al., *Numerical simulations of the second-order electrokinetic bias observed with the gated injection mode in chips*. Electrophoresis, 2007. **28**: p. 2961-2970.
56. Jacobson, S.C., et al., *Precolumn Reactions With Electrophoretic Analysis Integrated On A Microchip*. Analytical Chemistry, 1994. **66**(23): p. 4127-4132.
57. Lacharme, F. and M.A.M. Gijs, *Single potential electrophoresis microchip with reduced bias using pressure pulse injection*. Electrophoresis, 2006. **27**(14): p. 2924-2932.
58. Shultz-Lockyear, L.L., et al., *Effects of injector geometry and sample matrix on injection and sample loading in integrated capillary electrophoresis devices*. Electrophoresis, 1999. **20**(3): p. 529-538.
59. Mukhopadhyay, R., *What does nanofluidics have to offer?* Analytical Chemistry, 2006. **78**(21): p. 7379-7382.
60. Butler, J.M. and e. al., *Forensic DNA typing by capillary electrophoresis using the ABI Prism 310 and 3100 genetic analyzers for STR analysis*. Electrophoresis, 2004. **25**.
61. Sinville, R. and S.A. Soper, *High resolution DNA separations using microchip electrophoresis*. J. Sep. Sci., 2007: p. 1714-1728.
62. Koumi, P. and e. al., *Evaluation and validation of the ABI 3700, ABI 3100, and the MegaBACE 1000 capillary array electrophoresis instruments for use with short tandem repeat microsatellite typing in a forensic environment*. . Electrophoresis, 2004. **25**: p. 214.
63. Goedecke, N., et al., *A high-performance multilane microdevice system designed for the DNA forensics laboratory*. Electrophoresis, 2004. **25**(10-11): p. 1678-1686.
64. Guillo, C., J.P. Ferrance, and J.P. Landers, *Use of a capillary electrophoresis instrument with laser-induced fluorescence detection for DNA quantitation - Comparison of YO-PRO-1 and PicoGreen assays*. Journal of Chromatography A, 2006. **1113**(1-2): p. 239-243.
65. Austin, R., *Nanofluidics - A fork in the nano-road*. Nature Nanotechnology, 2007. **2**(2): p. 79-80.
66. Emerich, D.F. and C.G. Thanos, *Targeted nanoparticle-based drug delivery and diagnosis*. Journal of Drug Targeting, 2007. **15**(3): p. 163-183.
67. Lacerda, L., et al., *Carbon nanotubes as nanomedicines: From toxicology to pharmacology*. Advanced Drug Delivery Reviews, 2006. **58**(14): p. 1460-1470.
68. Instrument, S. *P-97 Pipette Cookbook*. Sutter Instrument Company [cited 2 October 2008]; Available from: http://www.sutter.com/contact/faqs/pipette_cookbook.pdf.
69. *Carbon nanotube*. Wikipedia, The Free Encyclopedia 26 Sep 2008, 20:11 UTC [cited 2 Oct 2008]; Available from: http://en.wikipedia.org/w/index.php?title=Carbon_nanotube&oldid=241197057.

70. *Copper*. Wikipedia, The Free Encyclopedia 2 Oct 2008, 00:02 UTC [cited 2 Oct 2008]; Available from: <http://en.wikipedia.org/w/index.php?title=Copper&oldid=242374823>.
71. Cherukuri, P., et al., *Mammalian pharmacokinetics of carbon nanotubes using intrinsic near-infrared fluorescence*. Proceedings of the National Academy of Sciences of the United States of America, 2006. **103**: p. 18882-18886.
72. Singh, R., et al., *Tissue biodistribution and blood clearance rates of intravenously administered carbon nanotube radiotracers*. Proceedings of the National Academy of Sciences of the United States of America, 2006. **103**(9): p. 3357-3362.
73. Lam, C.W., et al., *A review of carbon nanotube toxicity and assessment of potential occupational and environmental health risks*. Critical Reviews in Toxicology, 2006. **36**(3): p. 189-217.
74. Becker, M.L., et al., *Length-dependent uptake of DNA-wrapped single-walled carbon nanotubes*. Advanced Materials, 2007. **19**(7): p. 939-+.
75. Wick, P., et al., *The degree and kind of agglomeration affect carbon nanotube cytotoxicity*. Toxicology Letters, 2007. **168**(2): p. 121-131.
76. Chithrani, B.D. and W.C.W. Chan, *Elucidating the mechanism of cellular uptake and removal of protein-coated gold nanoparticles of different sizes and shapes*. Nano Letters, 2007. **7**(6): p. 1542-1550.
77. Singh, R., et al., *Binding and condensation of plasmid DNA onto functionalized carbon nanotubes: Toward the construction of nanotube-based gene delivery vectors*. Journal of the American Chemical Society, 2005. **127**: p. 4388-4396.
78. Klumpp, C., et al., *Functionalized carbon nanotubes as emerging nanovectors for the delivery of therapeutics*. Biochimica Et Biophysica Acta-Biomembranes, 2006. **1758**(3): p. 404-412.
79. Obataya, I., et al., *Nanoscale operation of a living cell using an atomic force microscope with a nanoneedle*. Nano Letters, 2005. **5**(1): p. 27-30.
80. Kam, N.W.S., Z. Liu, and H.J. Dai, *Functionalization of carbon nanotubes via cleavable disulfide bonds for efficient intracellular delivery of siRNA and potent gene silencing*. Journal of the American Chemical Society, 2005. **127**(36): p. 12492-12493.
81. Zhang, Z.H., et al., *Delivery of telomerase reverse transcriptase small interfering RNA in complex with positively charged single-walled carbon nanotubes suppresses tumor growth*. Clinical Cancer Research, 2006. **12**(16): p. 4933-4939.
82. Kam, N.W.S. and H.J. Dai, *Carbon nanotubes as intracellular protein transporters: Generality and biological functionality*. Journal of the American Chemical Society, 2005. **127**(16): p. 6021-6026.
83. Kam, N.W.S., et al., *Carbon nanotubes as multifunctional biological transporters and near-infrared agents for selective cancer cell destruction*. Proceedings of the National Academy of Sciences of the United States of America, 2005. **102**: p. 11600-11605.
84. Kouklin, N.A., et al., *Carbon nanotube probes for single-cell experimentation and assays*. Applied Physics Letters, 2005. **87**(17): p. 173901.

85. *DAPI*. Wikipedia, The Free Encyclopedia 27 Aug 2008, 12:44 UTC [cited 29 Sep 2008]; Available from: <http://en.wikipedia.org/w/index.php?title=DAPI&oldid=234554591>.
86. *House Mouse*. Wikipedia, The Free Encyclopedia 18 Sep 2008, 06:30 UTC [cited 21 Sep 2008]; Available from: http://en.wikipedia.org/w/index.php?title=House_Mouse&oldid=239208565.
87. Zelikin, A.N., et al., *A general approach for DNA encapsulation in degradable polymer microparticles*. ACS Nano, 2007. **1**: p. 63-69.
88. *FISH Fact Sheet*. National Human Genome Research Institute 13 May 2008 [cited 29 Sept. 08]; Available from: <http://www.genome.gov/10000206>.
89. Taft, B.J., et al., *Site-specific assembly of DNA and appended cargo on arrayed carbon nanotubes*. Journal of the American Chemical Society, 2004. **126**(40): p. 12750-12751.
90. Fackelmayer, F.O., *Nuclear architecture and gene expression in the quest for novel therapeutics*. Current Pharmaceutical Design, 2004. **10**(23): p. 2851-2860.
91. Salman, M., S.C. Jhanwar, and H. Ostrer, *Will the new cytogenetics replace the old cytogenetics?* Clinical Genetics, 2004. **66**(4): p. 265-275.
92. Wang, Q., et al., *The centrosome in normal and transformed cells*. DNA and Cell Biology, 2004. **23**(8): p. 475-489.
93. Levsky, J.M. and R.H. Singer, *Fluorescence in situ hybridization: past, present and future*. Journal of Cell Science, 2003. **116**(14): p. 2833-2838.
94. Durm, M., et al., *Optimized Fast-FISH with alpha-satellite probes: Acceleration by microwave activation*. Brazilian Journal of Medical and Biological Research, 1997. **30**(1): p. 15-23.
95. Henegariu, O., et al., *Improvements in cytogenetic slide preparation: Controlled chromosome spreading, chemical aging and gradual denaturing*. Cytometry, 2001. **43**(2): p. 101-109.